ANALYSIS AND FEEDBACK CONTROL OF THE SCANNING LASER EPITAXY PROCESS APPLIED TO NICKEL-BASE SUPERALLOYS

A Dissertation
Presented to
The Academic Faculty

by

Rohan Bansal

In Partial Fulfillment
of the Requirements for the Degree
Doctor of Philosophy in the
George W. Woodruff School of Mechanical Engineering

Georgia Institute of Technology
May 2013

ANALYSIS AND FEEDBACK CONTROL OF THE SCANNING LASER EPITAXY PROCESS APPLIED TO NICKEL-BASE SUPERALLOYS

Approved by:

Dr. Suman Das, Advisor
George W. Woodruff School of
Mechanical Engineering
Georgia Institute of Technology

Dr. Yogendra K. Joshi
George W. Woodruff School of
Mechanical Engineering
Georgia Institute of Technology

Dr. Nader Sadegh
George W. Woodruff School of
Mechanical Engineering
Georgia Institute of Technology

Dr. Jianjun Shi
School of Industrial and Systems
Engineering
Georgia Institute of Technology

Dr. Sudarsanam Suresh Babu
Department of Materials Science and
Engineering
The Ohio State University

Date Approved: April 01, 2013

Dedicated to family, friends, good health, and good times...

ACKNOWLEDGEMENTS

The road towards completing a PhD is a long journey and it is made worthwhile through the compassion and support of many individuals, without whom I could not have traveled this far.

Firstly I would like to express my gratitude towards my advisor, Dr. Suman Das, for taking me under his wing and guiding me throughout this journey. I especially appreciate how incredibly approachable he has been throughout the years and for all of the advice that he has provided me on interesting research topics and areas to pursue. He has been supportive of me through all of the ups and downs of research and always kept his cool, even when I may have made mistakes or gone down the wrong path.

I would also like to thank each of the members of my dissertation reading committee, Dr. Yogendra K. Joshi, Dr. Nader Sadegh, Dr. Jianjun Shi, and Dr. Sudarsanam Suresh Babu, for taking a significant amount of their valuable time to review my proposal and final dissertation. Their suggestions for how to make my work better and more scientifically valuable have been greatly appreciated.

I would like to thank Paul Cilino for all of the incredible design work and machining that he has done to support the research in our group and especially on my particular project. Kyle and Ahn in the ME electronics shop have also helped me develop and produce several circuits along the way. Kysten Raleigh has also been helpful in fulfilling our purchase requests and helping out with other administrative activities that make our research go smoothly.

Dr. Kadaba has provided me with incredible guidance throughout my whole undergraduate and graduate career. It is because of his guidance that I was able to

make it through the qualifying exams.

I would like to thank all of our sponsors and supporters. In particular, I would like to acknowledge Dr. Khershed Cooper and Dr. Ralph Wachter in the ONR, and Don Deptowicz at PCC for their support.

Many other individuals have given me moral support over the years, including all of my close friends, my extended family, and the other members of the Direct Digital Manufacturing group, past and present.

There are also several teams of people that make it a pleasure to get work done today, including the teams at Google, Evernote, Dropbox, and GitHub. I can't imagine doing research without these valuable tools.

Most importantly, I would like to thank my parents for teaching me the value of education, for supporting every choice I have ever made, for pushing me to venture beyond what I initially thought I could accomplish and for simply just putting up with me for all of these years. I cannot imagine having a more inspirational set of parents from whom to derive life values. I would like to thank my grandparents for teaching me mathematics at a young age and for all of their support throughout the years. I would also like to thank my brother for his never-ending friendship and for keeping in touch even when I seemed to drift away.

Finally, I would like to thank my lovely fiancé Emelia for all of her compassion and support throughout these past five years. It is her love that has made life so enjoyable and kept my spirits up throughout this whole process.

TABLE OF CONTENTS

LIST OF TABLES

LIST OF FIGURES

xiii

xiv

LIST OF SYMBOLS OR ABBREVIATIONS

α Absorptivity of an object.

α_s Scanner angle of operation.

ARX   Auto-Regresive model with eXternal input.

c Speed of light, $299792458\frac{m}{s}$.

CET   Columnar to Equiaxed Transition.

CFD   Computational Fluid Dynamics.

CTR   Columnar to total height ratio.

CW   Continuous Wave.

DAQ   Data Acquisition card.

DARMA   Discrete Auto-Regressive Moving Average.

DDC   Ductility dip cracking.

DFM   Dynamic Focusing Model.

DLF   Direct Laser Fabrication.

DMLS   Direct Metal Laser Sintering.

DoE   Design of Experiment.

DPC   Distributed Parameter Control.

DS   Directionally-solidified.

E-LMF   Epitaxial Laser Metal Forming.

E_{acc} Accumulated energy units.

EB   Electron Beam welding.

EBSD   Electron Back Scattering Diffraction.

E_d Energy density.

E_{dv} Volumetric energy density.

ϵ Emissivity of an object.

ϵ_p Measured pyrometer emissivity.

ϵ_t Adjusted thermal camera emissivity.

EQ   Equiaxed or polycrystaline.

η Carnot efficiency.

FCC   Face centered cubic.

FIR   Finite Impulse Response.

FS Field size.

G Temperature Gradient.

γ' Gamma prime precipitate.

GTA   Gas Tungsten Arc welding.

h Planck's constant, $6.626068 \cdot 10^{-34} \frac{m^2 kg}{s}$.

H Hatch spacing or Scan spacing.

HAZ   Heat affected zone.

HFOV   Horizontal Field of View.

HIP   Hot Isostatic Pressing.

HMC   Heterogeneous Multi-functional Component.

IFOV   Instantaneous field of view.

K Equiaxed criterion material constant.

k_B Boltzmann constant, $1.3806503 \cdot 10^{-23} \frac{m^2 kg}{s^2 K}$.

λ Wavelength of emitted radiation.

LENS   Laser Engineered Net Shaping.

LMF   Laser Metal Forming.

MFOV   Medium Field of View.

MRAC   Model Reference Adaptive Control.

n Equiaxed criterion material exponent constant.

OMT   Oriented to Misoriented Transition.

OSAAC   One Step Ahead Adaptive Control.

P Laser power.

PPM   Parts per Million.

ρ Reflectivity of an object.

S Scan speed.

SAC   Strain-age cracking.

σ Stefan's constant, $5.670373 \cdot 10^8 \frac{W}{m^2 K^4}$.

SISO   Single-Input Single-Output.

SLE   Scanning Laser Epitaxy.

SLM   Selective Laser Melting.

SLS   Selective Laser Sintering.

SP   Step Period.

SS   Step Size.

SX   Single-crystal or monocrystaline.

T Absolute temperature.

τ Transmissivity of an object.

T_{bot} Minimum thermal camera temperature.

T_{cor} Corrected pyrometer temperature.

T_e Turbine exhaust temperature.

T_i Turbine inlet temperature.

TIG   Tungsten Inert Gas welding.

T_p Powder thickness.

T_{therm} Corrected thermal camera temperature.

T_{top} Maximum thermal camera temperature.

T_{unc} Uncorrected pyrometer temperature.

V Solidification Velocity.

VFOV   Vertical Field of View.

W_{bb} Total radiant energy emitted by a black body.

W_d Scanner working distance.

W_λ Radiant energy emitted from the surface of the black body.

W_o Total radiant energy emitted by an object.

SUMMARY

Scanning Laser Epitaxy (SLE) is a new layer-by-layer additive manufacturing process being developed in the Direct Digital Manufacturing Laboratory at Georgia Tech. SLE allows for the fabrication of three-dimensional objects with specified microstructure through the controlled melting and re-solidification of a metal powder placed atop a base substrate. This dissertation discusses the work done to date on assessing the feasibility of using SLE to both repair single crystal (SX) turbine airfoils and manufacture functionally graded turbine components. Current processes such as selective laser melting (SLM) are not able to create structures with defined microstructure and often have issues with warping of underlying layers due to the high temperature gradients present when scanning a high power laser beam. Additionally, other methods of repair and buildup have typically been plagued by crack formation, equiaxed grains, stray grains, and grain multiplication that can occur when dendrite arms are separated from their main dendrites due to remelting. In this work, it is shown that the SLE process is capable of creating fully dense, crack-free equiaxed, directionally-solidified, and SX structures. The SLE process, though, is found to be currently constrained by the cumbersome method of choosing proper parameters and a relative lack of repeatability. Therefore, it is hypothesized that a real-time feedback control scheme based upon a robust offline model will be necessary both to create specified defect-free microstructures and to improve the repeatability of the process enough to allow for multi-layer growth. The proposed control schemes are based upon temperature data feedback provided at high frame rate by a thermal imaging camera. This data is used in both PID and model reference adaptive control (MRAC) schemes and drives the melt pool temperature during processing towards a reference melt pool

temperature that has been found to give a desired microstructure in the robust offline model of the process. The real-time control schemes will enable the ground breaking capabilities of the SLE process to create engine-ready net shape turbine components from raw powder material.

CHAPTER I

INTRODUCTION

1.1 *Background of the SLE Process*

Scanning Laser Epitaxy (SLE) is a new additive manufacturing technology being developed in the Direct Digital Manufacturing Laboratory at Georgia Tech that that will allow for: a.) the additive repair of damaged turbine engine hot-section components and b.) the fabrication of completely new three-dimensional superalloy components with specified microstructure through the controlled melting and re-solidification of metal powder layers placed atop a base substrate. The SLE process allows for the manufacture and repair of metallic parts with specified microstructure such as single-crystal (SX) components, as well as the manufacture and repair of heterogeneous multi-functional components (HMCs) with functionally graded microstructures. The components currently targeted for both manufacture and repair via the SLE process are components typically found in the hot sections of turbine engines. These parts are subjected to an environment of extreme temperature and pressure near the combustion stage of the engine during operation and, for this reason, are required to be constructed out of exotic materials with complex microstructure such as high temperature single-crystal (SX) nickel-base superalloys. There are several turbine engine hot-section components that are currently targeted for repair or manufacture using the SLE process, Figures 1(a) and 1(b) show examples of these components.

An overview of the SLE process is shown in Figures 2(a), 2(b) and 2(c). The SLE process consists of placing powder on a substrate and scanning it with a tightly focused high-power laser beam. The melting and re-solidification of the powder and underlying substrate are controlled by carefully adjusting the laser power and scan

(a) Turbine engine airfoil illustrating wear at the blade tip.
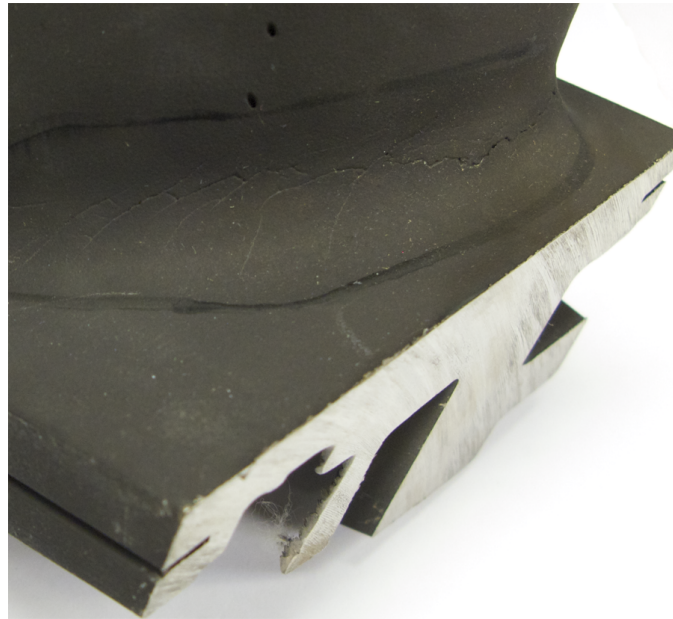
(b) Turbine engine component illustrating platform cracking.

Figure 1: Images of turbine engine hot section components.

speed such that a particular desired microstructure can be achieved while creating a perfect metallurgical bond between the substrate and the melted/re-solidified powder. The key difference between SLE and selective laser melting (SLM) is that a portion of the underlying substrate or underlying layer is remelted in SLE for the express purpose of seeding the grain growth of the subsequent layer whereas in SLM, several prior layers might be melted in the beam's scan path. This allows for the deposition of new material on existing parts without creation of new grain boundaries, creation of previously unattainable single-crystal and directionally-solidified microstructures

(a) Side view of the SLE repair process

(b) Side view of the multi-layer SLE process

(c) SLE Process on a turbine blade
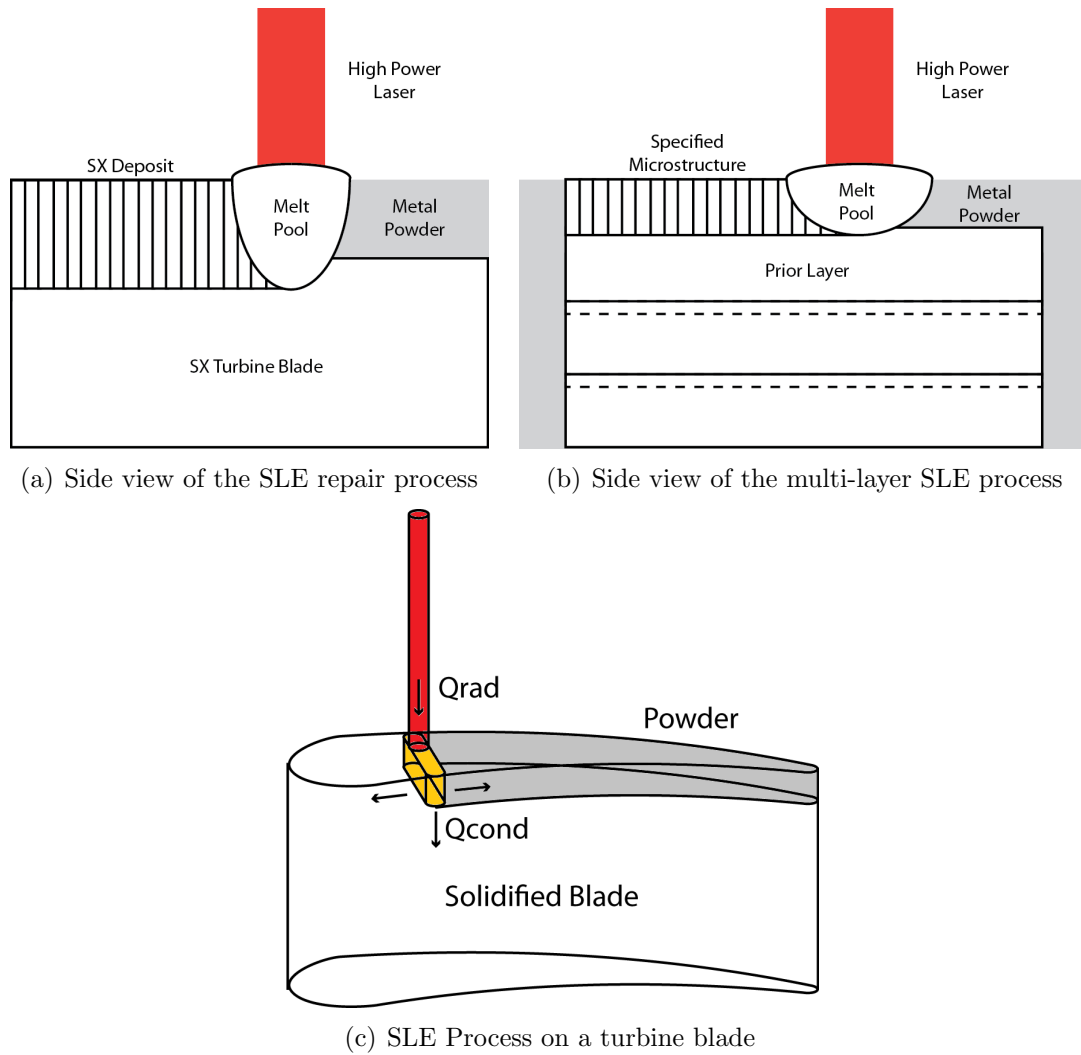
Figure 2: Overview of the SLE process

in additive manufacturing, and the potential for creating fully consolidated, porosity free, crack free and defect free three-dimensional parts with region specific microstructures. To achieve these desired capabilities, SLE requires that process parameters such as the scan speed and laser power are tightly controlled in real-time. Real-time control of these parameters allows for the ability to drive grain growth in particular directions by controlling the temperature gradients and cooling rates present during processing while also keeping the amount of meltback of the prior layer to a minimum. The main focus of the work presented in this dissertation is to assess the capabilities of the new SLE process as well as to extend its reach by implementing the required

real-time control algorithms to allow for creation of macrostructures with pre-defined microstructural morphology.

An overview of the various branches of fundamental research involved in the investigation and implementation of microstructure control in SLE is shown in Figure 3.
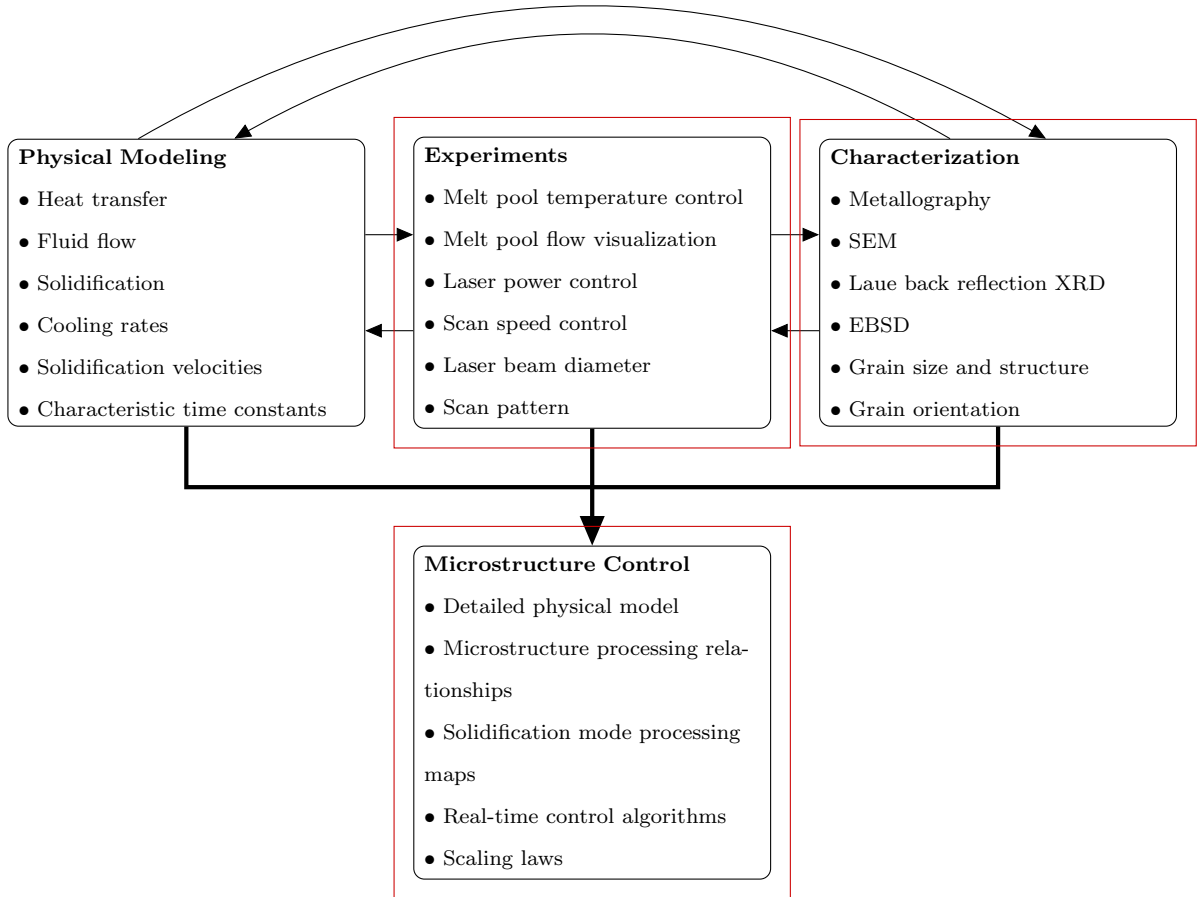
Figure 3: Research branches involved in the development of the SLE process with the main focuses of this dissertation indicated in red.

This dissertation covers much of the experimental and characterization work involved in the development of the SLE process for turbine component repair and

creation of HMCs. In particular, this dissertation covers the initial implementation of hardware and software required for the SLE process, the development of processing parameters and operating windows used to create proper structures using SLE, the addition of a real-time control scheme to refine the process parameters, and the utilization of optical metallography and image analysis to characterize processed samples.

1.2   Statement of the Problem

The initial research done on SLE as part of this dissertation focuses on turbine component repair. There are a number of challenges in repairing modern turbine components, mainly due to their manufacture out of conventionally non-weldable nickel-base superalloy materials that are cast in complex directionally solidified and single crystal microstructures. The first major challenge, as will be described in detail in Chapter 2 of this dissertation, is that many of the nickel-base superalloys under consideration have been previously deemed "non-weldable" and "non-joinable" due to some of their alloying components leading to various types of cracking during typical welding operations. The SLE process addresses the challenge of joining these superalloys by carefully controlling the thermal conditions present during processing such that the mechanisms causing the different types of cracking are minimized. The second major challenge in repairing these turbine components is creating a deposit on top of the underlying component in such a way that the underlying microstructure is minimally disturbed and is grown through the new deposit. The SLE process addresses this challenge by again carefully controlling the thermal conditions such that the melt back depth is minimized and proper thermal gradients are presented during subsequent solidification that drive grain growth in the deposit towards the particular desired microstructure.

The first portion of this dissertation will assess whether it is feasible to use the

SLE process to join these "non-joinable" superalloys while creating deposits of specified microstructure. The second portion of the dissertation will look at implementing real-time feedback control to further refine the process. The primary research objective, turbine component repair, is meant to be a stepping stone for the ultimate goal of creating multi-layer heterogeneous multifunctional components. Both of these applications are similar in that control of meltback depth, deposit height, and microstructural morphology are required but the multi-layer capability will require a stricter set of tolerances for each of these process outputs. Typically, the turbine component repair process is done in a single pass operation with a deposited layer thickness of 1000-2000μm. Figure 2(a) demonstrates the thick single layer deposition used in the repair process. The large height of this layer along with the lenient requirement of melt back depths on the order of 100-200μm allows for more room for error in selecting process parameters. Additionally, in the repair operation, all airfoil components will undergo a post-process contour grinding operation to remove excess material at the tip before being put into an engine, thus also removing a strict requirement on deposit height. Real-time control will still be required in the repair process to remove a number of defects that are currently found in the absence of feedback control, such as stray grain formation and a problematic oriented-to-misoriented transition as described in Chapter 4, but the higher tolerances will allow for easier initial development of the control schemes to take place. Once the repair process is fully understood, the next logical step is enabling multi-layer capability, which will require that layer thicknesses are on the order of 20-100μm, significantly reducing the allowable amount of variation in both melt back depth and deposit height. Minimizing the melt depth and creating a uniform deposit height on this scale while also defining particular microstructures will require extremely precise control of the processing parameters and conditions in real-time. Figure 2(b) demonstrates the thin layers with low remelt used during multi-layer builds.

1.3 Significance

SLE provides the potential for expanding the reach of additive manufacturing processes to the creation of modern engine-ready turbine components. There are a number of factors currently limiting other additive processes for creating such components. The main factor limiting other processes to this application is their inability to consistently create fully-dense structures with particular desired equiaxed, directionally-solidified or single-crystal microstructures. Current processes such as selective laser melting (SLM) are not able to create structures with defined microstructure and often have issues with warping of underlying layers due to the high temperature gradients present when scanning a high power laser beam [1, 2]. Direct metal laser sintering (DMLS) has issues with regulating the meltback depth of each layer and is limited in the number of usable materials due to the high cost of developing processing parameters for new materials [3]. Additionally, processes such as SLM and DMLS operate using open-loop control schemes and under improper atmospheric conditions, limiting the quality of produced deposits. Other methods of repair and buildup have typically been plagued by crack formation, equiaxed grains, stray grains, as well as grain multiplication that can occur when dendrite arms are separated from their main dendrites due to remelting [4, 5, 6, 7, 8].

A number of promising results have demonstrated SLE's capability of developing these particularly difficult microstructures using only open loop control, as illustrated in Figure 4. The sample in Figure 4 shows that carefully choosing process parameters can result in fully dense SX growth off the base substrate with a fairly uniform melt depth and deposit height across the entire length of the sample (in this case across multiple centimeters). However, a few issues prevent the process from being applied to engine ready parts in its current state.
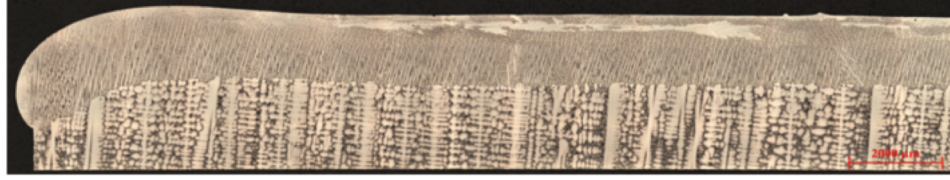
Figure 4: Cross-sectional optical image of a deposit made using the SLE process demonstrating growth of SX material off of an underlying SX substrate

The issues present in SLE mainly stem from a lack of repeatability in the current process as well as difficulty in choosing the proper parameter set to work with for a particular alloy. Typically, the laser power, scan speed, and scan spacing are chosen before processing by picking the parameters such that the energy density being applied to the substrate will be within a particular region that has previously been shown to generate a good deposit for that particular material and geometry. Determining the parameter sets that will lead to well-formed deposits is a time consuming task and requires that a design of experiment (DoE) analysis is done for each particular combination of material and geometry. Incorrectly choosing the parameter set leads to numerous defects including balling at the starting edge of the scan due to the incipient melt pool not wetting the starting edge of the substrate, lack of bonding along the substrate due to insufficient preheating, wide variations in melt depth and deposit height along the samples, and an excessive equiaxed region at the top of the deposit. A number of these defects are shown in the sample in Figure 5, which was run outside of the proper parameter range for creating a good deposit.
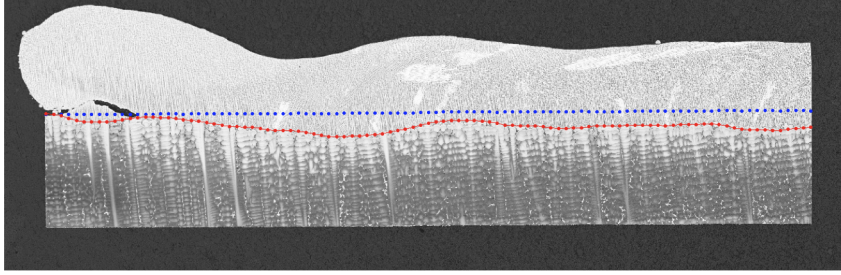
Figure 5: Cross-sectional optical image of a deposit made using the SLE process demonstrating the defects seen when improper process parameters are chosen. The blue line indicates the original substrate, and the red line indicates melt back depth.

Additionally, although the SLE process has demonstrated the capability of creating equiaxed, directionally solidified, and single-crystal microstructures, it is not currently capable of creating functionally graded components that have multiple types of microstructure in one part. It is hypothesized that applying a real-time closed loop feedback control scheme to the SLE process will increase the repeatability of the process and allow for the creation of functionally graded parts. The increase in repeatability will stem from two aspects of the real-time controller. Firstly, having a real-time control scheme will allow for the process to be abstracted away from choosing parameters such as laser power or scan speed before processing. Under a real-time control scheme the process will instead be focused on tracking a desired melt pool temperature profile that is determined by a robust offline model and has been shown to develop the desired microstructural features. This will allow for the creation of functionally-graded structures as well as remove the requirement of running a DoE to select parameters for every single different geometry/material combination that would be made. Secondly, the feedback control scheme will serve to regulate the temperature of the melt pool in spite of any issues or unforeseen problems that occur during processing, which will increase the robustness of the process, allowing for multi-layer builds and eliminating stray grains that might otherwise show up during processing.

The proposed control schemes will be based on temperature feedback data supplied during processing by a thermal imaging camera, as well as visual feedback from a high speed video microscope, and will control the laser power, scan speed, and scan path to track a desired melt pool temperature in real-time as discussed throughout this document.

1.4   Research Questions & Hypothesis

The primary goals of this research are to address the following questions:

1. Can the SLE process address the cracking issues typically found in joining some nickel-base superalloys?

2. Is it feasible to use SLE to create fully dense, defect-free deposits of specified microstructure?

3. How can the SLE process be used for the deposition of monolithic alloy compositions with the intended application of repairing wear damage and surface manufacturing defects on modern jet turbine components?

4. How can integrating real-time feedback control improve the SLE process and does controlling the melt pool temperature effectively control the produced deposit microstructure?

5. How can the SLE process be extended to allow for the creation of fully three-dimensional multilayer parts with functionally graded microstructures?

It is hypothesized that proper control of process parameters in the SLE process will allow for the joining of previously non-joinable nickel-base superalloys as well as the creation of deposits with specified microstructure. It is also hypothesized that real-time feedback control schemes based upon implementing a predefined processing temperature profile specified by an offline model will be necessary both to create

specified defect-free microstructures and to improve the repeatability of the process enough to allow for multi-layer growth.

1.5 Dissertation Outline

Chapter 2 of this dissertation will outline the challenges present in turbine component production and repair. In particular it will present details about nickel-base superalloys, phenomena related to cracking, prior additive processes used to repair turbine components, and prior schemes used for process control.

Chapter 3 will present details about all of the hardware and software implemented as part of this dissertation that enables the SLE process.

Chapter 4 will focus on details of SLE process development as well as an analysis of results showing the capabilities of the SLE process to create fully-dense and defect-free deposits of specified microstructure.

Chapter 5 will cover the implementation of a real-time control scheme to control the melt pool temperature defined by an offline model during processing and will address whether controlling the melt pool temperature has an effect on the produced microstructure.

Chapter 6 will summarize the research conducted as part of this dissertation, highlight the key original contributions, and outline some potential avenues for further research in the area.

CHAPTER II

BACKGROUND

2.1 Introduction

The primary goal of this research is to develop an additive manufacturing process capable of repairing and building modern turbine engine components made of nickel-base superalloys. The development of SLE to manufacture these types of components involves several different disciplines including metallurgy, manufacturing, control theory, and computer vision. This chapter first provides an overarching framework for why a process like SLE is useful in regards to modern turbine repair and then presents an overview of many of the challenges involved in the development of the SLE process. Highlights of how several different prior processes, both welding and additive, have tried to overcome these challenges are presented.

2.2 Turbine Engine Components

Gas turbines are commonly used for propulsion in aircraft and in land based energy generation systems. Modern day turbine engines typically operate under a Brayton cycle in which inlet air is first compressed, then mixed with fuel that is combusted and finally exhausted through an expansion turbine, generating power. A typical modern day turbine jet engine is illustrated in Figure 6.
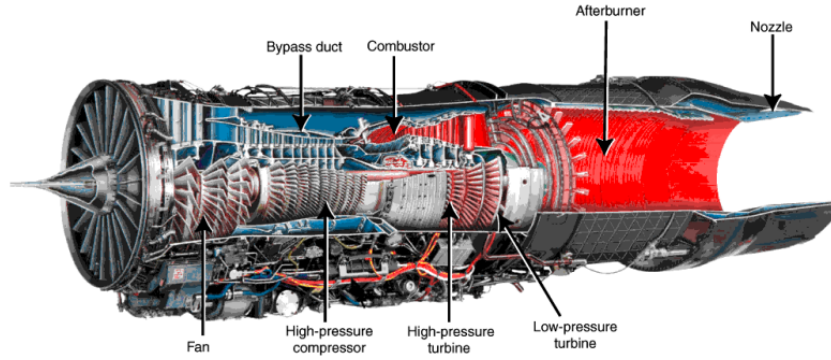
Figure 6: Cutaway of a commercial jet engine [9].

As indicated by the blue and red in Figure 6, there are two distinct sections of a typical turbine engine, a cold section before the combustor, and a hot section including the combustor and exhaust turbine. The ideal efficiency of a turbine engine, such as this one, operating under the Brayton cycle is governed by the Carnot efficiency, η, defined in Equation 1:

$$\eta = 1 - \frac{T_e}{T_i} \tag{1}$$

where T_e is the exhaust temperature and T_i is the inlet temperature. With this efficiency relationship in mind and noting that the inlet temperature is typically fixed, it can be seen that increasing engine efficiency is mainly derived from increasing the operating temperature of the exhaust turbine. For this reason, turbine engine manufactures strive to increase the operating temperature as well as pressure ratio of the exhaust turbines operating in their engines. Figure 7 shows the progression in turbine exhaust temperature over the past 70 years for one particular manufacturer's engines and is representative of the industry as a whole.
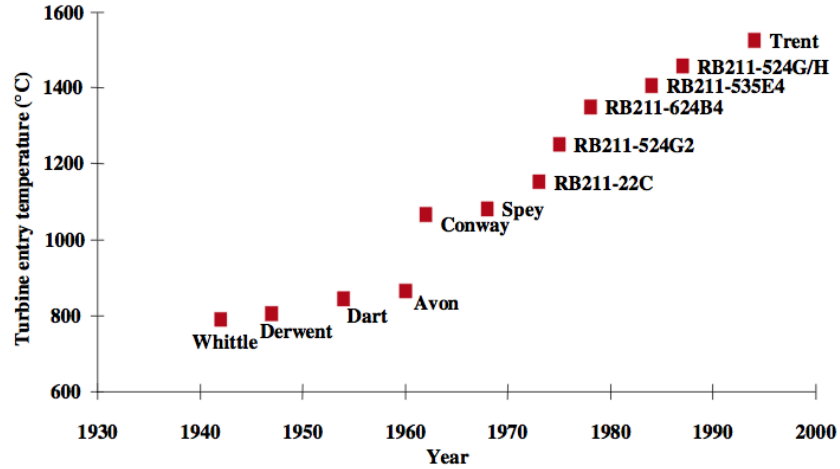
Figure 7: Development of exhaust turbine entry temperature over time of Rolls-Royce turbine engines [10].

As can be seen, the turbine exhaust operating temperature has been steadily increasing and is currently at an operating temperature in excess of $1500°C$. Accomodating operating temperatures this high has been accomplished through the use of high temperature metals such as nickel-base superalloys, introduction of complex internal cooling channels into the turbine blades, and development of thermal barrier coatings on the internal and external surfaces of the blades. Developments in these areas have progressed well enough that modern turbine engine exhaust turbines often operate at temperatures above the melting point of the superalloys that the blades are manufactured of while concurrently rotating at tens of thousands of rotations per minute without failure. Materials and their subsequent microstructures and geometries that are capable of operating under these extreme conditions are currently extremely difficult to manufacture and even more difficult to repair. The development of the SLE process hopes to make it possible to repair such hot-section turbine components manufactured from these difficult to repair materials and thus extend the life of these components.

2.3 Superalloys

2.3.1 Desireability

Increasing the operating temperature of a turbine engine can increase its efficiency but this is limited by the properties of the materials used inside of the engine. The high temperature components of turbine engines today can reach temperatures of over $1500°C$, limiting the usable materials to those that exhibit a resistance to creep and fatigue at those high temperatures [10, 11]. Nickel-based superalloys are one of these materials and are the most commonly used for the high temperature components of high performance jet aircraft. Figure 8 shows a comparison of several different classes of materials and their strength-to-weight ratio as a function of increasing temperature.
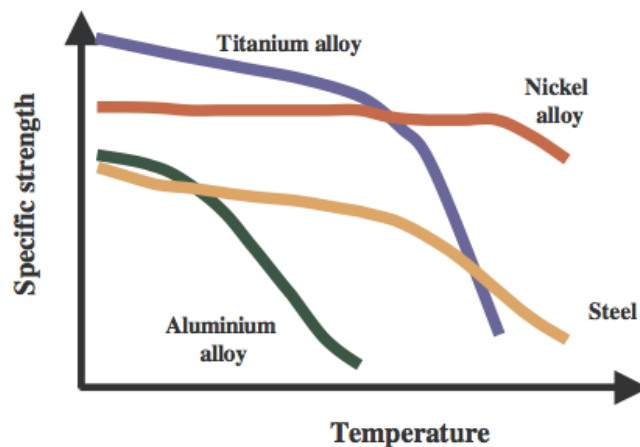
Figure 8: Specific strength vs temperature for several classes of turbine engine materials [10].

Titanium is used for the majority of the cold section components due to its lower density and ease of manufacturing, but as seen in Figure 8, nickel-base superalloys exhibit much higher strength at high temperature operating conditions than other classes of metals and, for this reason, they are used for the vast majority of hot-section turbine components.

15

2.3.2 Composition & Microstructure

Typical Ni-superalloys can contain upwards of ten different alloying elements that are meant to impart various strengthening properties to the alloy. Some common alloying components are Carbon and Boron used for grain boundary strengthening, Aluminum, Titanium, and Tantalum as precipitation hardening components, Chromium is added for corrosion resistance, and elements like Molybdenum and Tungsten are used to increase the melting temperature of the alloy. The compositions by weight % for three of the alloys considered in this dissertation are listed in Table 1 and melt temperature ranges are listed in Table 2.

Table 1: Chemical composition by % of Mar-M247, CMSX-4, and René-80 [12].

	Cr	Co	Mo	Re	W	Al	Ti	Ta	Hf	B	C	Zr	Ni
Mar-M247	8.0	10.0	0.6	—	10.0	5.5	1.0	3.0	1.5	0.015	0.15	0.03	Bal
CMSX-4	6.5	9.6	0.6	3.0	6.4	5.6	1.0	6.5	0.1	—	—	—	Bal
René-80	14.0	9.0	4.0	—	4.0	3.0	4.7	—	0.8	0.015	0.16	0.01	Bal

Table 2: Solidus and liquidus temperatures of Mar-M247, CMSX-4, and René-80 [13].

	T_{sol} (K)	T_{liq} (K)
Mar-M247	1158	1366
CMSX-4	1594	1654
René-80	1485	1611

Despite the complex alloying components and superior properties of these Ni-superalloys at high temperatures, they are still pushed to their performance limits. To further increase the strength and durability of the turbine components, these Ni-superalloys are now cast with particular microstructural morphologies that can better withstand the extreme operating conditions. There are three microstructural

morphologies typically found in cast turbine components, equiaxed (EQ) or poly-crystalline, directionally-solidified (DS), and single-crystal (SX) or monocrystaline, as shown in Figure 9 and Figure 10.
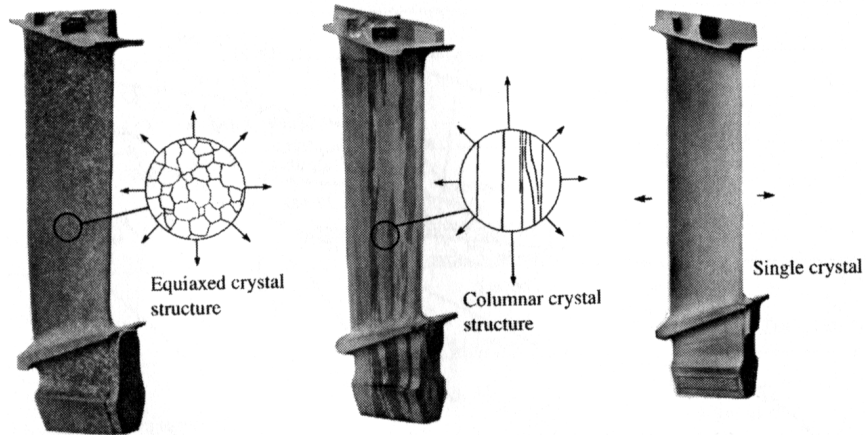
Figure 9: Turbine blades of equiaxed, DS, and SX microstructure [12].
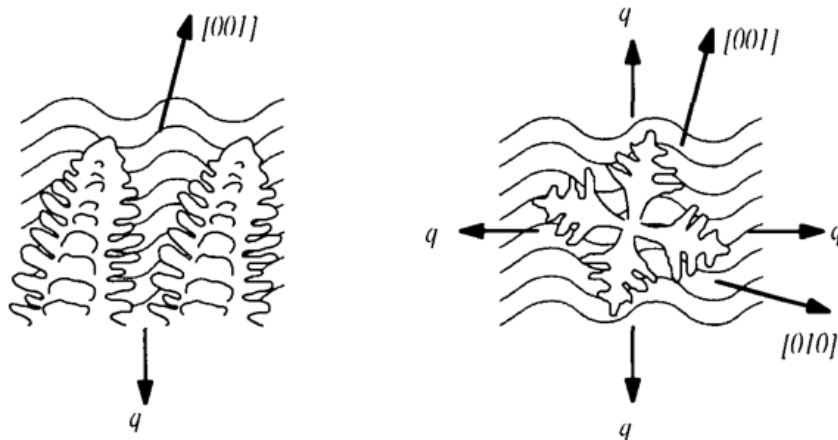
Figure 10: Representation of columnar (DS/SX) and equiaxed (EQ) dendritic formation [4].

Turbine components cast with a polycrystalline morphology are susceptible to failure because they contain some grain boundaries that are transverse to the longitudinal direction of the blades or to the main axis of stress when a blade is rotating around in

an engine. Directionally-solidified blades only have grain boundaries in a single direction perpendicular to the main axis of stress, resulting in a more durable blade with higher ductility and resistance to thermal fatigue. Single-crystal or monocrystaline components contain no grain boundaries and are the most desirable due to the ability to remove grain-boundary strengthening alloying components such as Boron and Carbon which would otherwise be necessary and would lower the melting point of the alloy, adversely impacting the fatigue life of the component. The three alloys investigated in this dissertation are part of a class of materials called precipitation-hardened alloys or gamma-prime (γ') formers. These alloys contain significant concentrations of Al and Ti that form precipitates of Ni_3Al or Ni_3Ti in the normally face centered cubic (FCC) structure of the solidified Nickel, as illustrated in Figure 11.
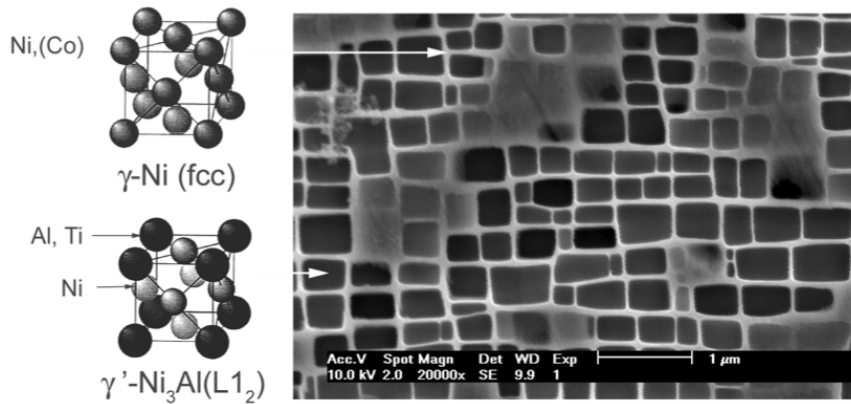
Figure 11: Illustration of the γ' phase in the FCC Nickel structure [6].

These γ' phase precipitates in the overall crystal lattice give rise to a yield strength anomaly in which the yield strengths of these materials actually increases at higher temperatures as illustrated in Figure 12.
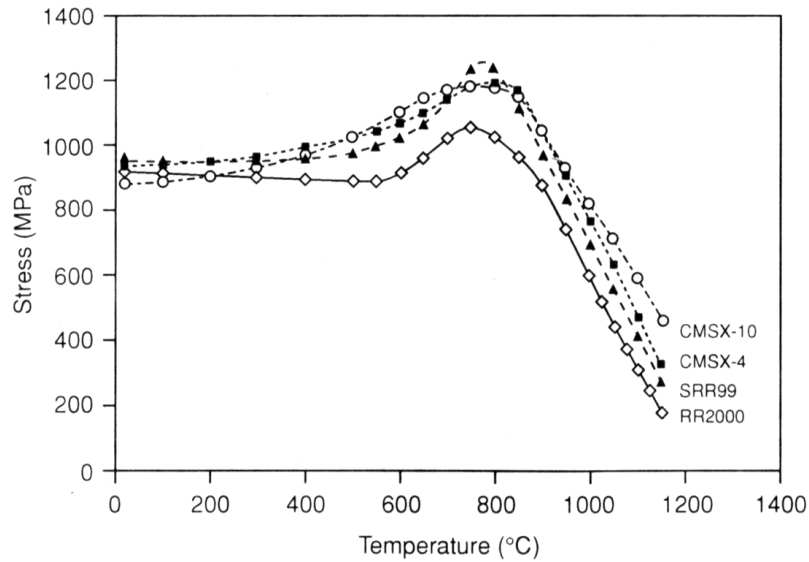
Figure 12: Variation of yield stress as a function of temperature for various precipitation hardened superalloys [12].

The main mechanism leading to this yield strength anomaly is the formation of an anti-phase boundary, locking dissociated dislocations at high temperatures. The details of this mechanism are described in the work of Decker and Mihalisin [14], Takeuchi and Kuramoto [15], and Yoo [16]. The superior properties provided by these γ' phase precipitates come at a cost though, as they lead to a high susceptability to strain-age cracking that adversely impacts the weldability and thus repairability of these alloys, as will be discussed in the next section alongside the other cracking mechanisms.

2.3.3 Processing Problems

The wide range of alloying elements used in these Ni-superalloys make them prone to cracking during solidification, adding to the challenge of both casting and repairing superalloy components. The mechanisms causing cracking include fusion zone solidification cracking (hot cracking), heat affected zone (HAZ) liquation cracking, strain-age

cracking, and ductility dip cracking. Addressing the issues leading to each of these types of cracking has plagued both prior and current state-of-the-art repair processes, and has typically limited repair operations to using filler metals with compositions that differ from the underlying substrate.

Fusion zone solidification cracking occurs at the terminal stages of solidification when shrinkage strains across partially solidified grain boundaries or interdendritic sites become too high, causing separation to occur, as noted in the work by Cieslak et al. [17, 18], DuPont et al. [19], and many others. The solidification temperature range, or range between solidus and liquidus temperatures of the alloy, and processing conditions are the primary factors that determine if solidification cracking will occur. The larger the range of solidification temperature is, the larger the crack-susceptible mushy region behind the initial melt pool will be. This is particularly problematic in many superalloys because the large number of alloying components leads to a relatively large solidification temperature range. Additionally, the segregation of many impurities commonly found in superalloys such as Phosphorus and Sulfur can create low melting point liquid films that wet grain boundary and interdendritic regions also leading to higher solidification cracking suceptability [20]. These cracking issues can be somewhat mitigated by using low impurity filler material and by controlling scan parameters such that the mushy zone size is limited during processing.

The HAZ is the area just outside of the fusion zone and is susceptible to two types of liquation cracking. The first, the segregation mechanism, occurs when low melting point impurity elements or Carbon/Boron diffuse towards grain boundaries and locally lower the melting point of these regions, resulting in areas of high strain and separation. The second mechanism, "constitutional" liquation, is particular to precipitation-hardened materials and occurs when a reaction between a constituent particle such as TiC reacts with the surrounding matrix causing localized melting. The effects of both of these mechanisms can be reduced by creation of smaller grains

which exposes a higher grain boundary area and reduces the unit strain per area of boundary. It has also been found that high heating rate results in more cracking in the HAZ and proper control of processing parameters can limit the effects of this cracking [20].

Strain-age cracking (SAC) typically occurs during post-process heat treatment of precipitation-strengthened alloys. SAC is caused by large amounts of weld residual stress, use of dissimilar filler material with a different coefficient of thermal expansion than the substrate, and particularly by dimensional changes near precipitates during heat treatment. It has been found that high Ti and Al concentrations in alloys leads to significant amounts of strain-age cracking and leads to many of these alloys being labled "non-weldable" or "non-joinable". Figure 13 illustrates the susceptibility of various alloys to strain age cracking, and illustrates the "non-weldability" of two of the alloys discussed in this dissertation, Mar-M247 and René-80.

Figure 13: Susceptability of various superalloys to strain-age cracking as a function of Al and Ti content [20].

Ductility dip cracking (DDC) is observed in superalloys with a high concentration of Chromium (above 25-30 wt%) in which a stark drop in ductility of the alloy occurs somwhere between the solidus and liquidus temperatures. Welding of materials prone to DDC has been difficult to overcome by means other than limiting restraint on the substrate during processing or by using filler metals containing less Chromium [20]. The three materials discussed in this dissertation, though, are not particularly prone to DDC due to their relatively lower concentrations of Chromium, and it is only mentioned for the sake of completeness.

2.4   State-of-the-Art Manufacture & Repair Processes

Typical turbine components are manufactured through a traditional investment casting process with directionally-solidified and single-crystal components being cast by carefully setting up and controlling the temperature gradients present during solidification. The temperature gradients during solidification serve to drive the grain growth direction and, if properly controlled, can be used to create DS and SX castings. DS and SX components are typically investment cast using either a Bridgman or Stockbarger technique. In these techniques, the mold is slowly vertically withdrawn from a casting furnace or induction heater at a controlled rate, on the order of several centimeters per hour, slowly propagating the solid-liquid interface and elongating the grains in the direction of withdrawal. Normally, this results in a DS structure, but if a seed crystal or seed selector is placed at the bottom of the casting mold, these techniques can produce an SX structure [12]. Due to the complexity and sensitivity of casting DS and SX parts there are relatively few foundries in the world capable of producing them, resulting in high costs and long lead times for these components.

Despite being cast with these advanced single-crystal microstructures, turbine blades still have a limited operating life due to material loss at the blade tip resulting from abrasion between the blade and the engine shroud. Once a blade has experienced

a certain amount of material loss, typically on the order of 0.5-1mm on a 8cm tall blade, it must be scrapped and replaced. Replacing each of these blades becomes quite expensive due to the difficulty involved in casting SX components. The high costs and long lead times associated with casting of turbine components directly leads to the necessity for developing a process capable of repairing aging components. Thus, various OEMs and spare parts manufacturers in the aerospace industry are interested in finding a process capable of repairing and reconditioning these blades such that they can be re-inserted in an engine. Currently, there is no effective way of repairing turbine blades that have been cast with a directionally solidified or single-crystal morphology due to the fact that many of these alloys are considered "non-weldable" and there is difficulty retaining the underlying microstructure of the substrate in the newly deposited material. Over the past several decades, many researchers have attempted to repair components using both welding and additive techniques with varying degrees of success.

2.4.1 Welding Processes

There are several welding processes that have been applied to the repair of nickel-base superalloys. The most commonly used processes are gas tungsten arc (GTA) welding or tungsten inert gas (TIG) welding, electron beam (EB) welding, and laser welding. Each of these processes is typically subject to the same limitations in producing specified microstructures such as DS or SX and crack formation. As discussed earlier in this chapter, these welding processes are susceptible to four types of cracking, solidification cracking, HAZ cracking, strain-age cracking, and ductility dip cracking. Figures 14 and 15 illustrate solidification and centerline cracking typically found in welding of superalloys as discussed in the work of Henderson et al. [21], Dye et al. [22], and Babu and Park et al. at Oak Ridge National Laboratory [7, 8].
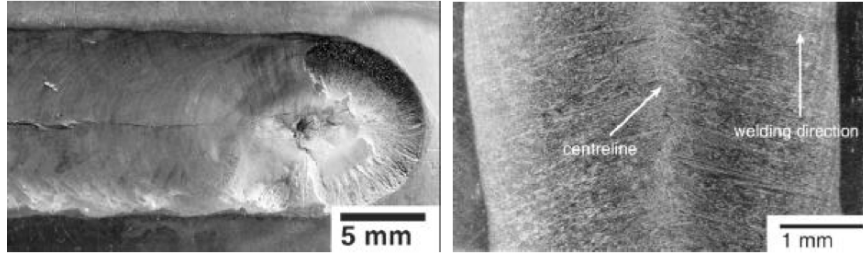
Figure 14: Illustration of fusion zone solidification cracking in a GTAW repair weld [21].
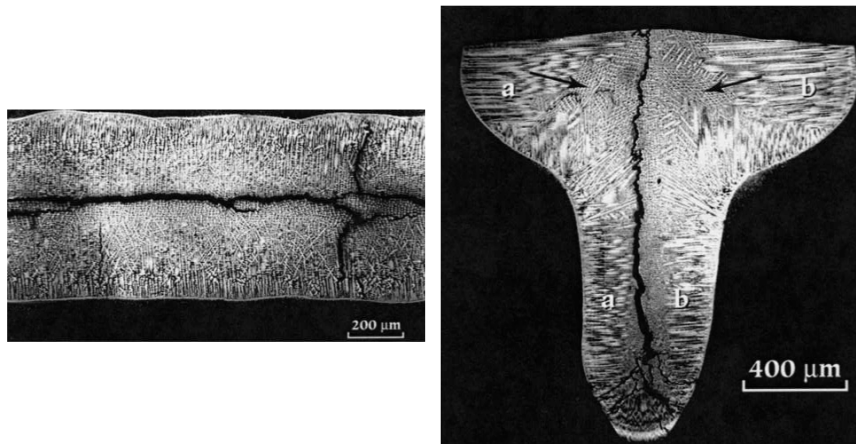
Figure 15: Illustration of fusion zone solidification cracking in a EB repair weld [7].

Anderson and DuPont have demonstrated that laser welding and EB welding of superalloys like CMSX-4 are less susceptible to cracking and stray grain formation than GTA welding as shown in Figures 16 and 17.
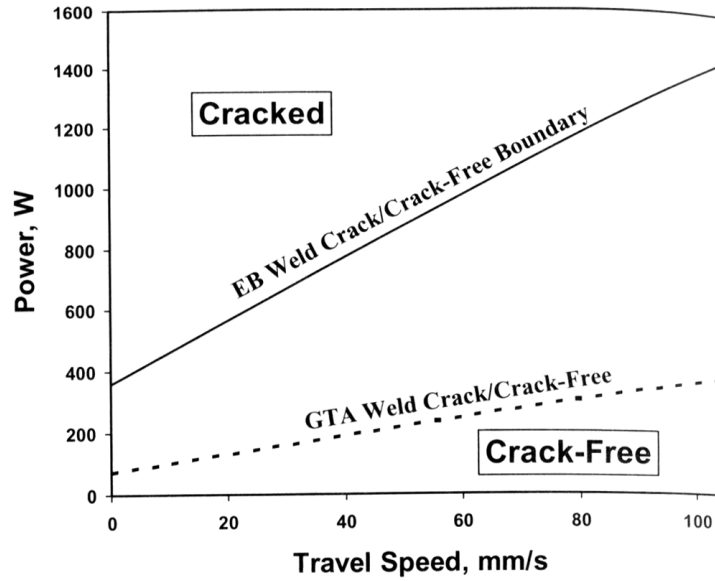
Figure 16: Crack susceptibility as a function of processing parameters under different welding schemes [20].
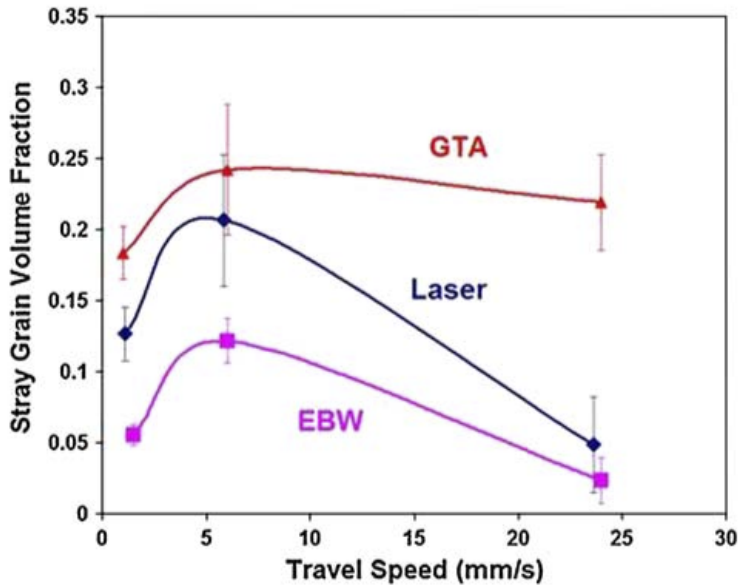
Figure 17: Stray grain formation as a function of processing parameters under different welding schemes [23].

The work of Ojo and Idowu [24, 25] shows the susceptibility of laser welding to HAZ cracking, as illustrated in Figure 18.
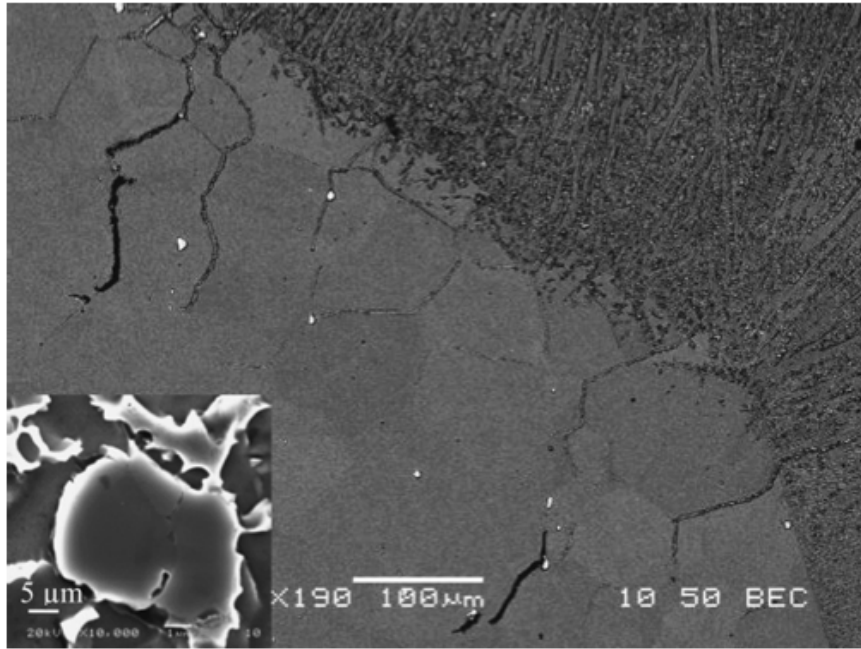
Figure 18: HAZ cracking in a laser weld operation of Allvac 718Plus [25].

DS and SX growth via welding processes started in the late 80s in the work of Rappaz et al. [26, 27] on a limited selection of Ni-base alloys. The work has since been expanded to many different alloys including CMSX-4 [23, 28, 29, 30] but the SX growth is limited to a height of between 100-200μm.

2.4.2 Laser Based Additive Processes

Laser-based cladding processes are the most commonly used methods for repairing single-crystal and superalloy components in general. First developed at the United Technology Research Center in 1979 [31], cladding processes typically involve the creation of a melt pool by a high-power energy source into which metal feed powder in blown. The energy source and powder feed are scanned across the substrate creating an additive deposit. Cladding processes used for additive manufacturing have been

labled under several different names in the literature, including Laser Engineered Net Shaping (LENS) [32, 33, 34, 5], Laser Metal Forming (LMF) [35], Direct Laser Fabrication (DLF) [36], and Epitaxial Laser Metal Forming (E-LMF) [4, 6]. An overview of a typical cladding process is illustrated in Figure 19 [37].
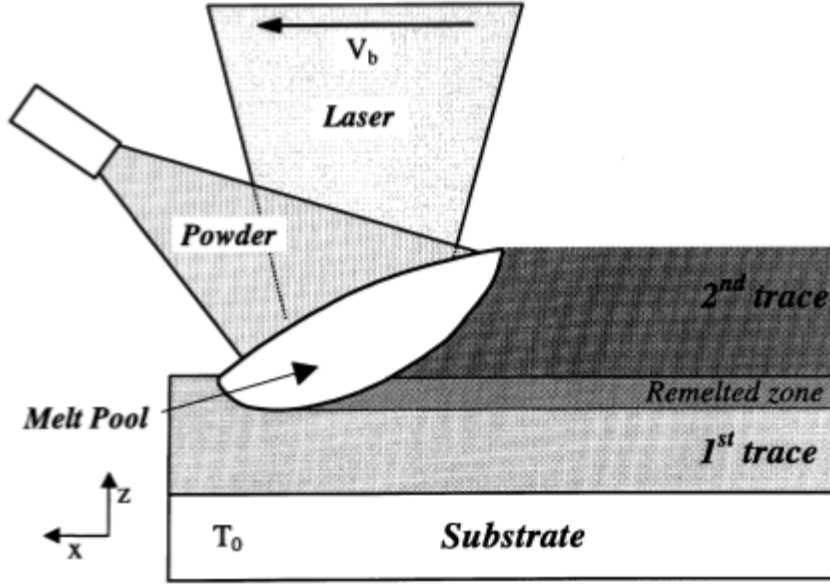
Figure 19: Overview of a typical cladding process showing the powder feed mechanism [37].

These cladding processes have been applied to the repair of cracks that form on the platform of a turbine blade. Although these methods have seen some success, this method of repair has typically been plagued by crack formation from the formation of equiaxed grains as well as grain multiplication that occurred when dendrite arms were separated from their main dendrites due to remelting [4, 5, 6]. The powder blowing mechanism used in cladding processes leads to two significant problems. The first problem is in the disturbance of convective currents in the melt pool caused by the high velocity powder particles entering the melt, adversely impacting DS and SX microsructure formation and causing stray grain formation. The second problem is

the limitation that having a mechanical powder feed assembly causes on the speed at which the energy source can scan accross the substrate. It has typically been found that higher scan speeds lead to less crack formation and fewer stray grain formation but the speed at which the energy source can move is significantly limited by the X-Y stage that the substrate is placed on in typical cladding operations.

United Technologies Corporation has attempted a method of creating crack free SX additive deposits on a substrate [38]. In this method, a relatively low power laser beam melts a filler metal that is deposited on a substrate over a large area. After melting, the laser power is lowered or turned off and the large melt pool slowly cools, creating an SX layer. If there are cracks in the resulting deposit, the layer is again remelted to remove the cracks. Although this containerless deposition method may work and create SX structures, it is limited in that the size of the melt pool is large and it cannot be used for the complex geometries found in turbine components like airfoils.

The work on SLE in this dissertation is a direct descendant of a powder bed based processes refered to as direct selective laser sintering (SLS) developed at The University of Texas at Austin in the late 90s [39]. An overview of the SLS process is shown in Figure 20.
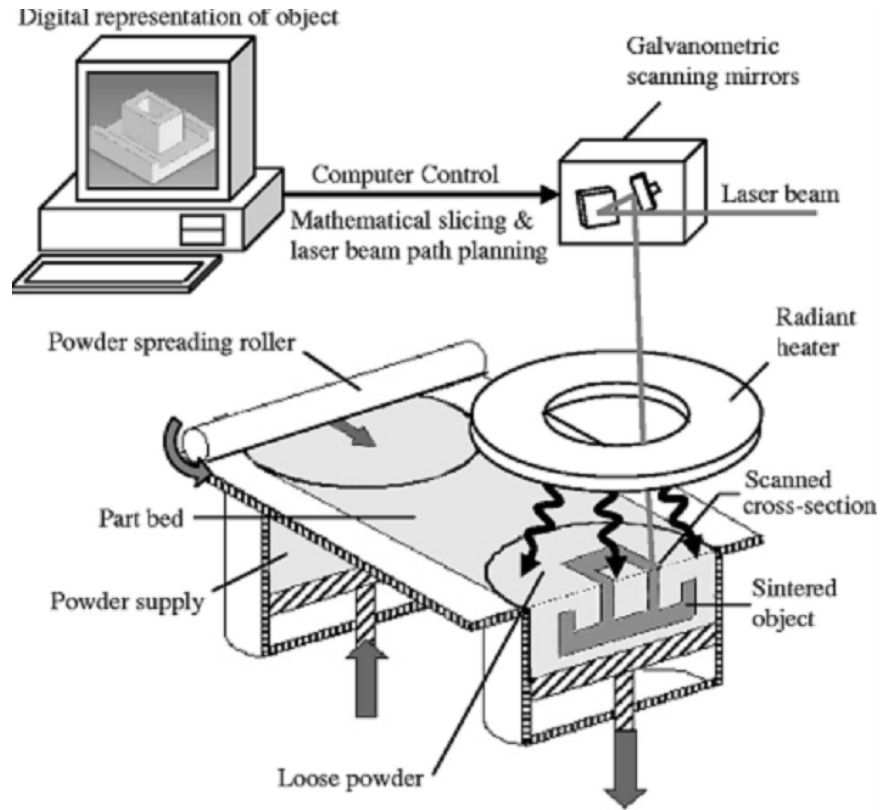
Figure 20: Overview of the SLS process [40].

Through layer-by-layer sintering of metal powder, the direct SLS process created components that were not fully dense, but could be made into fully dense engine ready components through the use of hot isostatic pressing (HIP). The work on SLE extends the work on Direct SLS by allowing for the direct construction of net-shape engine ready components that have specified EQ, DS or SX microstructure.

2.5 Process Control

Typical welding and cladding processes operate under open-loop control in which process maps are developed relating major control parameters like scan speed and input power to the resultant microstructural features. An example of such a processing map is illustrated in Figure 21 from the work of Henderson et al. [21].
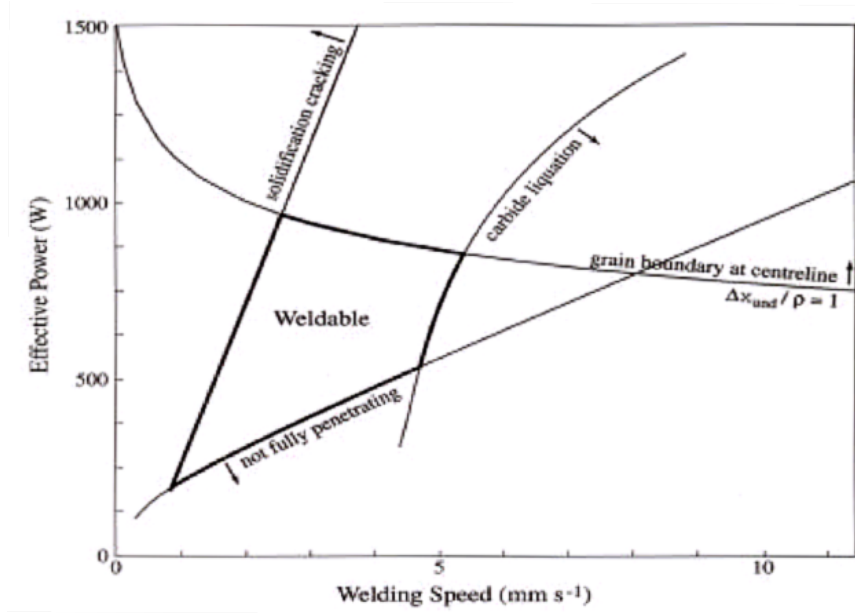
Figure 21: Process map showing parameters leading to good welds in GTA welding operation on IN718 [21].

Development of these processing maps is both time and material consuming, as experiments need to be run over a wide range of parameters to develop an accurate understanding of the process. As these processes become more complex, they include even more parameters and require even more experimentation to develop. In trying to overcome the amount of experimentation required to develop these processing maps, Gaumann, in his work on E-LMF, developed analytical relationships describing how various process parameters affected the resultant microstructure of a deposit [4]. In his work developing SX deposits using E-LMF, he found that the temperature gradient in the melt pool directly determined the resulting microstructure of the deposit. The relationship found to define the development of a columnar grain structure rather than an equiaxed grain structure is shown in Equation 2,

$$\frac{G^n}{V} > K \tag{2}$$

30

where G is the temperature gradient at a location in the melt pool, V is the solidification velocity, and n and K are experimentally determined properties of the material. Usage of this criterion resulted in processing maps such as the one illustrated in Figure 22.
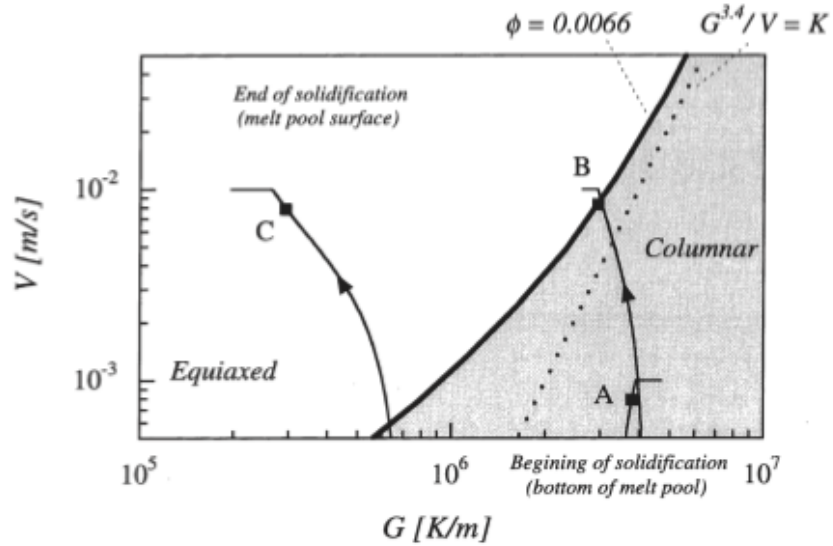
Figure 22: Process map showing what values of scan velocity and melt pool temperature gradient result in columnar DS/SX grain growth in CMSX-4 [37].

Figure 23 illustrates the columnar to equiaxed (CET) that occurs when the columnar criterion is not met, as most often happens near the top of the deposit.
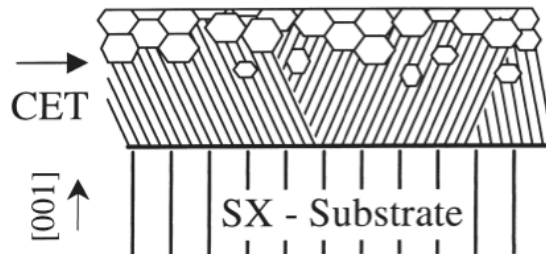
Figure 23: Illustration showing columnar microstructure transitioning to equiaxed microstructure (CET) when the temperature gradient in the melt pool is low [37].

The process parameters that produce a specified temperature gradient in the E-LMF process were then developed using a modified Rosenthal solution for the problem of moving heat source [41, 37]. The Rosenthal solution giving the temperature distribution for a semi-infinite body with constant properties and no latent heat release is shown in Equation 3:

$$T(x, y, z) = T_0 + \frac{\beta P}{2\pi\kappa r} exp\left(\frac{-V_b(r + x)}{2\alpha}\right) \tag{3}$$

Where $r = \sqrt{x^2 + y^2 + z^2}$, T_0 is the initial temperature of the material, α is its thermal diffusivity, κ is its thermal conductivity, P is the heat source input power, V_b is its velocity, and β is a term representing the heat source input power coupling into the material. For a stationary beam with a circular melt pool it is relatively easy to calculate the temperature gradient at the liquidus isotherm, r_l, as shown in Equation 4:

$$G = \left.\frac{dT}{dr}\right|_{r_l} = \frac{-2\pi\kappa}{\beta P}(T_l - T_0)^2 \tag{4}$$

Where $r_l = \frac{\beta P}{2\pi\kappa(T_l - T_0)}$ and T_l is the liquidus temperature. Although it is possible to use this criterion to develop processing maps relating other variables like preheat temperature and laser power to the temperature gradient and thus the formation of particular microstructures, it proves difficult to do when there are many variables and processing conditions that can change as a function of time and alter how the temperature gradient is developed, rendering a simple solution like the Rosenthal solution inaccurate. Most common superalloys exhibit material property variation as a function of temperature. Several examples of these variations are are provided in Figures 24 and 25.
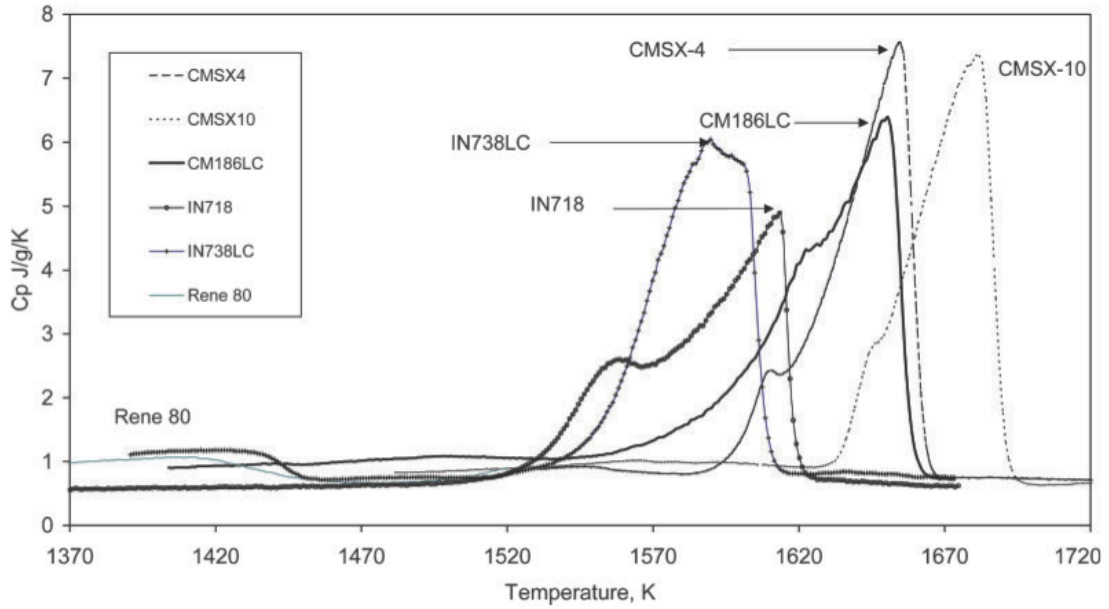
Figure 24: Plot of varying heat capacity, c_p, as a function of temperature for various superalloys [13].
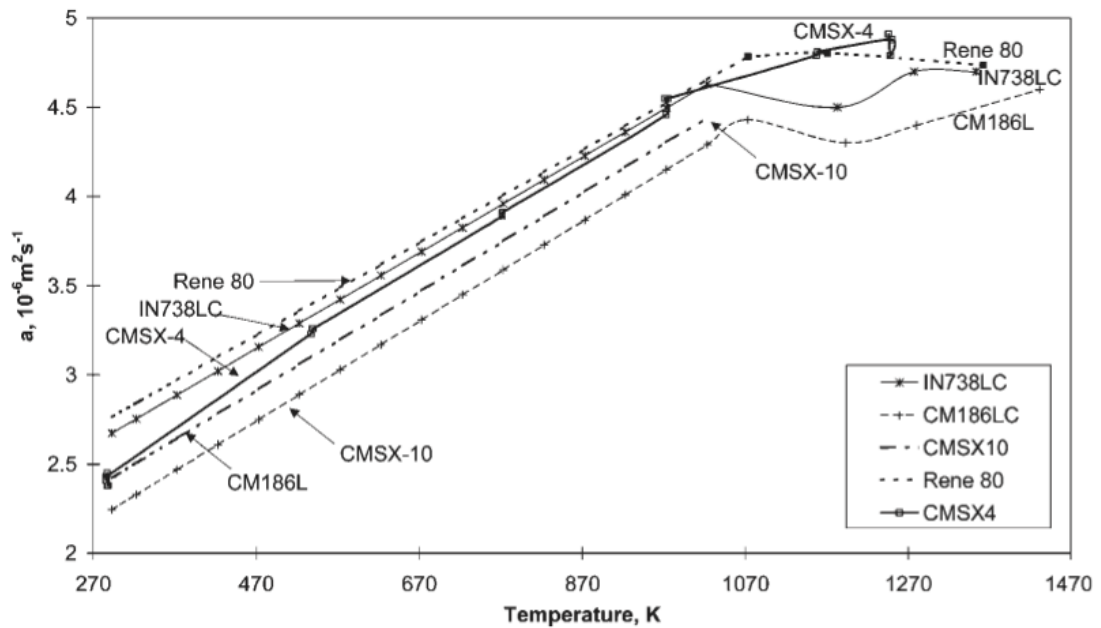
Figure 25: Plot of thermal diffusivity, α, as a function of temperature for various superalloys [13].

Enabling a repair/manufacturing process with the capability of robustly accounting for these variations in material properties and thus enabling the capability of producing HMCs is one of the main overall goals of the SLE process. To do so, the SLE process will utilize a robust offline computational fluid dynamics (CFD) model to develop desired melt pool temperature profiles and processing maps to utilize during processing to develop specified microstructure. The SLE process will then implement real-time feedback control to track the desired melt pool temperature as specified by the offline model and thus create the temperature gradients required for proper microstructure formation. The addition of real-time feedback control to the area of additive manufacturing has been targeted in the roadmap for additive manufacturing as an area of high interest. This is due to the relative lack of research done in the area in the past and the potential impact that proper control could have on the quality of parts that are capable being manufactured via additive processes [42].

In establishing a starting point for developing real-time control methodologies for controlling the melt pool temperature and laser scanning speed in the SLE process, a survey of the literature on control of welding processes was conducted. Welding processes typically utilize real-time feedback to control the heat-affected zone, weld bead diameter, melt depth, and weld microstructure. The first efforts to control the heat affected zone and cooling rate during welding operations were in the work of Boughton et al. in the late 1970s [43]. By the early to mid 1980s, in the work of Garlow and Weinert, it was found that adaptive controllers were necessary due to significant variations in the system parameters seen during welding operations [44]. Although there was some exploration of neural network modeling/controls to simplify the amount of effort required in determining weld system models as noted in the work of Andersen et al. and Zhang and Kovacevic [45, 46], various forms of adaptive controllers with online models of varying complexity remain the most prevalent today. Alongside these adaptive control schemes, Doumanidis and Hardt [47] explored the

concept of distributed parameter controllers that had prior been implemented in slab heating operations. They found that the weld bead geometry, microstructure, and final material properties could be more carefully controlled by taking into account the entire temperature field rather than just the weld temperature but the complexity of the control scheme seems to have subdued its prevalence.

Descriptions of work on real-time feedback control applied to additive processes like SLE is rather limited in the literature. One example of such work was presented by Salehi and Brandt [48] in which simple PID melt pool temperature control was applied to the cladding process but it was not found to create better deposits in any significant way. A second example is in the work of Tang and Landers [49, 50, 51] in which a general tracking controller using the internal model principle was used to control the melt pool temperature. In their work, the temperature control was quite accurate but it was not tied to any microstructural behavior, so the results are again inconclusive.

2.6 Summary

The challenges associated with the creation of nickel-superalloy based monolithic structures of specified microstructure are summarized as follows:

1. Superalloys are susceptible to several types of cracking, namely, fusion zone solidification cracking, HAZ cracking, strain-age cracking, and DDC cracking.

2. Creation of DS and SX microstructures while avoiding stray grain formation and cracking has proven difficult using prior processes.

3. Process parameter maps in which good crack-free DS and SX deposits are formed are difficult to develop and require significant time and material investments.

4. Real-time control has as of yet been unproven when applied in the area of additive manufacturing.

There are several reasons for which the SLE process will be able to address all of these challenges and will be capable of producing nickel-superalloy based monolithic structures of specified microstructure. The SLE process is capable of operating at a much higher scan velocity because the laser is scanned using a set of high speed galvanometer scanners and is not mechanically attached to and impeded by any powder blowing mechanism. Additionally, the use of a pre-placed powder bed in the SLE process eliminates any melt pool disturbance that would be caused by the powder blowing mechanism used in cladding processes, removing another potential cause of poor microstructure formation. The SLE process has also been found to avoid issues with hot tearing and liquation cracking found when using similar processes on a number of materials previously thought to be "non-weldable" and "non-joinable" [21]. The high resolution scan spacing used in the SLE process causes each subsequent raster scan to overlap a portion of both the prior and the next raster scans resulting in a pre-heat and post-heat treatment during the scanning operation, eliminating any hot tearing as seen in other processes. The high resolution scan spacing also results in finer grain structures developed in the deposits made via SLE, this exposes a large boundary area and limits the stresses that would otherwise cause liquation cracking [52]. These features of SLE have shown that it is possible to work with materials such as René-80 that are highly susceptible to liquation and strain-age cracking [53] and deemed unable to be welded by any prior process. Further control of the temperature gradients present in the process in real-time can only serve to further improve the SLE process and limit the surface tension-driven instabilities that cause many of these hot tearing and other cracking phenomenon.

Another key characteristic of the SLE process is its ability to create functionally-graded microstructures. A number of applications for turbine components with functionally graded microstructures have been identified. One example is that of a turbine disc made of a superalloy composition with equiaxed structures of radially increasing grain size. The smaller grains at the inside of the disc offer better tensile capabilities while grains towards the outside offer superior resistance to fatigue and creep [54, 55]. Typically components like these require numerous long processing steps and lengthy thermal treatment times to produce the functionally graded microstructures. SLE potentially offers the capability of producing components like these in a single processing step while also enabling complex internal features due to the layer-by-layer processing.

CHAPTER III

EXPERIMENTAL SETUP & METHODOLOGY

3.1   Introduction

This chapter provides an overview of the hardware and software implemented to en-able the SLE process as well as describes the experimental procedure followed in nearly all experiments. All of the hardware and software used in the development of the SLE process has been put together particularly to allow for full access to, and control of, all process parameters in real-time. Putting together each of these com-ponents individually and implementing the necessary software from the ground up, rather than using an already assembled SLS or SLM machine, enables full modifica-tion of scan path, scan speed, and laser power on-the-fly during real-time operation. The critical pieces of hardware involved in the SLE process are a high power 1kW Yt-terbium fiber laser, a 3-axis galvonometer scanning system, a controlled atmosphere processing chamber, a thermal imaging camera, and a melt pool video microscope system, as shown in Figures 26(a) and 26(b).
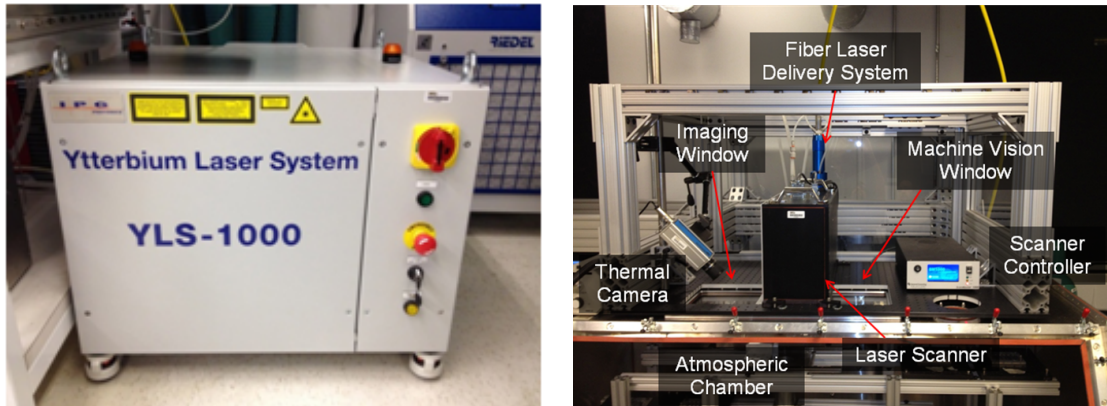
(a) Fiber Laser   (b) Equipment Overview

Figure 26: SLE Equipment Overview.

A schematic overview of the SLE process hardware is shown in Figure 27.
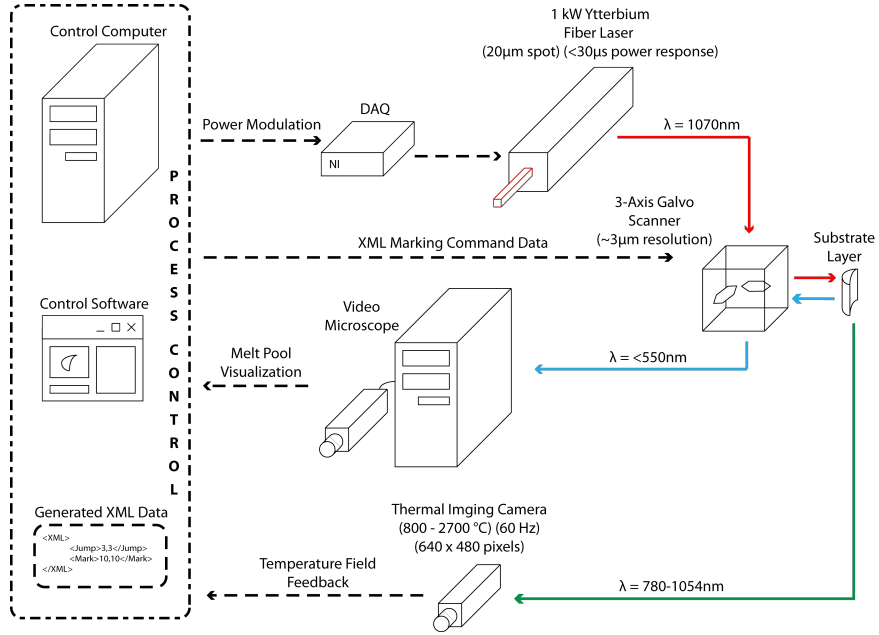
Figure 27: Overview of the SLE process

3.2   Hardware

3.2.1   High Power Laser

As with other additive manufacturing and welding processes, the backbone of the SLE process is the energy input source used to consolidate or otherwise affect the material being developed. In the case of the SLE process, the energy input source is a tightly focused high power laser. The laser currently being used for SLE processing is an IPG Photonics YLS-1000 continuous wave (CW) diode-pumped single mode Ytterbium fiber laser with a wavelength of approximately 1075nm. The YLS-1000 laser chosen can shutter the laser beam on and off within 100 μs and adjust its power in response to an external analog voltage signal at a rate of 5 kHz, allowing for high bandwidth control of the amount of energy being applied to the substrate. The typical optical characteristics of the YLS-1000 laser are listed in Table 3.

Table 3: YLS-1000 laser optical characteristics.

Characteristic	Test Condition	Symbol	Minimum	Typical	Maximum
Operation Mode				CW	
Polarization				Random	
Nominal Output Power		P_{NOM}	1000 W		
Power Tuning Range			10%		105%
Emission Wavelength	$P_{OUT} = 1kW$		1070 nm		1080 nm
Emission Linewidth	$P_{OUT} = 1kW$			3 nm	6 nm
Switching ON/OFF Time	$P_{OUT} = 1kW$			80 μs	100 μs
Power Modulation Rate	$P_{OUT} = 1kW$				5.0 kHz
Power Stability	Over 8hrs			1.00%	2.00%
Beam Quality		M^2		1.1	1.2
Beam Divergence				25 mrad	30 mrad
Aiming Laser Wavelength			640 nm		680 nm
Aiming Laser Power			0.5 mW		1 mW

The 0-10V analog voltage provided to the YLS-1000 to control the laser power is supplied by a National Instruments PCIe-6321 data acquisition (DAQ) card with a maximum modulation rate of 900 kS/s and a 16-bit resolution, which is well above the capabilities of the laser hardware. The DAQ card turns the control signal provided by the control computer during both open-loop and closed-loop control into the analog voltage required by the laser. The laser power was correlated with the analog input voltage by using the laser power meter built into the YLS-1000. Figure 28 shows the measured linear relationship between analog input voltage and output laser power.
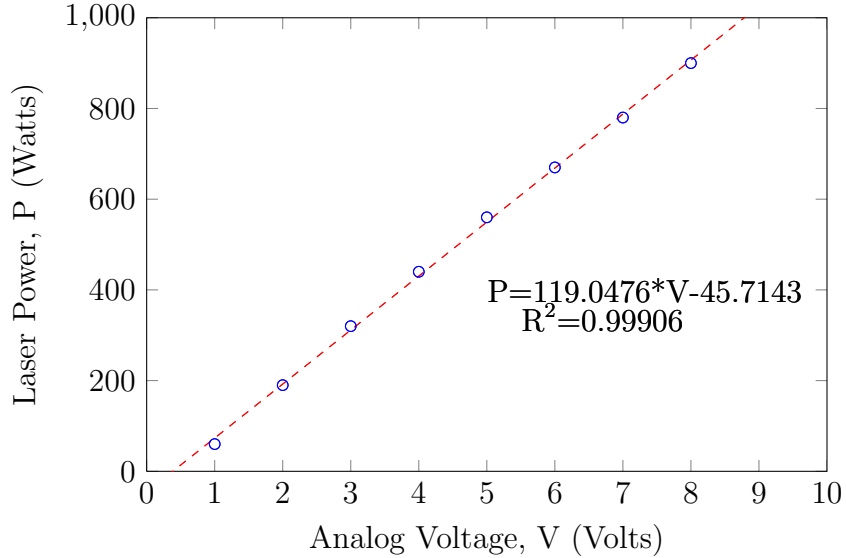
Figure 28: Linear fit of DAQ analog voltage to output laser power.

3.2.2 3-Axis Galvanometer Scanner

The fiber laser is focused through a 3-axis galvanometer scanner from Cambridge Technology to a spot size of 20 μm, enabling both tight control of the local temperature conditions surrounding the melt pool as well as post-process cleanup operations via laser cutting. The laser scanner has the capability of moving the incident beam across a 185mm by 185mm X-Y scan field at speeds of up to several m/s, though typical scan speeds used in SLE are on the order of hundreds of mm/sec. The incoming laser beam is collimated prior to entering the scan head by a 50mm diameter IPG-1070 collimator with a focal length of 160mm and an output beam $\frac{1}{e^2}$ value of 16mm. The optics internal to the Cambridge scanner then focus this beam down to a minimum spot size of 20 μm. The third axis of the scanner, the z-axis, is a prescanning objective dynamic focusing module (DFM), illustrated in Figure 29, that can adjust the beam focus during a scanning operation.
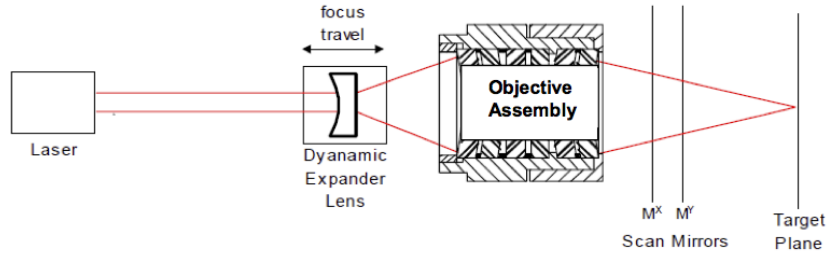
Figure 29: Unfolded optical path of the 3-axis scanning system.

The beam focus adjustment serves two purposes, the first is that it corrects for the focus lost due to the change in working distance as a scan moves across the scan field, as illustrated in Figure 30, and the second is that it can adjust the focus to allow for scanning on curved surfaces.
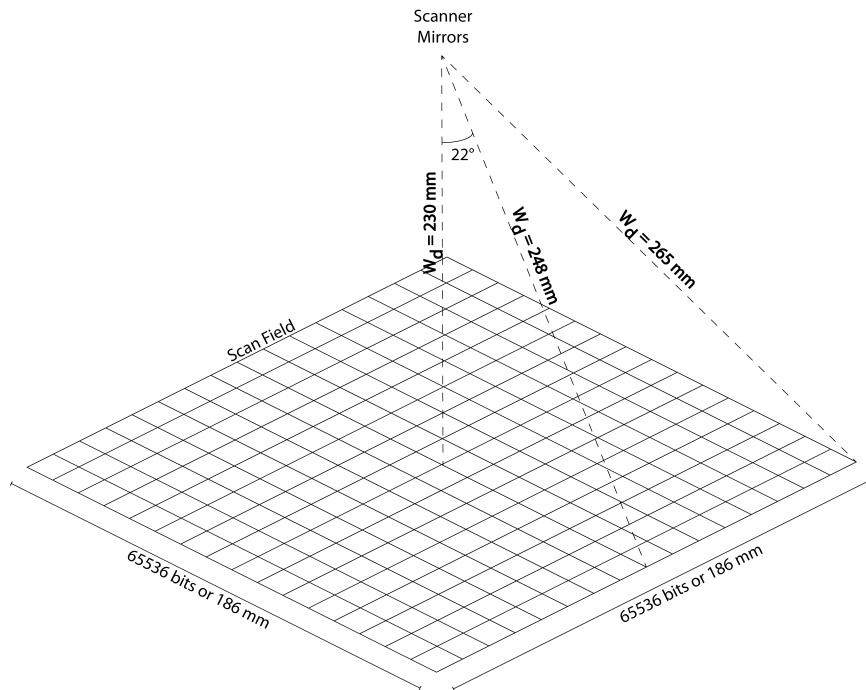
Figure 30: Illustration of the scan field and different working distances, W_d, at different locations.

3.2.3 Atmosphere Controlled Processing Chamber

The SLE process takes place inside of a heavily modified controlled-atmosphere glove box from Terra Universal, shown in Figure 31.
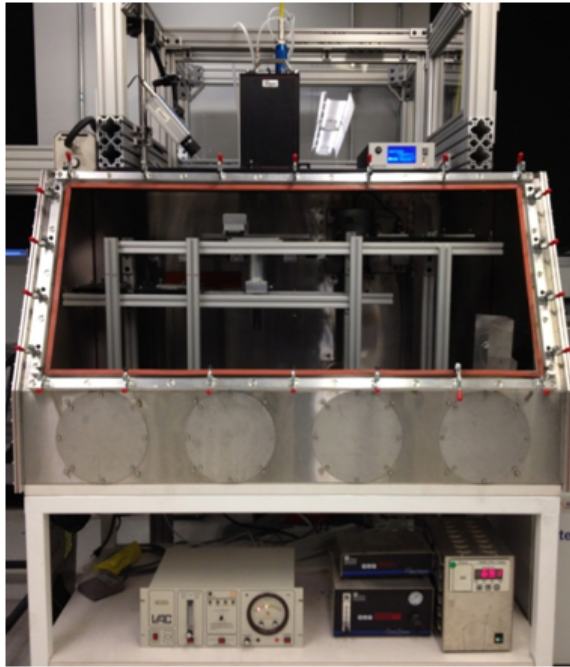
Figure 31: Controlled atmosphere processing chamber.

During processing, the chamber is backfilled with argon until the chamber atmosphere contains less than 10 parts-per-million (PPM) oxygen at atmospheric pressure, as measured by a Ntron Model 3100 oxygen analyzer that has been calibrated at atmospheric and 99.999% pure argon oxygen levels. The chamber contains a conveyor belt-like assembly that can hold up to five carrier plates that hold the samples during processing. After all of the samples on one carrier plate are processed, another carrier plate can be moved into place under the scan field allowing for higher throughput during experimentation. The processing chamber can also be equipped with the layering system illustrated in Figure 32 for processing of multi-layer deposits.
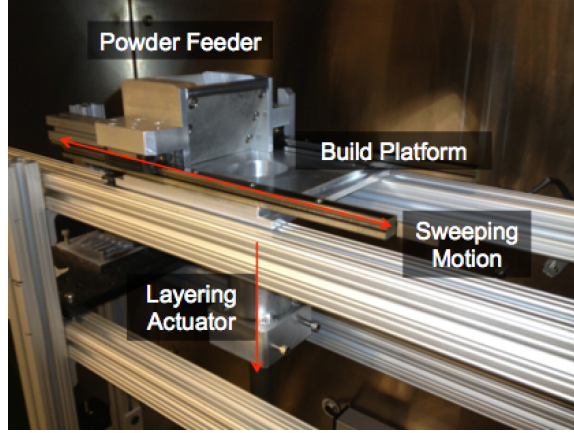
Figure 32: Layering system in the controlled atmosphere processing chamber with a gravity fed powder hopper and 2-axis motion.

3.2.4   Thermal Imaging Camera

A Mikron MCS640 thermal imaging camera is the main instrument providing data to be used in closed-loop feedback control of the SLE process. The thermal camera provides a temperature field for the whole processing zone at a rate of up to 60Hz, which is the limiting rate on the real-time control scheme. The thermal imaging camera utilizes a microbolometer array to measure the infrared energy emitted by an object and turn it into an electrical signal. The energy radiated from a theoretical ideal blackbody source is described by Plank's Law, shown in Equation 5:

$$W_\lambda(T) = \frac{2\pi h c^2}{\lambda^5 \left(e^{\frac{hc}{\lambda k_b T}} - 1 \right)} \tag{5}$$

where W_λ is the radiant energy emitted from the surface of the black body, T is its absolute temperature, λ is the wavelength of the emitted radiation, k_B is the Boltzmann constant, h is Planck's constant, and c is the speed of light. A blackbody is a theoretical surface which absorbs and re-radiates all the energy it receives while not reflecting or transmitting and of that energy. An ideal blackbody does not exist but the radiant energy emitted by a real non-ideal "gray body" object can be related

44

to the ideal emittance by the relation in Equation 6:

$$\epsilon = \frac{W_o}{W_{bb}} \tag{6}$$

where ϵ is the emissivity of the object, W_o is total radiant energy emitted by the object at a given temperature T, and W_{bb} is the total radiant energy emitted by a blackbody at a given temperature T. For a black body, the emissivity and absorptivity are equivalently 1. In an actual object though, some of the radiation is transmitted through the object and some is reflected back, resulting in the following relation:

$$\alpha + \tau + \rho = 1 \tag{7}$$

where α is the absorptivity or equivalently the emissivity of the object, τ is the transmissivity, and ρ is the reflectivity. The total radiant energy emitted by the object is found by integrating Plank's Law from 0 to infinity, resulting in the Stefan-Boltzmann law shown in Equation 8:

$$W = \epsilon \sigma T^4 \tag{8}$$

Where W is the total radiant energy emitted by the body, ϵ is the emissivity of the object, σ is the Stefan's constant, and T is the temperature of the object. Assuming a constant emissivity with respect to frequency, this equation can also relate the amount of energy emitted by a particular frequency range to a unique temperature.

Internally to the camera, the total radiant energy measured by each pixel is represented as a 16-bit energy unit. These energy units are converted to a temperature using a factory calibrated function. The conversion between energy units and temperature can be requested via the camera's API. The camera calibration is listed in Table 4 for one of the three camera ranges and shows that the camera has been calibrated to measure temperatures within an accuracy of $0.5\% \pm 1°C$.

Table 4: Thermal camera NIST calibration table.

Actual Temperature $°C$	Display $°C$	Correction $°C$	Tolerance $\pm°C$	Uncertainty U=ku (k=2) $°C$
1100.0	1096.3	3.7	6.5	1.9
1200.0	1199.1	0.9	7.0	2.1
1300.0	1302.5	-2.5	7.5	2.3
1400.0	1401.5	-1.5	8.0	2.6
1500.0	1501.5	-1.5	8.5	2.9
1600.0	1600.2	-0.2	9.0	3.2
1700.0	1700.8	-0.8	9.5	3.5
1800.0	1803.8	-3.8	10.0	3.9
1900.0	1905.7	-5.7	10.5	4.3

The normal operating frequency range of the camera is 780nm to 1080nm but a notch blocking filter has been added to the camera to additionally block the 1060nm to 1080nm range such that reflected energy from the incoming laser beam is rejected. An overview of the thermal imaging camera characteristics is listed in Table 5 with a pictorial overview in Figure 33.

Table 5: Thermal camera characteristics characteristics.

Characteristic	Value
Tmperature Range 1	800 - 1200 $^\circ C$
Temperature Range 2	1100 - 1900 $^\circ C$
Temperature Range 3	1800 - 2700 $^\circ C$
Operation Wavelength Range	780 - 1080 nm
Notch Filter	1064$\pm$10 nm
Accuracy	0.5% $\pm$ 1 $^\circ C$
Uncertainty	10 $^\circ C$
IFOV	0.18 mm
MFOV	0.54 mm
HFOV	119.35 mm
VFOV	89.67 mm
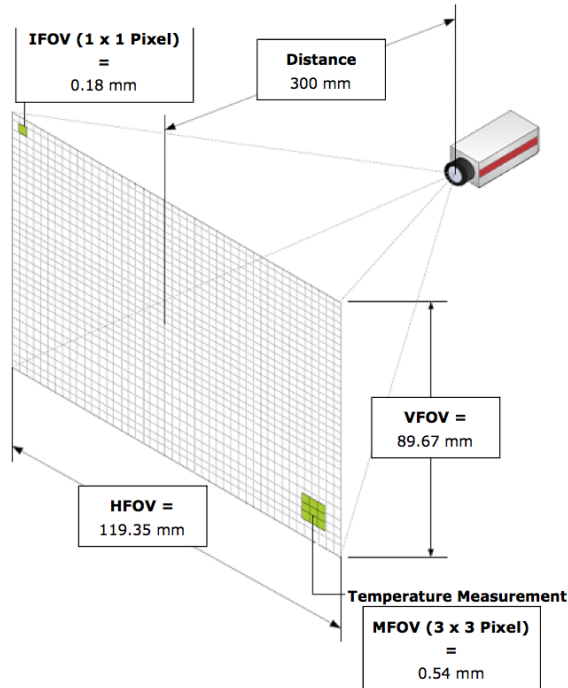
Figure 33: Overview of the thermal camera characteristics. Instantaneous field of view, IFOV, is the minimum spatial feature that can be resolved. Medium field of view, MFOV, is the minimum area for which a temperature measurement completely covers at least one pixel. HFOV and VFOV are horizontal and vertical fields of view specifying the size of the whole image plane.

Figure 34 shows a black body emission curve for an average temperature just above the liquidus temperatures of the materials studied in this dissertation, and illustrates the relatively low amount of emission below the 780nm camera cutoff at the typical measurement temperatures for this process.
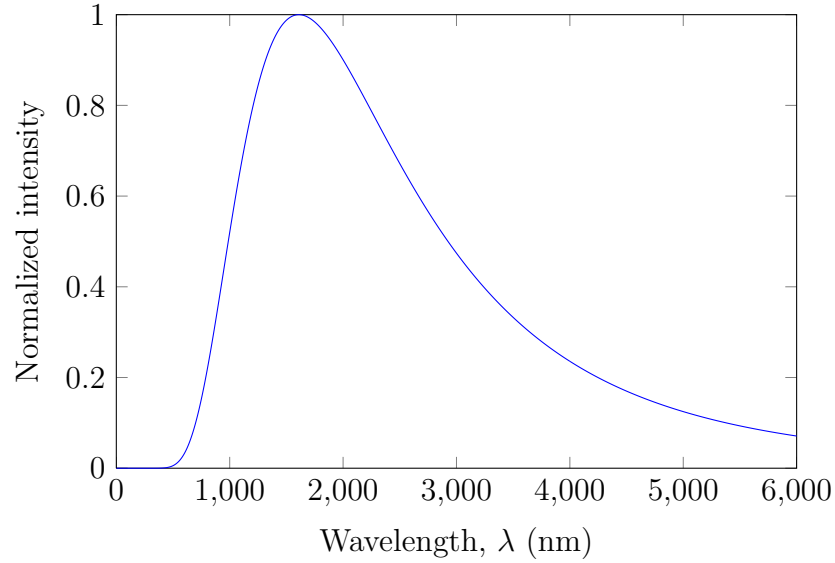
Figure 34: Plot of Planck's law for a surface at 1800K.

Additionally, the emission spectra for Nickel and Chromium, the two most significant alloying components in the studied materials, illustrate, in Figures 35(a) and 35(b), that there are a significant number of spectral emission lines within the 780nm to 1060nm band and thus if the emissivity is properly calibrated, the thermal camera will be able to measure the temperature of these alloys as configured.
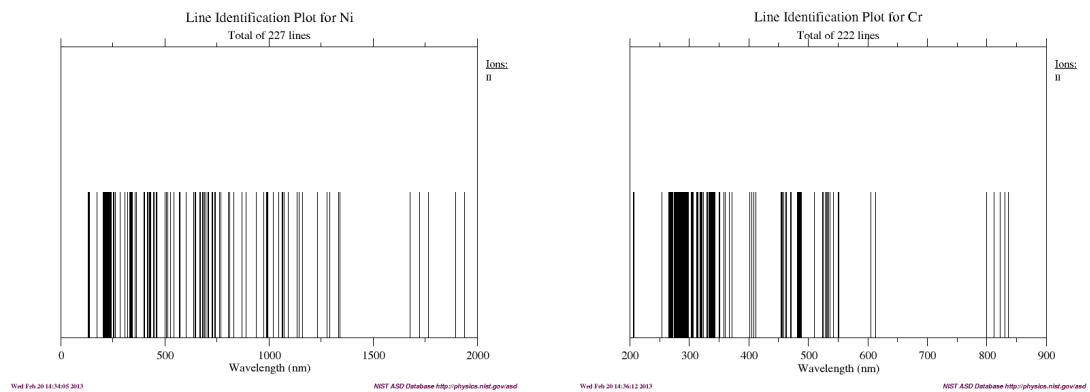
(a) Nickel Spectral Lines

(b) Chromium Spectral Lines

Figure 35: Spectral lines for major alloying components of the Ni-superalloys investigated [56].

Determining the emissivity of René-80 was done using two methods, the first method was used to determine the emissivity at the melting point of the alloy using a method similar to the one described in the work of Ghaemi [57] which involved measuring the temperature of a material as it cooled and matching the freezing point to the known freezing point of the material to calibrate an emissivity value for that material at the freezing point. For the purposes of this dissertation, the emissivity was approximated for a temperature between the solidus and liquidus temperatures by defocusing the laser beam and using a low power to slowly heat up and melt a sample of the René-80 material while the thermal camera measured the average temperature of the laser spot location. A curve such as the one illustrated in Figure 36 was then generated for a particular emissivity value.
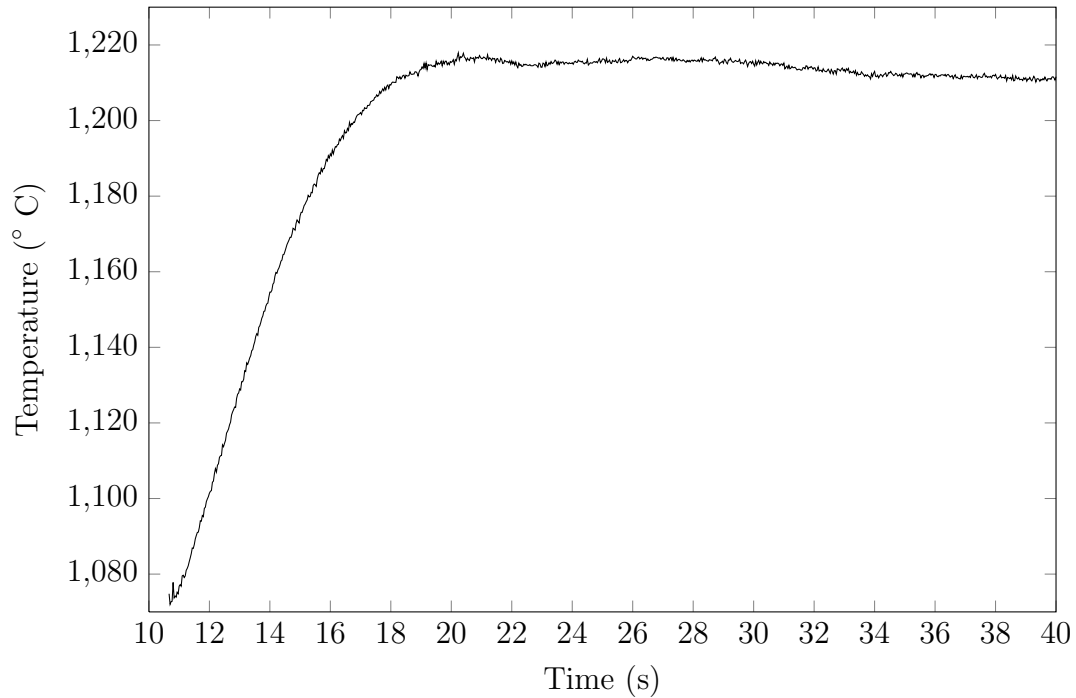
Figure 36: Temperature as a function of time for heating a René-80 substrate with a low power 100W defocused beam and measured at an emissivity value of 0.52. This emissivity results in a plateau in temperature at the solidus temperature of René-80.

The emissivity value was then altered until a curve with the plateau at the solidus

temperature of René-80 was measured. The emissivity value for René-80 was found to be 0.52 at the solidus temperature, which is near the emissivity value of 0.4-0.5 reported for partially oxidized molten Ni-base superalloys in literature [58, 59]. The sensitivity of the thermal camera temperature measurement to changes in emissivity was also approximated by adjusting the emissivity value and seeing how the plateau temperature changed as a result. It was found that around the nominal emissivity value of 0.52, every 0.01 change in emissivity resulted in approximately an $18°C$ change in the apparent temperature. At the temperatures typically viewed during the SLE process, this results in approximately 1.1% temperature error for every 0.01 or 1% change in the emissivity value. The second method to measure the emissivity value only worked for temperatures below the melting point of the material and is described in detail in the next section, which covers the operation of the emissivity correcting pyrometer instrument.

3.2.5 Emissivity Correcting Pyrometer

A specular configured Pyrofiber PF-1550 emissivity correcting pyrometer was additionally implemented to assist in the emissivity calibration of the thermal imaging camera for temperatures other than the liquidus temperature of the material in question. This method of calibrating the thermal camera emissivity involved the comparison of the measured temperature of the thermal camera with the temperature measurement from another calibrated device, in this case a non-contact pyrometer.

The main principle of operation of a typical non-contact thermal measurement pyrometer is similar to the operation of the thermal camera in that is is based on measuring the amount of radiant energy emitted by a source and using Plank's radiation law and the Stefan-Boltzmann relationship except that it only measures the temperature of a single spot. Although a typical pyrometer would involve the same issues as the thermal camera in requiring a proper emissivity value to calculate an

accurate temperature, an emissivity correction pyrometer such as the PF-1550 also includes a pulsed 1550nm laser that is used to directly measure the reflectivity of the object by measuring the amount of the 1550nm beam that is reflected off of the surface of the object. The amount of measured 1550nm laser power is compared to the output laser power and the emissivity is then calculated using Equation 7 with the transmissivity taken as 0 for an opaque object. This measured emissivity value is then used to correct the measured temperature of the pyrometer resulting in two separate measurements, a measured temperature and a more accurate emissivity corrected temperature. The PF-1550 pyrometer operates in a 70nm wavelength band centered around 1550nm and is capable of measuring temperatures in the range of $400 - 2000°C$ with an accuracy of $\pm 3°C$. The emissivity and radiance measuring instruments in the pyrometer were individually factory calibrated using a reflection standard and a black body furnace respectively.

The emissivity corrected temperature was used to calibrate the temperature reading of the thermal imaging camera using a series of experiments in which the focused laser beam heated a polished René-80 sample which the thermal imaging camera and pyrometer concurrently took temperature measurements. The emissivity of the thermal camera was then adjusted until the temperature reading of the thermal camera and the emissivity corrected temperature reading of the pyrometer were the same.

Prior to operating the pyrometer, the reflectivity of a polished René-80 sample was factory calibrated by Pyrometer Instrument Company as compared to a NIST certified specular reflection standard. The polished René-80 sample had a measured reflectivity of 0.676. The pyrometer setup was then calibrated to account for the loses through the window of the atmospheric processing chamber by first adjusting the angle of the pyrometer perpendicular to the René-80 sample until the amount of reflected 1550nm laser power was maximized. Once the measured power was maximized, the instrument was calibrated to take this amount of return power as a 0.676 reflectivity

measurement. Figure 37 illustrates the setup of the pyrometer and thermal imaging camera.
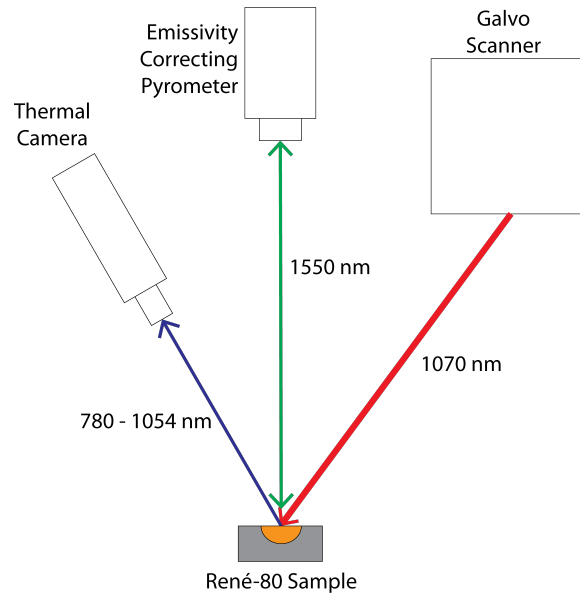
Figure 37: Overview of the pyrometer and thermal imaging camera calibration setup.

Figure 38 shows both a temperature measurement and corrected temperature measurement from the pyrometer for a range of temperatures below the melting point of René-80.
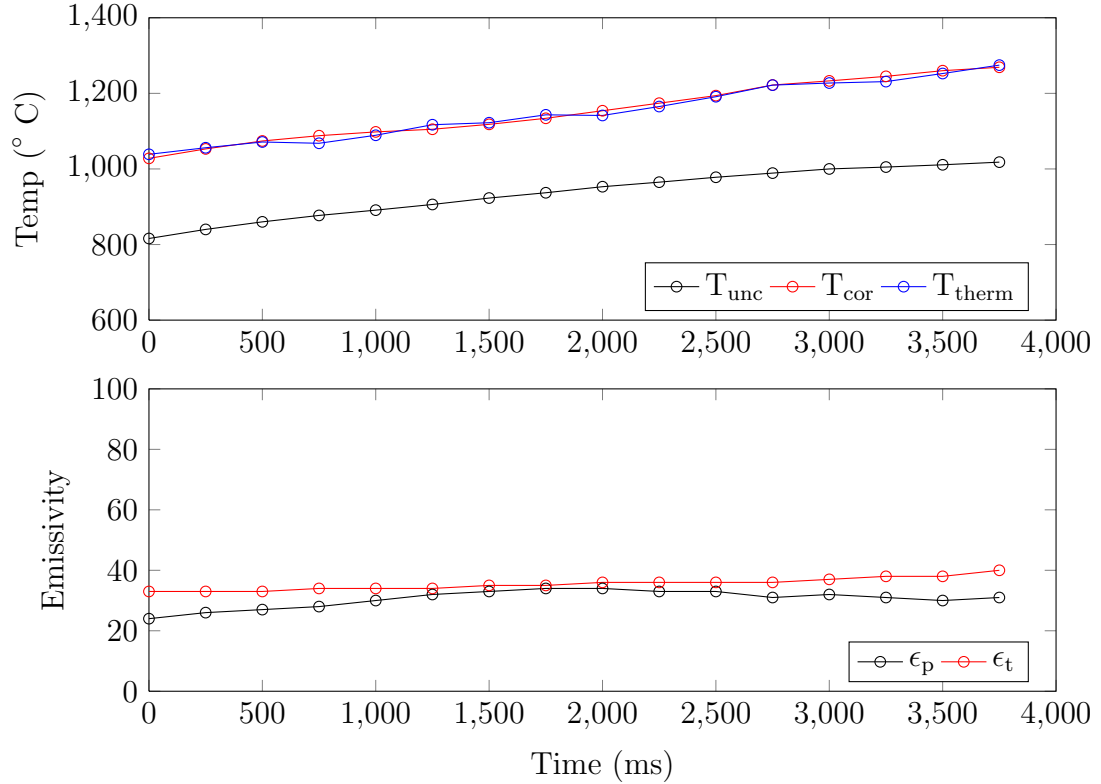
Figure 38: Calibration of thermal camera against the emissivity correcting pyrometer. Measurements reported by the emissivity correcting pyrometer and thermal camera for René-80 heating with a 300W focused beam.

In Figure 38 the uncorrected pyrometer temperature is T_{unc}, corrected pyrometer temperature is T_{cor}, corrected thermal camera temperature is T_{therm}, measured pyrometer emissivity is ϵ_p, and the adjusted thermal camera emissivity is ϵ_t. Temperatures above the melting point could not be measured by the specularly calibrated pyrometer because the melt pool meniscus that formed during melting altered the angle of incidence and return path of the 1550nm laser, causing incorrect emissivity measurements. Comparison of the emissivity data collected by the pyrometer and adjusted emissivity values of the thermal camera show that the emissivity below the melting point of René-80 is approximately 0.35-0.40 when viewing from the thermal camera. This range of values was similar to values found for other Ni-superalloys

such as IN718 in literature [60]. It also showed the similar trend of increasing slightly as temperature increased. Values below 1000 °C were not measured due to the lower bound on the operating range of the thermal camera.

3.3   Software

3.3.1   Overview

All of the hardware components including the laser, scanner, DAQ, thermal camera and layering system are tied together in a software package developed in C# specifically for this research project. The software is capable of importing XML job data, producing rectangular raster scan patterns of specified parameters, streaming marking commands to the scanner on the fly, controlling the laser power, and measuring and analyzing temperature field data acquired by the thermal imaging camera at a rate of 60 Hz. An overview of the C# software is shown in Figure 39.
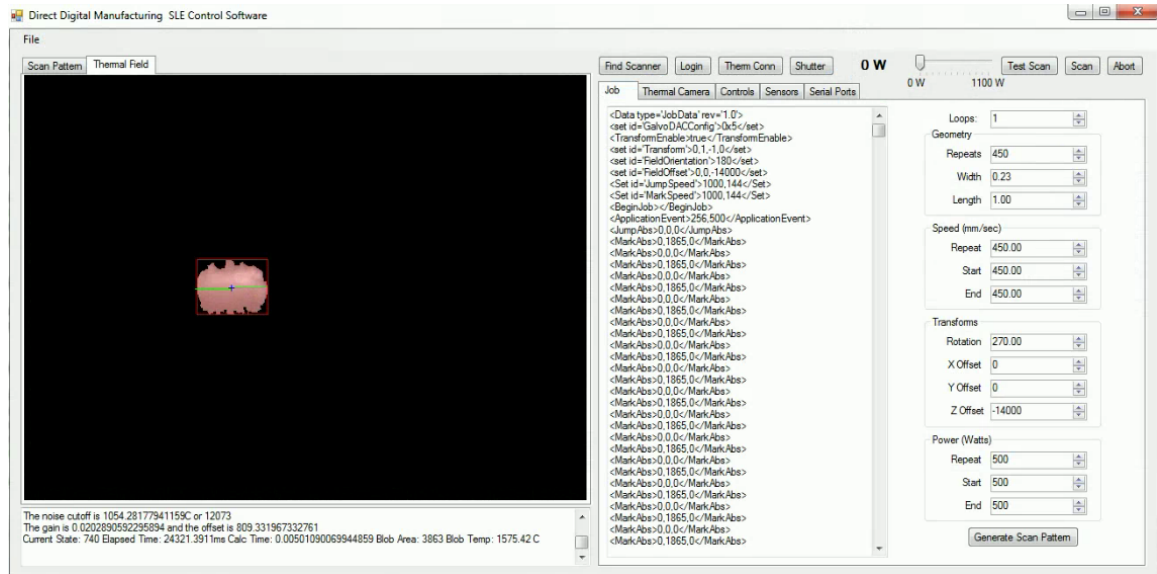
Figure 39: Overview of the custom C# software to control the SLE process showing job generation and thermal image processing/melt pool detection via thermal imaging camera.

Particular care has been taken to ensure that real-time control schemes can be

implemented in the software with the capability of controlling the laser scan speed and scan power on the fly rather than generating scan paths and power information on a layer-by-layer basis, as is typical of other additive manufacturing processes. Additionally, area filling and scan path generation algorithms can be implemented in the software and tied together with the laser power control schemes. With the implementation of a CAD file slicing mechanism to obtain layer information, the software will be completely standalone, self-sufficient, and will be suitable for potential implementation in commercial equipment or for use by other researchers.

3.3.2 Process Control

The four main parameters controlling the SLE process are the scan path, scan speed, number of preheat repeat scans, and laser power. In the initial development of the SLE process in this dissertation, each of these parameters was held fixed during a run, though through further developments, the parameters began to be adjusted in real-time using a feedback control system. An overview of the raster scan paths used in the SLE process is shown in Figure 40 in which the laser path is indicated by the arrows.
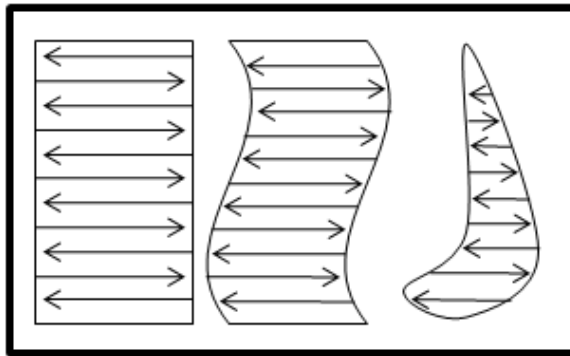
Figure 40: Typical raster scan patterns.

There are two types of scans currently used in the SLE process. The first type, the repeat scan, is used to initiate an incipient melt pool formation as well as partially

pre-heat the underlying substrate. The second type, the raster scan, causes the melt pool to smoothly propagate across the substrate and creates the resulting epitaxial growth. These scans are illustrated in Figures 41(a) and 41(b).

(a) Repeat scans   (b) Raster Scans
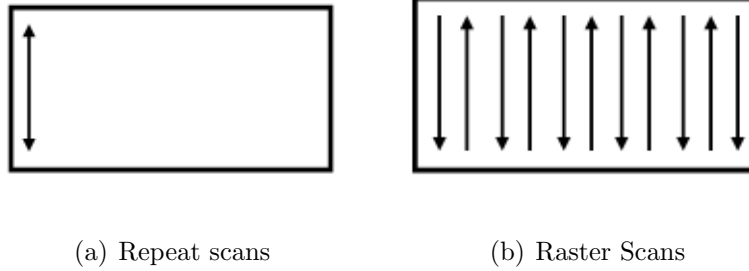
Figure 41: Types of scans used in the SLE process.

As will be discussed in the Chapter 4 of this dissertation, the four main processing parameters have a profound impact on the type and quality of epitaxial growth that is formed off of the underlying substrate. It is necessary to carefully control the number of repeat scans to avoid both excess deposit formation at the starting edge and excess preheating of the substrate which can lead to excessive residual stress buildup, substrate warping, and crack formation. It is also critical to carefully select the scan speed and laser power such that the temperature gradients created during processing lead to proper microstructural growth, as has been discussed in Chapter 2. For purposes of analysis, the four processing parameters for a simple raster scan pattern can be combined in the following way to provide a measurement of the overall energy density applied to the powder and substrate by the incident laser beam. The energy density, E_d, is taken as shown in Equation 9:

$$E_d = \frac{P}{S \cdot H} \tag{9}$$

where P is the laser power, S is the scan speed, and H is the scan spacing. The energy density can also take into account the powder thickness, resulting in the volumetric

energy density, E_{dv}, shown in Equation 10:

$$E_{dv} = \frac{P}{S \cdot H \cdot T_p} \tag{10}$$

where T_p is the powder thickness. Using these two relationships, processing maps can be developed that succinctly relate all of the major process parameters to the resulting deposit quality, as is discussed in Chapter 4.

3.3.3 Laser Scan Control

Control of the galvanometer laser scanners is done via a ScanMaster 1000 (SM1000) scanner controller and operates using an X-Y-Z rectangular coordinate system. The field size of the scanner at a particular working distance from the exit of the scanner is given by Equation 13:

$$FS = 2 \cdot W_d \cdot tan(\alpha_s) \tag{11}$$

where FS is the field size in meters, W_d is the working distance to the substrate, and α_s is the angle over which the scanner can operate, which in the case is $22°$. The scanner controller divides the angular position of the scanner into 65536 or 2^{16} subdivisions. Taking into account the angular subdivision, the minimum grid spacing on the rectangular X-Y plane can be represented by Equations 12 and 13

$$G = \frac{FS}{65536} \tag{12}$$

$$G = \frac{2 \cdot R \cdot tan(22°)}{65536} \tag{13}$$

where G is the minimum grid spacing. For the case of the 3-axis Cambridge scanner used in this dissertation, the typical working distance is about 230mm, resulting in a minimum grid spacing of $2.8\mu m$. The Z-axis controlled by the dynamic focusing module is also controlled using a 16-bit input and is capable of focusing over a range of $\pm30mm$ around a center point, resulting in a spacing of about $1\mu m$. The SM1000

controller divides each scan vector into a series of small steps, the size of which is user defined. The step size (SS) is defined in terms of a multiple of the grid spacing unit, G. The step period (SP) is also user defined and specifies the length of time over which one step is traversed during a scan. Combining the step size and step period results in the overall scan velocity defined in Equation 14:

$$v = \frac{SS \cdot G}{SP} = \frac{2 \cdot R \cdot tan(22°)}{65536} \frac{SS}{SP} \tag{14}$$

The scan spacing parameter in a raster scan pattern is defined as the space between each subsequent line scan and must be a multiple of the grid spacing. In prior direct SLS processes, fine scan spacings on the order of $5-20\mu m$ were found to be desireable for full density processing and high quality surface finish [39]. A scan spacing of $12\mu m$ was fixed most most trials involved in this dissertation.

Control of the SM1000 scanner unit is done using a software API accessed via the C# software. The SM1000 unit interprets job data in the form of XML files and converts the job into scanner commands that drive the 3-axis scanner unit. Typically, jobs are run with a full single layer XML job file being sent from the C# software to the SM1000 unit in a single transmission. The C# software is also capable of continuously streaming commands to the SM1000 unit which contains a buffer for the incoming command stream and allows for streaming of priority commands that can interrupt and modify the current scan job.

3.3.4 Thermal Feedback

The SLE software accesses images captured by the thermal imaging camera at a rate of 60Hz via a common object model software API. This image data is represented by 640x480 pixels of 16-bit data representing the accumulated energy value for each pixel. Alongside this image data, the camera also reports a minimum temperature range and maximum temperature range value associated with the current operating range of the camera as well as the chosen emissivity and transmissivity values for

the particular run. Conversion between accumulated energy values and temperature is handled in the SLE software according to the following procedure. A 16-bit gain value is first generated using the lower and upper temperature ranges as shown in Equation 15:

$$gain = \frac{T_{top} - T_{bot}}{65536} \tag{15}$$

where T_{top} is the maximum temperature the camera can currently measure, and T_{bot} is the minimum temperature. After multiplying the accumulated energy units, E_{acc}, by the gain, the temperature is offset from the minimum temperature, as shown in Equation 16, resulting in a temperature reading T in $^{\circ}C$.

$$T = E_{acc} * gain + T_{bot} \tag{16}$$

It should be noted that these gain and offset values are a function of the current range, emissivity value, and transmissivity value and must be requested from the camera and recalculated every time these values are changed.

Detection of the melt pool generated during processing using the thermal imaging camera is the basis for the feedback control schemes implemented in Chapter 5. Image processing in the C# code is facilitated by using the EmguCV wrapper for the OpenCV platform developed by Intel for use in machine vision and other image processing software. The EmguCV platform efficiently computes several image processing techniques such as conversion between color and greyscale, Gaussian blurring, and image gradient calculation.

3.4   Summary

This chapter described the implementation of the hardware and software associated with the development of the SLE process. The key pieces of hardware implemented included a high power 1kW Ytterbium fiber laser, a 3-axis galvonometer scanning system, a controlled atmosphere processing chamber, a thermal imaging camera, and

a melt pool video microscope system. Several of the operating details for each of these pieces of hardware were also provided, including bandwidth capabilities and uncertainties. Two methods were also described that allowed for determination of the emissivity values for René-80, as measured by the thermal camera. It was found that below the solidus temperature of René-80, the emissivity was between 0.35-0.40 and at the solidus temperature it was 0.52. An overview of the various aspects of process control was also covered, including software development, types of scan patterns used, and what the process control parameters were. The main process parameters included input laser power, scan speed, number of repeat scans, scan spacing, and powder thickness. These parameters could be combined into single expressions of energy density and volumetric energy for analysis and development of process maps. Finally, the chapter concluded with a description of the galvanometer scanner controller and thermal camera APIs.

CHAPTER IV

SLE PROCESS DEVELOPMENT

This chapter describes the development of the SLE process and includes a discussion of material selection and preparation, experimental procedures, analysis methods and metrics, it finally concludes with discussions of promising process parameters for each material. In particular, the main goal of this chapter is to address whether the SLE process is capable of producing fully dense crack-free repair deposits of specified microstructure.

4.1   Material Selection & Preparation

Initial development of the SLE process as part of this dissertation started on Mar-M247 and later progressed to CMSX-4 and René-80 processing. Each of these Ni-base superalloys are precipitation hardened alloys, the components of which are listed in Table 1, and have been chosen primarily because of their common use in jet turbine engine components. Mar-M247 is a Ni-base superalloy created at Martin Marietta Materials that contains Tantalum for high temperature precipitation strengthening and Carbon/Boron for grain boundary strengthening. Mar-M247 is typically cast in an equiaxed or polycrystalline microstructure and is relatively easier to weld than the other materials presented in this dissertation due to it being a slightly lower temperature material and thus exhibiting an decreased viscosity at the processing temperatures encountered during SLE. Due to its relative ease of processing, Mar-M247, was the first material used to prove the concept of using SLE to produce fully-dense crack free deposits. CMSX-4 is another alloy commonly used in jet turbine components that is typically cast with single-crystal microstructure. CMSX-4 is an alloy developed by the Cannon Muskegon Corporation that contains Rhenium for

creep resistance at high temperatures. CMSX-4 processing experiments were used to demonstrate that the SLE process was capable of producing DS and SX microstructures. René-80 was the final alloy processed as part of this dissertation and is a high-temperature alloy developed by General Electric that is high in both Aluminum and Titanium concentration, leading to many weldability issues as discussed in the second chapter of this dissertation. René-80 was explored to gain an understanding of how the SLE process operated on previously thought to be "non-weldable" materials.

All of the powders used were produced by Praxair Surface Technologies through an atomization process and resulted in the powder sizes listed in Table 6.

Table 6: Powder particle size distribution for Mar-M247, CMSX-4 and René-80. Upper bounds represent the larger mesh sieve the particles first pass through and lower bounds represent the smaller mesh sieve used to filter out 90% of the remaining smaller particles.

Powder	Particle Size
Mar-M247	$44 - 88\mu m$
CMSX-4	$97 - 150\mu m$
René-80	$61 - 151\mu m$

The SEM images in Figures 42, 43, and 44 illustrate the spherical nature of the powders.
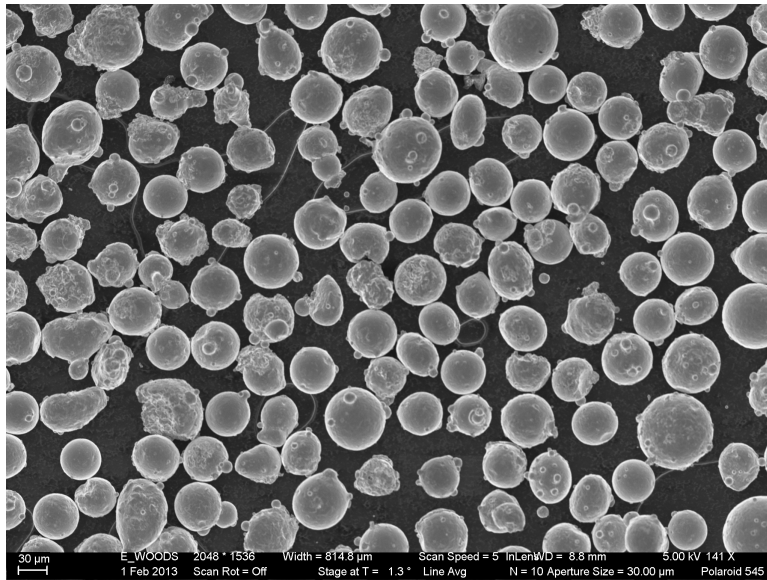
Figure 42: SEM image showing particle size distribution and spherical nature of the Mar-M247 powder.
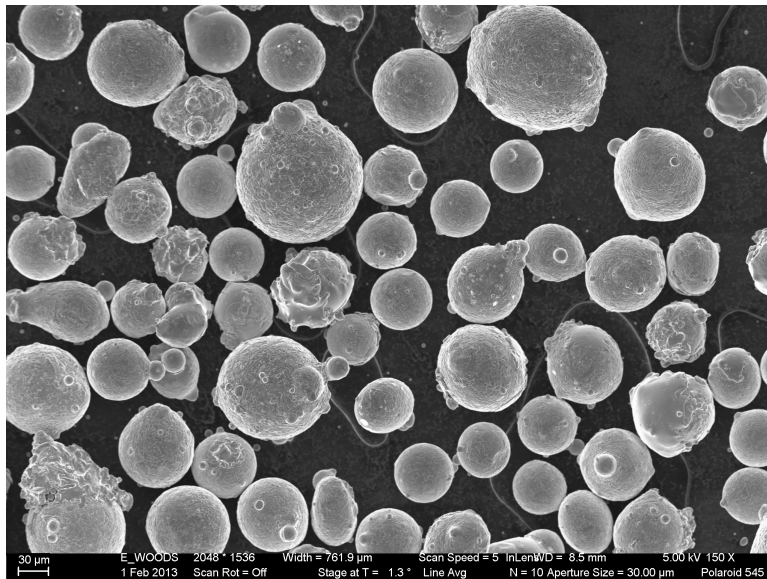
Figure 43: SEM image showing particle size distribution and spherical nature of the CMSX-4 powder.
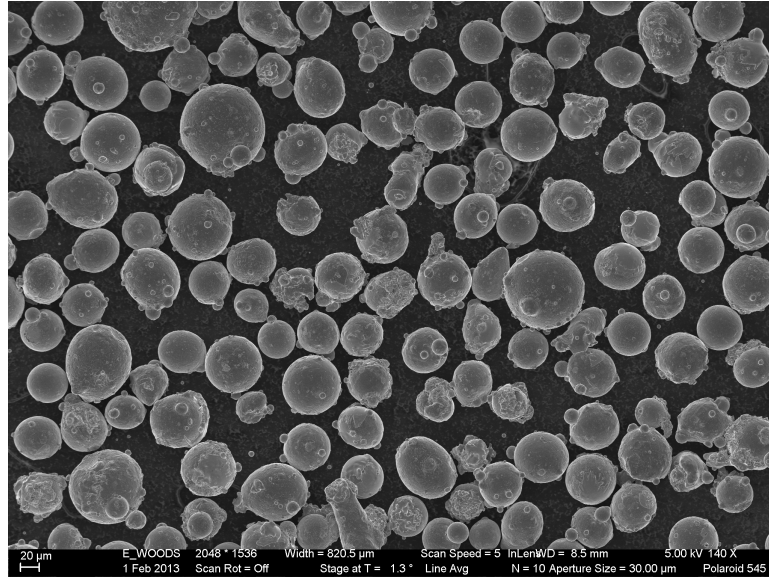
Figure 44: SEM image showing particle size distribution and spherical nature of the René-80 powder.

The spherical morphology of the powder causes it to fall into the moving linear melt pool at a consistent rate and aids in forming consistently smooth deposits. The packing density of the powder defines how much reduction in volume will be experienced when consolidating the powder and creating a fully dense deposit. The packing density of these powders is highly dependent upon the exact particle size distribution but for particles with sizes as listed in Table 6, the approximate void fraction will be between 0.35 and 0.45 [61], resulting in a 35-45% reduction in volume during powder consolidation.

Figures 45, 46, and 47 illustrate the small amount of porosity present in the powders used in this dissertation.
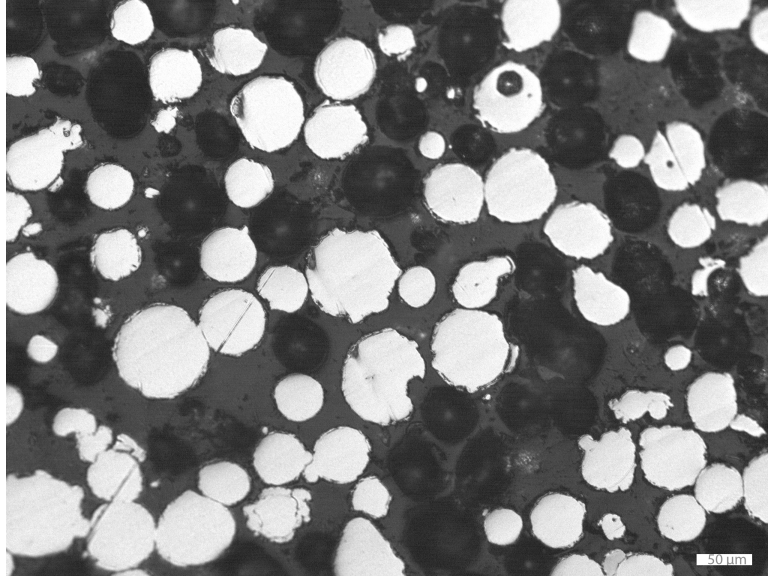
Figure 45: 100x optical image of Mar-M247 powder cross-section.
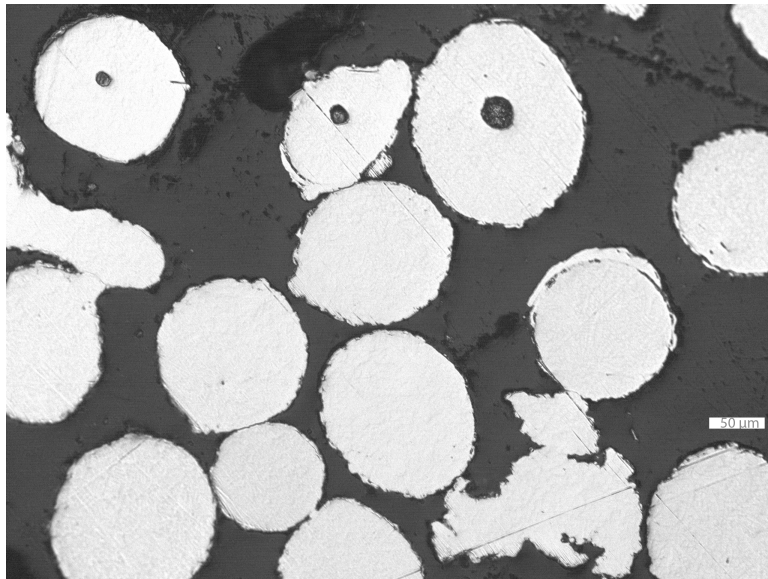
Figure 46: 100x optical image of CMSX-4 powder cross-section.
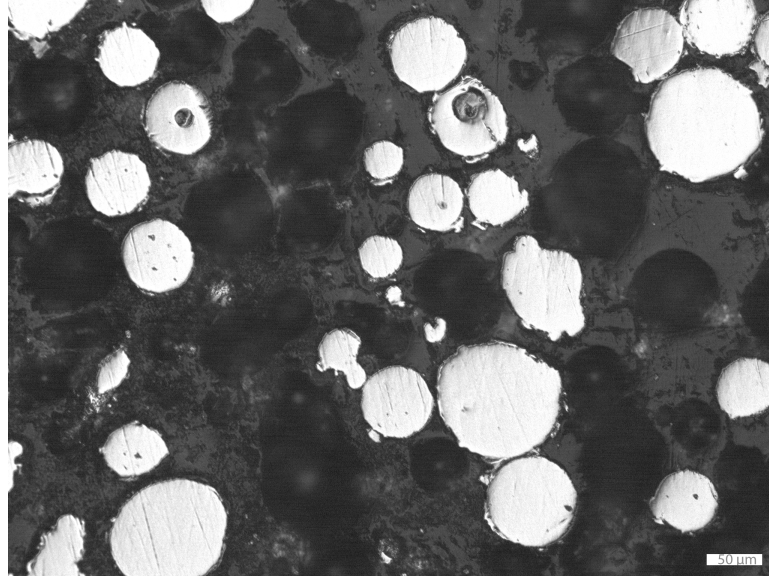
Figure 47: 100x optical image of René-80 powder cross-section.

It is unlikely that the small amount of porosity present in these powders would lead to any additional porosity in the resulting deposits due to the porosity size being small enough to insignificantly alter the overall void fraction of the powder.

Any adsorbed contaminants in the metal powder such as gases or moisture could volatilize during processing and would result in either oxidation at the free surface of the melt pool or creation of voids near the top of the deposited material as will be shown later in this chapter. To avoid these issues, all of the powders were degassed through a bake-out process in a $212°C$ vacuum oven at 70 cmHg vacuum for at least 24 hours. Prior to powder removal from the bake-out process, the chamber is backfilled with ultra-high purity 99.999% argon to prevent moisture or other gasses from being readsorbed onto the powder prior to SLE processing. It was found that this bake-out process significantly improved melt flow characteristics, reduced porosity in the resulting deposits and reduced the amount of oxidation discoloration at the top surface of the deposit.

4.2   Analysis Procedure

4.2.1   Optical Metallography

Metallurgical analysis of the samples is conducted by cutting a lengthwise cross-section through the center of the specimen and then cutting widthwise cross sections along the length using a Buehler IsoMet 4000 low speed sectioning saw, as illustrated in Figure 48.
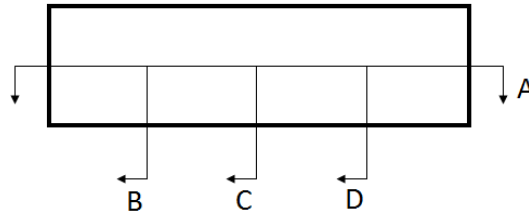
Figure 48: Locations where coupon samples are cut for analysis.

Each section is mounted in Bakelite using a Buehler SimpliMet 3000 compression mounting press. These mounts are then ground to a smooth finish using a Buehler EcoMet 250 automated polisher; starting at 60 grit sandpaper and progressively increasing to 1200 grit. The samples then undergo a rough polishing operation with $3\mu m$ and $1\mu m$ diamond solutions. Finally, the samples are smoothed to a mirror finish using a $0.5\mu m$ silica suspension. An overview of the polishing procedure is listed in Table 7.

Table 7: Overview of the polishing steps used to prepare Ni-superalloy specimens for optical metallographic analysis. Rotation indicates whether the platen holding the abrasive and the head holding the samples rotate in the same direction or opposite directions.

Abrasive	Force	Time	Rotation
60 Grit sandpaper	15 N	Until flat	Co-rotation
80 Grit sandpaper	15 N	2 min	Co-rotation
180 Grit sandpaper	15 N	2 min	Co-rotation
240 Grit sandpaper	10 N	3 min	Co-rotation
360 Grit sandpaper	10 N	4 min	Co-rotation
1200 Grit sandpaper	10 N	5 min	Co-rotation
$3\mu m$ diamond on satin	10 N	2.5 min	Co-rotation
$1\mu m$ diamond on satin	10 N	2.5 min	Co-rotation
0.5 silica on neoprene	10 N	5 min	Counter-rotation

The polished samples were then exposed to Kalling's No. 2 etchant composed of 50ml Ethanol, 50ml HCl and 2.5g $CuCl_2$, exposing the microstructure for microscopy. Imaging is completed using a Leica DM6000 optical microscope at varying levels of magnification. The DM6000 microscope was equipped with an X-Y gantry stage allowing for generation of macroscale images composed of 100 stitched together high magnification images. The level of detail present in the high magnification macroscopic images enabled algorithmic analysis of each chosen metric, as discussed in the next section.

To additionally verify proper crystal formation in the single crystal samples, a selection of CMSX-4 samples were also analyzed via electron backscatter diffraction (EBSD) analysis by a third-party company. EBSD analysis resulted in plots of crystal orientation in each specimen that were used to verify that the dendrite growth was within the misorientation tolerance level.

4.2.2 Analysis Metrics

Each specimen is analyzed to determine the height of the deposited material, the amount of meltback along the substrate, the number of stray grains formed, the locations of cracks or porosity, and the location of the columnar-to-equiaxed transition point if applicable. Although measurements of each of these metrics was initially done manually by measuring several discrete points along the sample length and averaging the values to determine the metric, over the course of this research, computer algorithms were developed to track each metric and capture all of the variations along each sample length. These algorithms are described in detail in the thesis work of J. Gambone [62]. An overview of the output of these algorithms is presented here as a prelude to what metrics were used to characterize the processing maps presented later in this chapter.

The image analysis software first isolates the samples and uses active contouring to detect the bottom and top of each sample, as illustrated in Figures 49 and 50.
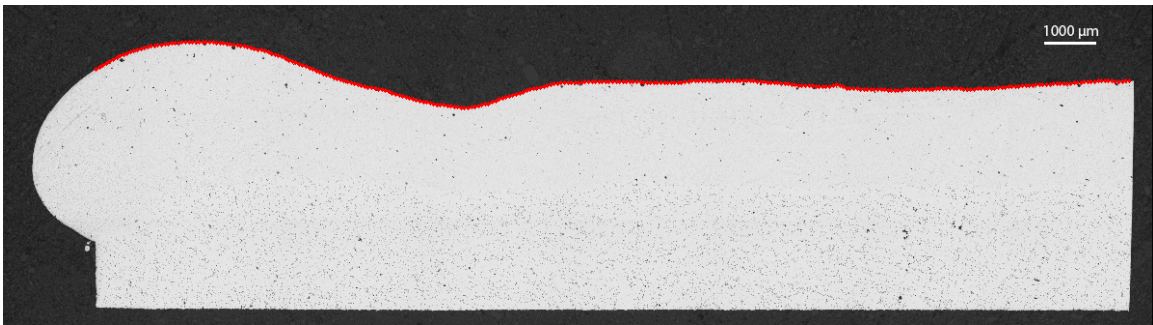
Figure 49: Tracked top of a sample overlaid with the image [62].
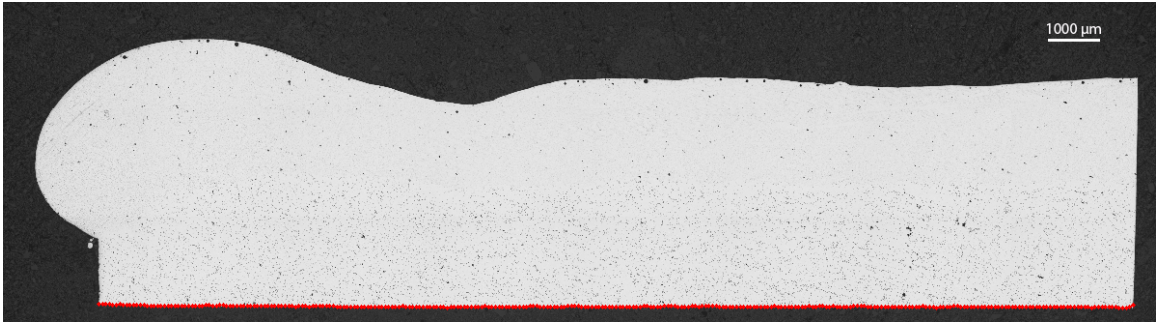
Figure 50: Tracked bottom of a sample overlaid with the image [62].

After isolating the sample, the software then operates in two modes, the first mode analyzes polycrystalline deposits such as those made using René-80 and the second mode analyzes single-crystal deposits such as those made using CMSX-4. For polycrystalline samples, the melt line is tracked, again using active contouring, as shown in Figures 51 and 52.
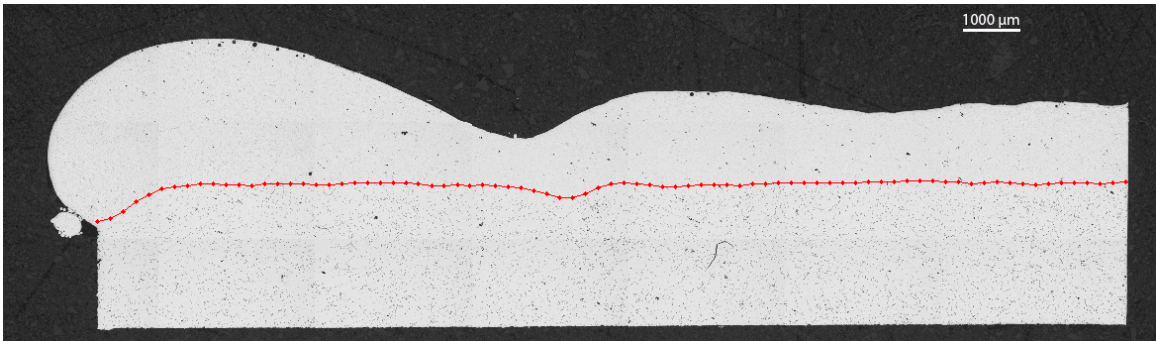
Figure 51: Melt back line tracked across an entire René-80 sample [62].

Figure 52: Closeup view of the René-80 meltback line [62].

71

Using the knowledge of the original sample height and the detected melt line, plots of the deposit height and melt back depth can be generated. The software also detects cracks and porosity in the deposits as illustrated in Figure 53.
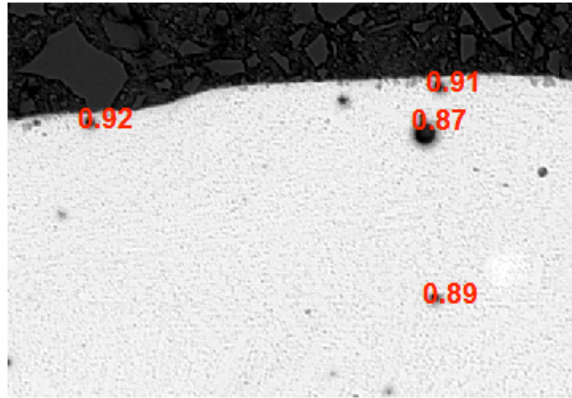
Figure 53: Pores found on a René-80 sample with level of circularity labeled for each [62].

Defects found with high circularity values are labeled as pores and those found with low circularity values are labeled as cracks.

Single-crystal deposits are analyzed using a combination of Canny edge detection and active contouring algorithms. Dendrite locations, angles, and widths are first tracked via the Canny edge detection routine as shown in Figures 54 and 55.
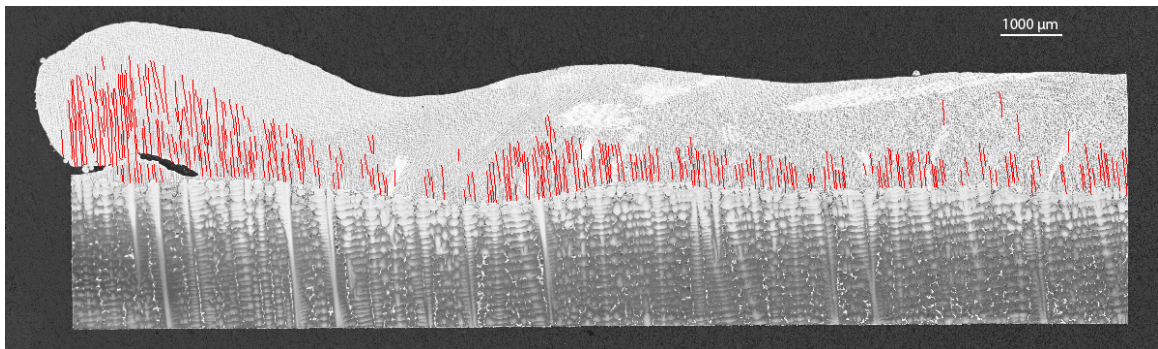
Figure 54: Accurate dendrites shown across an entire CMSX-4 sample [62].
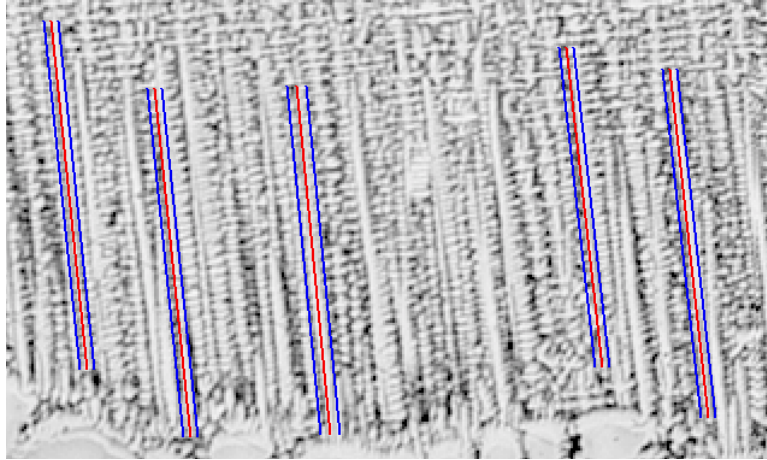
Figure 55: Dendrite width overlaid on a CMSX-4 image [62].

The dendrite termination points are then used to determine the SX termination line as illustrated in Figure 56.
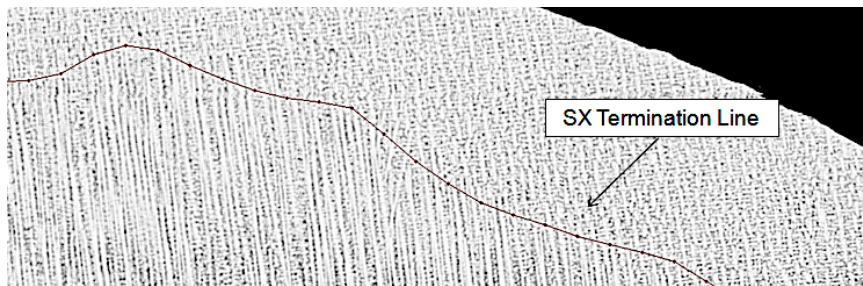
Figure 56: A close view of the SX termination point found with the active contouring [62].

The melt back line is found in a similar way using the lower termination point of the fine dendrites in the deposit. Combining the knowledge of the original sample thickness with the melt line, SX termination line, and overall tracked top line allows for generation of plots tracing the melt back depth, SX height, and overall deposit height respectively. Plots of dendrite width and angle as a function of location along the substrate length can also be generated. An overview of the metrics tracked is shown in Figure 57.
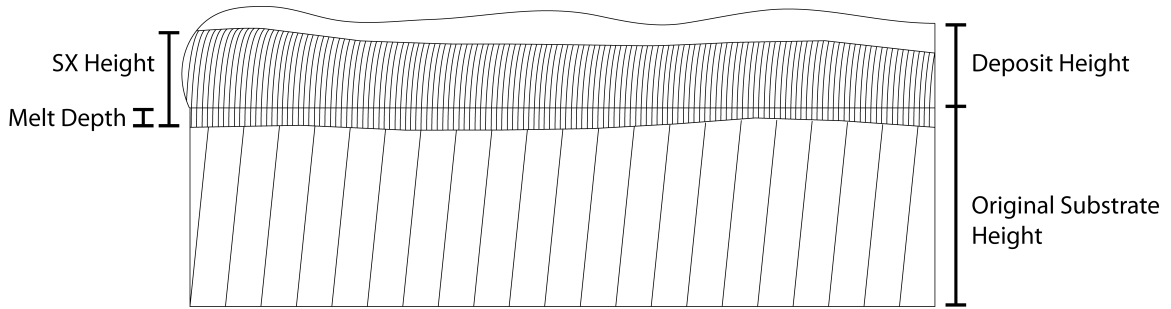
Figure 57: Overview of the measurement metrics used to determine sample quality for the process maps developed in this chapter.

4.3 Initial Process Development on Mar-M247 & Preliminary Observations

Initial development of the SLE process began in 2008 on the Mar-M247 alloy, due to it being a slightly lower temperature material and thus exhibiting a decreased viscosity at the processing temperatures encountered during SLE. This decreased viscosity and lower surface tension allows powder to fall into the melt pool more smoothly during melt line propagation, leading to higher quality, more uniform deposits. The initial SLE process development on the Mar-M247 and CMSX-4 alloys began using a dated Hobart 2.4kW Nd:YAG lamp-pumped laser. This laser had a much larger beam diameter, 1.5mm, and lower beam quality than the current laser. Additionally, it had a rather unstable laser power that could fluctuate up to 50W during processing. Despite these shortcomings, it was capable of demonstrating the capabilities of the SLE process on Mar-M247 and CMSX-4.

Processing of Mar-M247 was initially attempted as a proof-of-concept showing that the SLE process was capable of creating crack-free deposits of a Ni-base superalloy. All of the Mar-M247 trials were run using 76.2 x 19.1 x 2.54mm rectangular coupons with the maximum amount of unconstrained powder laid on top. The Mar-M247 parameter space included a laser power and scan speed range of 300-600W

and 100-300 mm/s respectively with a fixed scan spacing of $25.4\mu m$. Repeat scans were not necessary for producing high quality deposits on Mar-M247, due to the melt temperature being relatively low. The same chemistry Mar-M247 powder was spread evenly across the top of the coupon but due to the ball bearing like nature of the powder, it tended to form a mound in the middle of the coupon and slope off towards the outer edges as shown in Figure 58.
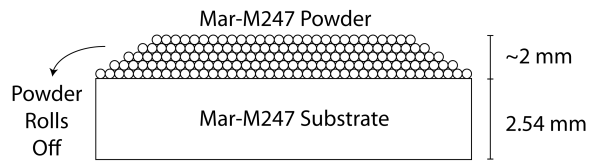
Figure 58: Illustration of the powder height variation across the width of a sample when powder containment is not used.

Also, due to there being no mold constraining the powder, the powder height could not be accurately measured for each trial. This lack of a mold container led to repeatability issues in the set of experiments run on Mar-M247. Nevertheless, several promising samples were produced on Mar-M247 at this early stage in the development of the SLE process. Figure 59 shows the uniformity and smooth finish of one of the deposits created on Mar-M247.
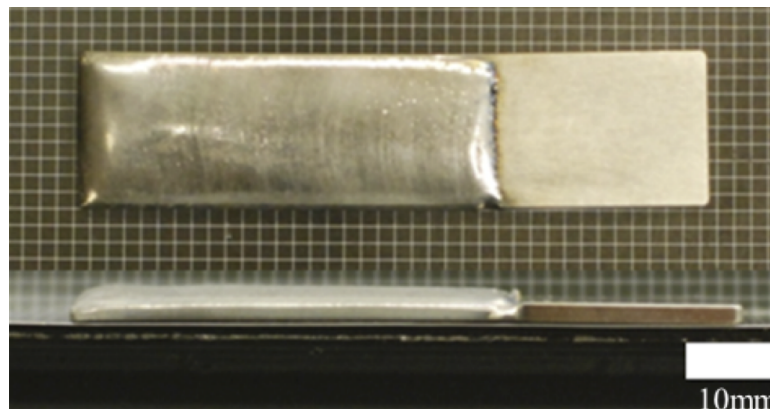
Figure 59: As processed MarM-247 sample

Two cross-sections as illustrated in Figure 60 were taken of each sample to analyze the results.
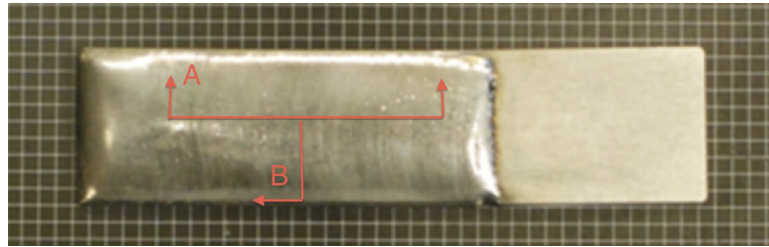
Figure 60: Cross sectional cuts taken of Mar-M247 samples.

Figure 61(a) shows a micrograph for a sample in the middle of the range of parameters indicating full bonding across the length of the sample, no cracking or porosity, and no significant substrate warping. Deposit heights were found to be 1.5-2.0mm from a single pass. Several of the Mar-M247 samples also underwent a post-process heat treatment for 4 hours in an Argon purged tube furnace at $1067°C$ to assess whether strain-age cracking would occur. Figure 61(b) shows a micrograph of a heat-treated sample showing no signs of porosity or cracking.
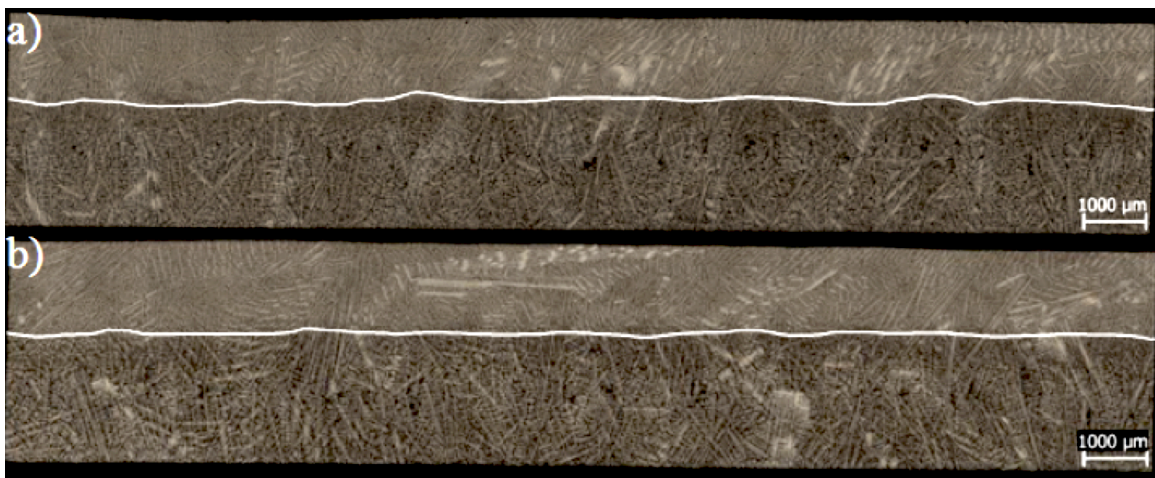
Figure 61: a.) As processed MarM-247 longitudinal section A view b.) Heat treated MarM-247 longitudinal section view. The white line depicts the boundary between the base substrate and added material.
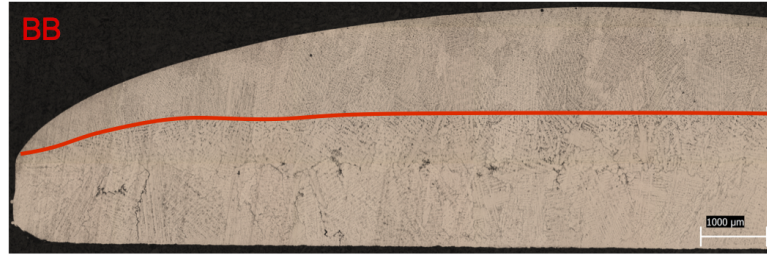
Figure 62: Widthwise section B of a Mar-M247 sample with red line indicating the bond line.

The widthwise cross section of a Mar-M247 sample in Figure 62 indicates the loss of deposit height towards the edges of the sample and shows that proper powder containment was required going forward.

Several key observations from the Mar-M247 trials were made. These observations are sumarized as follows: 1) Fully dense deposits were achievable 2) Metallurgical bonds were formed between the melt and base substrate and 3) Hot tearing, or stress cracking was not evident, even after post-process heat treatment.

Several challenges to overcome were also highlighted by these trials and are summarized as follows: 1) Powder containment would be required to make the SLE process more predictable and repeatable; 2) Properly correlated experimental results would require either in-process measurement of laser power or usage of a newer laser with less power fluctuations; and 3) High power/low scan speeds (high energy density) led to significant warping of the base substrate while low power/high scan speeds (low energy density) resulted in low substrate melt-back, indicating that a trade off would have to be made between having sufficient melt back and limiting substrate warping.

4.4 *CMSX-4 Single Crystal Process Parameter Development*

The next developments in the SLE process involved the creation of DX and SX microstructure deposits on CMSX-4 substrates. Taking into account the first and

second challenges identified in the Mar-M247 trials, the experimental procedure was modified over the course of several years to increase the repeatability and reliability of the process. The most significant change was the addition of a powder container or mold on top of the substrate. The powder container configuration went through several iterations illustrated in Figures 63(a) and 63(b) before finally settling on the setup illustrated in Figure 63(c).
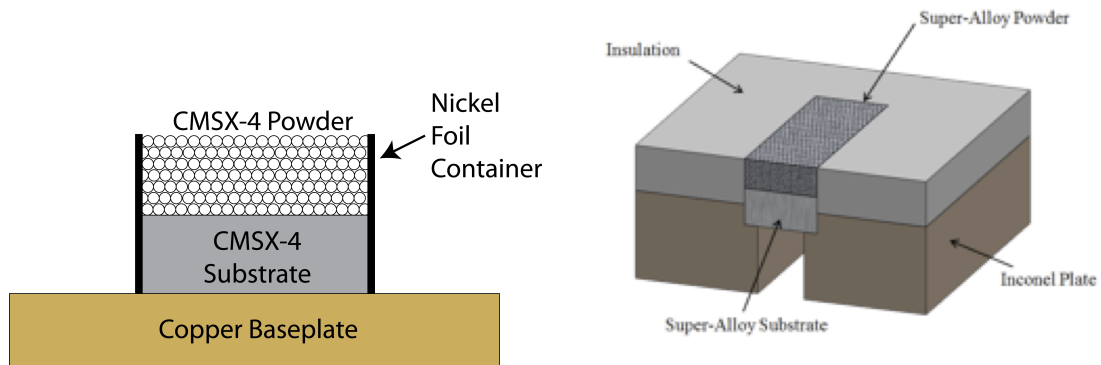
(a) Consumable nickel foil powder container.   (b) Consumable ceramic mold powder container.
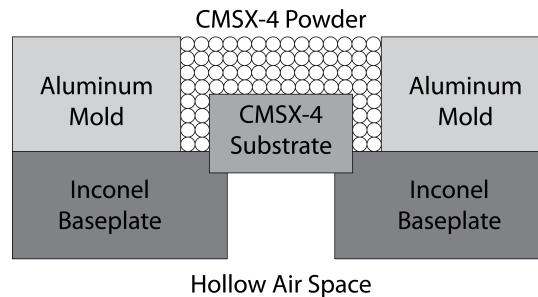
(c) Final setup showing the over sized aluminum powder container.

Figure 63: Various powder containers used during development of the SLE process.

As illustrated in the final setup, an over sized aluminum mold was used to hold a consistent height of powder on top of the substrate. The excess powder above the sides of the substrate allowed for additional feed powder to fall into the melt pool from the outsides and prevented powder starvation as the scan proceeded. It also allowed for high aspect ratio deposits without loss of epitaxy or deposit height towards the outsides of the sample. Additionally, the copper baseplate that was initially used as a sample holder was replaced with a specially machined Inconel 625 baseplate that

78

contained a hollow pocket beneath each sample, as illustrated in Figure 64.
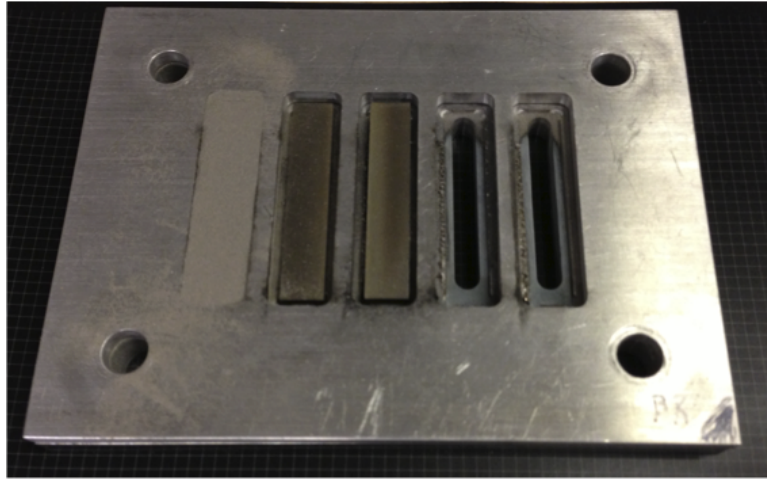
Figure 64: Baseplate and powder container used for processing CMSX-4 and René-80 samples. The right most positions show the hollow space under the samples, the middle positions show uncovered samples, and the left position shows a sample with powder placed on top and ready for processing.

This baseplate was meant to closely represent the processing conditions that would be present in operation of the SLE process on an actual turbine airfoil. Typical high-performance turbine blades have a hollow space below the tip cap that acts as a cooling passage and would significantly alter the heat transfer characteristics at the top of the blade. The hollow space in the baseplate was meant to represent this hollow space beneath a typical turbine blade tip cap. Additionally, Inconel 625 is a Nickel-Chromium alloy more similar in composition to CMSX-4 than the Copper that had been used before. Figure 65 shows a widthwise cut of a CMSX-4 sample illustrating the edge-to-edge columnar epitaxy of over 1mm height that can be produced using this setup.
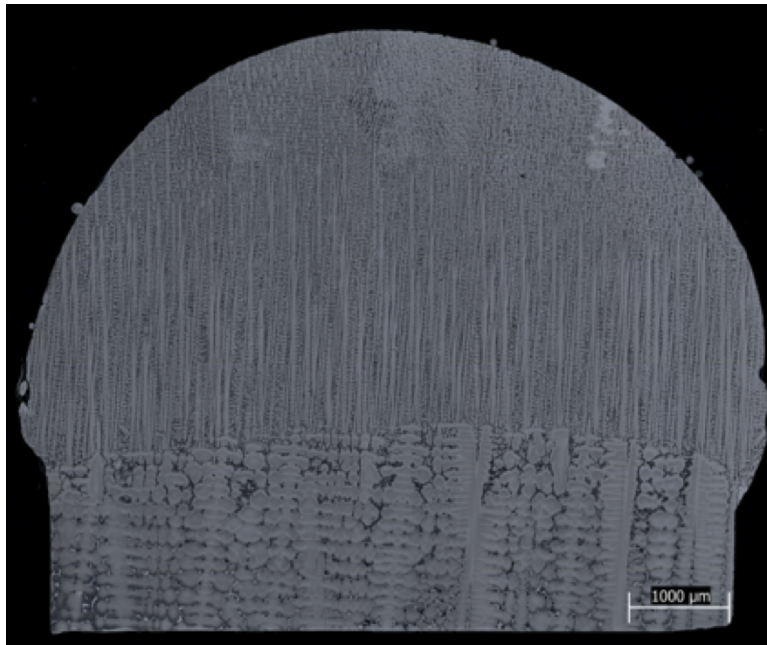
Figure 65: Cross-sectional cut of a CMSX-4 sample demonstrating no loss of epitaxy near the edges of the sample.

The second major change to the experimental setup involved the addition of a 95-5 beam splitter in the path of the laser, between the laser and the scanner unit, as illustrated in Figure 66.
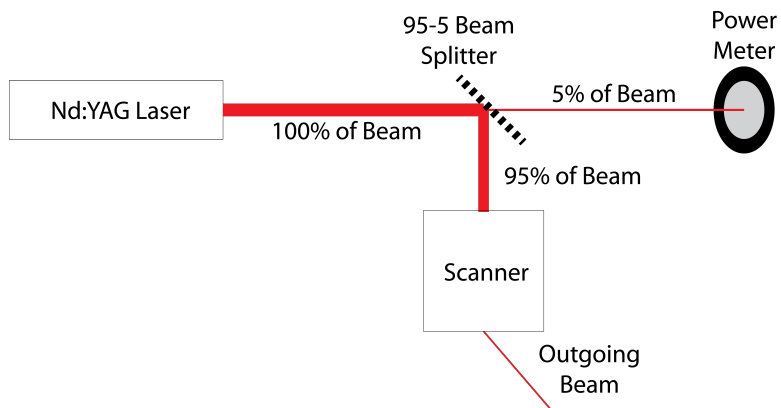
Figure 66: Illustration of the beam path used to measure 5% of the incident laser power during SLE processing.

This beam splitter caused 5% of the beam power to be split off and fed to a

Coherent FieldMaxII-TO laser power meter. This allowed for measurement of 5% of the laser beam power during processing and gave an indication of the actual apparent power during each experimental trial. Neglecting the small amount of power loss when passing through the scanner system, the actual laser power delivered to the substrate would be 19 times the measured value. This actual power could then be factored into the calculation of the energy density for that particular trial and was necessary to develop experimental processing maps due to the high amount of variance in the Hobart laser power between trials.

To additionally verify that the microstructure seen in the optical micrographs was indeed single crystal, electron back scattering diffraction (EBSD) analysis was conducted on a set of older samples exhibiting significant epitaxial growth. EBSD analysis can verify the SX growth and determine the degree of misorientation, if any, in the deposited material relative to the parent structure. Figure 67 shows a representative EBSD analysis.
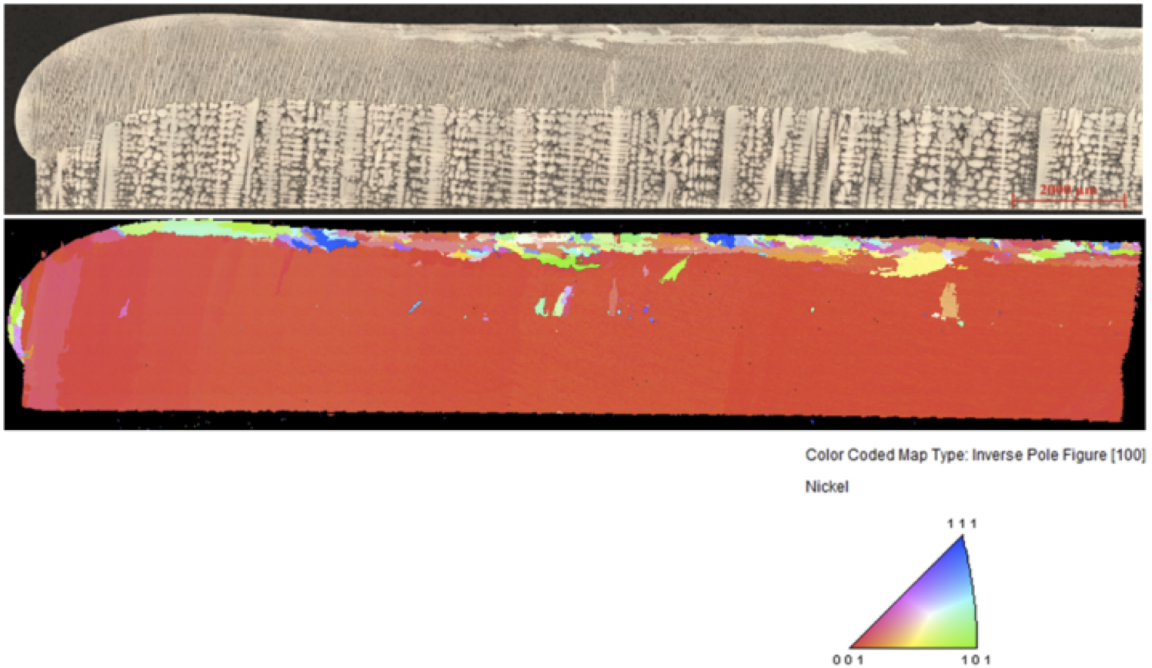
Figure 67: EBSD analysis of a CMSX-4 deposit

With the exception of the equiaxed cap and selected areas along the fusion line, excellent directional correlation exists between the deposited dendrite structure and the parent SX structure. The EBSD images show that the SLE process is capable of creating fully dense SX deposits.

4.4.1 Parameter Development

As demonstrated in the casting processes used to create single-crystal castings, the key to developing a single-crystal microstructure is proper control of the temperature gradients and velocities during melt solidification. The SLE process operates by remelting a portion of the underlying substrate and using that remelt to epitaxially grow a deposit on top of the substrate with similar microstructure. There are two main factors that differentiate SLE from prior processes and allow it to create DS and SX microstructures. The main factor in creating the vertical temperature gradients is the use of the high power laser beam to apply an extremely high temperature to the top of the melt pool. The second factor is the relative absence of powder bed and substrate preheating. Having a high power energy source and under heated substrate creates the temperature gradients required for DS and SX growth, as illustrated in Figure 68.
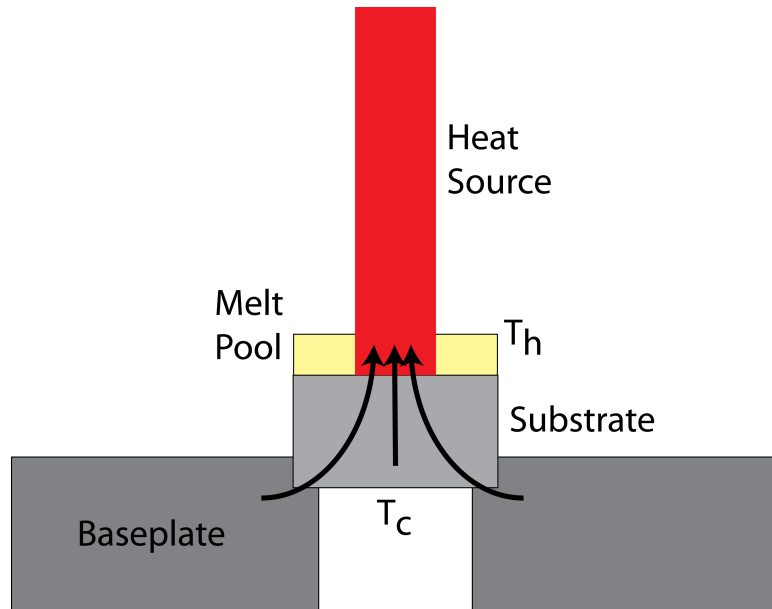
Figure 68: Illustration of the large difference between the high temperature, T_H, under the incident laser beam and low temperature, T_C, at the bottom of the substrate. The arrows indicate the temperature gradient that should be vertical in the solidifying melt pool for columnar growth.

Once the experimental setup was finalized as described earlier, many iterative experiments were run with parameters chosen by observation of prior runs until a set of parameters near the optimal range was developed. A set of experiments was then constructed to explore the effects of various processing parameters on the resulting microstructure within this subset of the entire parameter space. The parameter range explored included 50-100 repeat scans, scan speeds of 150-250mm/sec, laser powers of 400-600 W, and powder thicknesses of 1mm, 1.5mm, and 2mm. All samples were run with a fixed scan spacing of $25.4\mu m$ and had dimensions of 35.6 x 6.9 x 2.54mm. The scan spacing was fixed at an average value found to produce smooth deposits on prior related technologies such as Direct SLS [63]. An overview of these sets of experiments is listed in Table 8 with the energy density and volumetric energy density also calculated for each trial.

Table 8: Subset of CMSX-4 trials analyzed in the following section.

Sample Number	Repeats	Scan Speed (mm/s)	Total Laser Power (W)	Scan Spacing (mm)	Powder Thickness (mm)	Energy Density (J/mm^2)	Volumetric Energy Density (J/mm^3)
CMSX1	50	150	406	0.0254	2	106.56	53.28
CMSX2	50	150	468	0.0254	2	122.83	61.42
CMSX3	50	200	548	0.0254	2	107.87	53.94
CMSX4	50	200	586	0.0254	2	115.35	57.68
CMSX5	50	250	600	0.0254	2	94.49	47.24
CMSX6	100	150	416	0.0254	1.5	109.19	72.79
CMSX7	100	150	452	0.0254	1.5	118.64	79.09
CMSX8	100	200	490	0.0254	1.5	96.46	64.30
CMSX9	50	200	520	0.0254	1.5	102.36	68.24
CMSX10	50	250	584	0.0254	1.5	91.97	61.31
CMSX11	100	150	384	0.0254	1	100.79	100.79
CMSX12	100	150	424	0.0254	1	111.29	111.29
CMSX13	100	200	480	0.0254	1	94.49	94.49
CMSX14	50	200	510	0.0254	1	100.39	100.39
CMSX15	50	250	586	0.0254	1	92.28	92.28

The powder in each of these trials went through a 60hr long bake-out in the argon purged vacuum oven and was metered into the containing mold by weight. Once the powder was placed in the mold on top of the sample, each set of 5 samples was shaken on a vibrating table to allow the powder to settle and even out to the desired powder height.

4.4.2 Image Analysis

Several typical microstructural features present in deposits created at various processing parameters in the SLE process are readily demonstrated within this set of samples. Problematic microstructural features include lack of fusion, balling at starting edge, cracking, hot tearing, columnar to equiaxed transition (CET), and oriented to misoriented transition (OMT). Lack of fusion, found in several of the samples and illustrated in Figure 69, is a result of insufficient energy applied to the sample causing a lack of melting in the substrate.
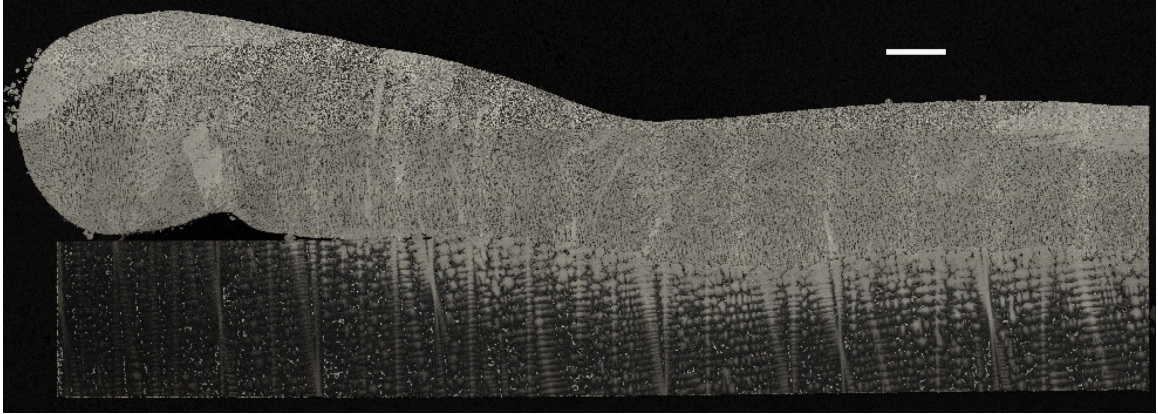
Figure 69: Length-wise cross sectional cut of sample CMSX8 demonstrating lack of fusion at the starting edge on the left side of the image. Scale bar is 1mm.

The samples that had 2mm of powder on top exhibited an extreme amount of lack of fusion at the starting edge or across the first 1/3rd of the sample. There are two conditions under which balling at the starting edge, illustrated in Figures 69 and 70, will occur. The balling in Figure 69 is caused by not providing enough repeat scans at a high enough power level to initiate the melt pool at the starting edge. Because the melt pool is not properly initiated, the molten powder is unable to adequately wet the substrate and forms a ball due to surface tension forces. The other form of balling illustrated in Figure 70 is caused by excessive repeat scans causing the melt pool to widen and accumulate too much powder from in front of the starting edge, resulting in a large deposit height at the start of the scan.
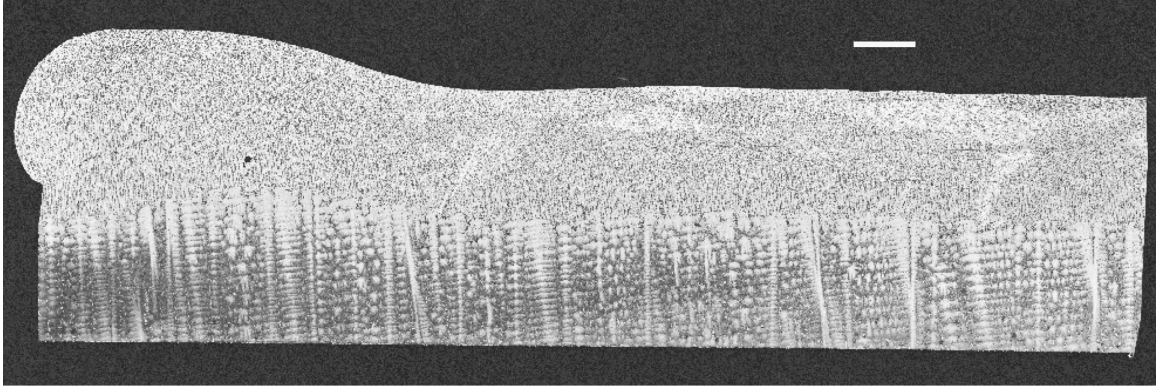
Figure 70: Length-wise cross sectional cut of sample CMSX13 demonstrating balling at the starting edge on the left side of the image. Scale bar is 1mm.

The effects of balling can be seen in all samples, but limiting the number of repeat scans also limits the amount of balling. A balance must be maintained between providing enough energy to initiate the melt pool while also not over melting the substrate or causing too much powder to be pulled into the initial melt pool. Alternative strategies for initiating the melt pool at the starting edge such as a slow ramp up of power may also limit the effect of balling.

Hot tearing or hot cracking, as illustrated in Figure 71, occurs in the fusion zone and is a result of stresses accumulating in a semi-solidified region.
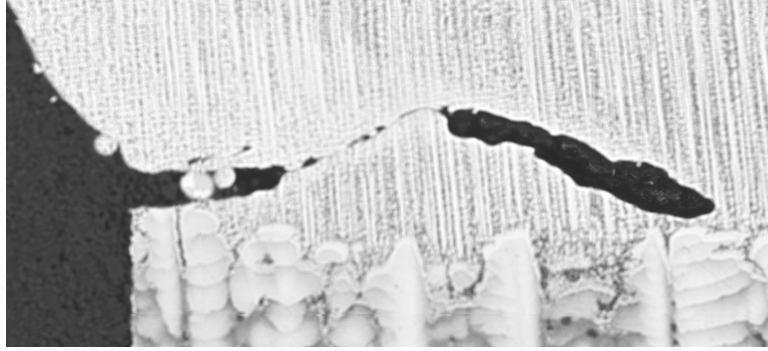
Figure 71: Length-wise cross sectional cut of sample CMSX11 demonstrating a hot tear at the starting edge on the left side of the image. This separation is labeled as a hot tear or crack as opposed to lack of fusion due to the formation of the columnar microstructure prior to cracking.

This cracking can happen at various combinations of scan speed and laser power, but it is rare due to the scan spacing distance being much smaller than the laser beam diameter in the SLE process, causing each location of the substrate to undergo a pre-heat and post-heat during melting and solidification respectively. This pre-heat and post-heat operation limits the rate at which the scanned area solidifies and reduces the accumulation of stress in the samples.

The CET, illustrated in Figure 72, typically occurs near the top of the deposit and is a result of an insufficient vertical temperature gradient in that location to drive the columnar growth.

Figure 72: Image demonstrating the CET in which the columnar structure in the lower left transitions into the equiaxed structure on the right.

The CET occurs due to the high localized temperature gradient directly under the incident laser beam and the relative inability to convect heat off the top of the melt pool. The OMT, illustrated in Figure 73, occurs due to an increase in the temperature of the substrate as the scan progresses, resulting in a flip in the direction in which grain growth occurs.

Figure 73: Image demonstrating the OMT indicated by the vertical columnar structure at the bottom of the image flipping to a horizontal columnar structure near the top of the image.

The direction of the solidification flips from $< 001 >$ (vertical) to $< 100 >$ (horizontal) when the predominant temperature gradient driving the solidification switches from the vertical direction, from incident laser spot to substrate, to the direction following the motion of the laser across the top of the sample. The height of the OMT occurrence typically decreases as the scan progresses due to the buildup of heat in the substrate as the scan progresses, reducing the temperature gradient in the $< 001 >$ direction and resulting in a lower $< 001 >$ columnar structure towards the trailing edge of the sample. The CET and OMT occurrences near the top of the deposit are two limiting factors on the height of columnar structure that is produced.

Several of the high energy density samples also indicated bending towards the latter half of the sample, as indicated illustrated in Figure 74.
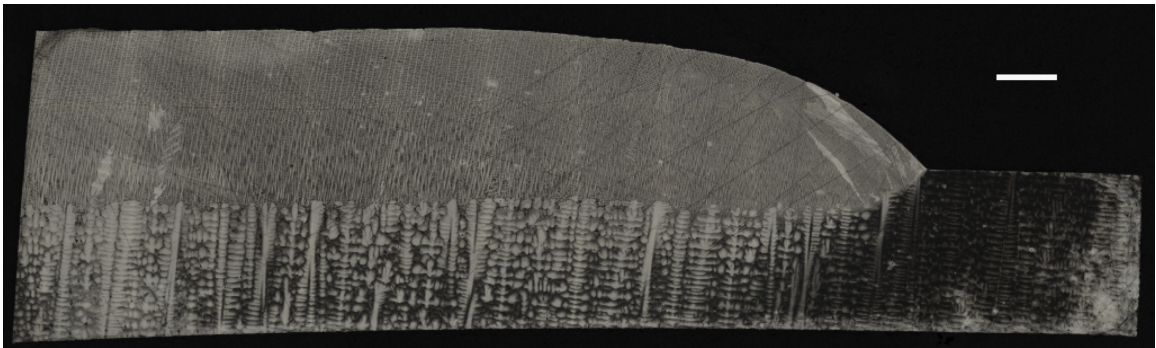
Figure 74: Image demonstrating the bending in the later half sample CMSX4 which was run at high energy density. Scale bar is 1mm.

Many of the samples exhibit the phenomena described in this section, but proper selection of processing parameters minimizes the impact of each of these problems. Trial CMSX14 shown in Figure 75 illustrates the result of properly balanced parameters.
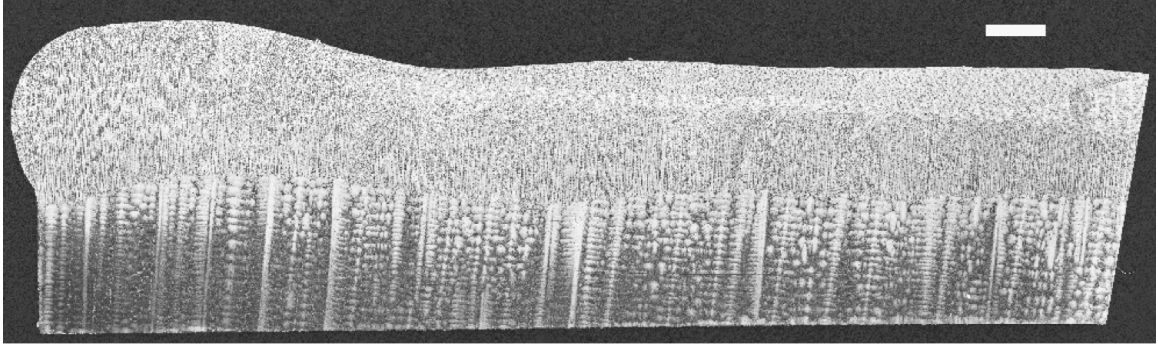
Figure 75: Sample CMSX14 demonstrates a sample produced at a proper balance of repeat scans, scan speed, and laser power. Notable features are fusion across the length of the sample, significant columnar growth, and lack of pores or cracking. Scale bar is 1mm.

In this sample there is full fusion along the entire sample, melt-back depth within tolerance, and significant columnar growth along the length of the sample. This sample demonstrates more than 1mm of columnar structure across nearly the entire length. Also of note is the lack of porosity in the samples, indicating the cleanliness of the powder and lack of contaminants in the processing chamber.

Another interesting phenomena is the dendrite width of deposited material being nearly 15 times finer than the dendrite width of the underlying substrate, as illustrated in Figure 76
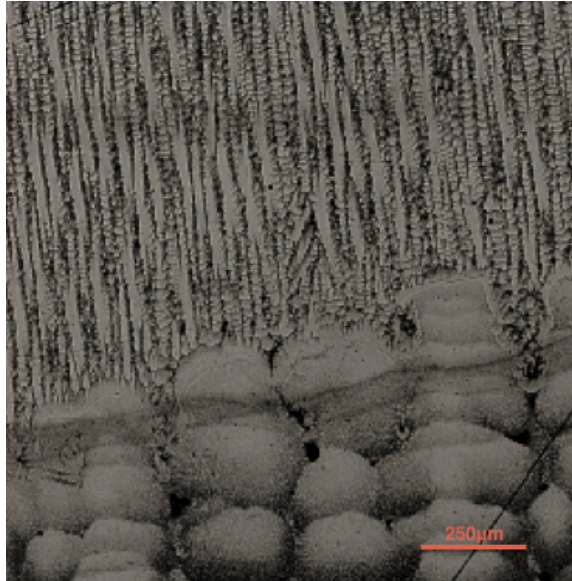
Figure 76: Illustration of the transition from wider dendrites to finer dendrites at the interface between cast material and SLE deposited material.

The finer dendrite width is caused by the significantly higher cooling rates experienced during solidification in the SLE process as compared to the casting process used to create the substrate [64].

4.4.3   Process Maps

The CMSX-4 samples were etched and then processed using the optical metallographic software analysis described in the third chapter. It was of particular interest to see how volumetric energy density related to the percentage of the sample that was fused, the overall average deposit height, the average columnar height, the average melt-back depth, the amount of deformation, and the number of stray grains present in the deposit. Figure 77 shows the percentage of the overall deposit that was fused to the underlying substrate.
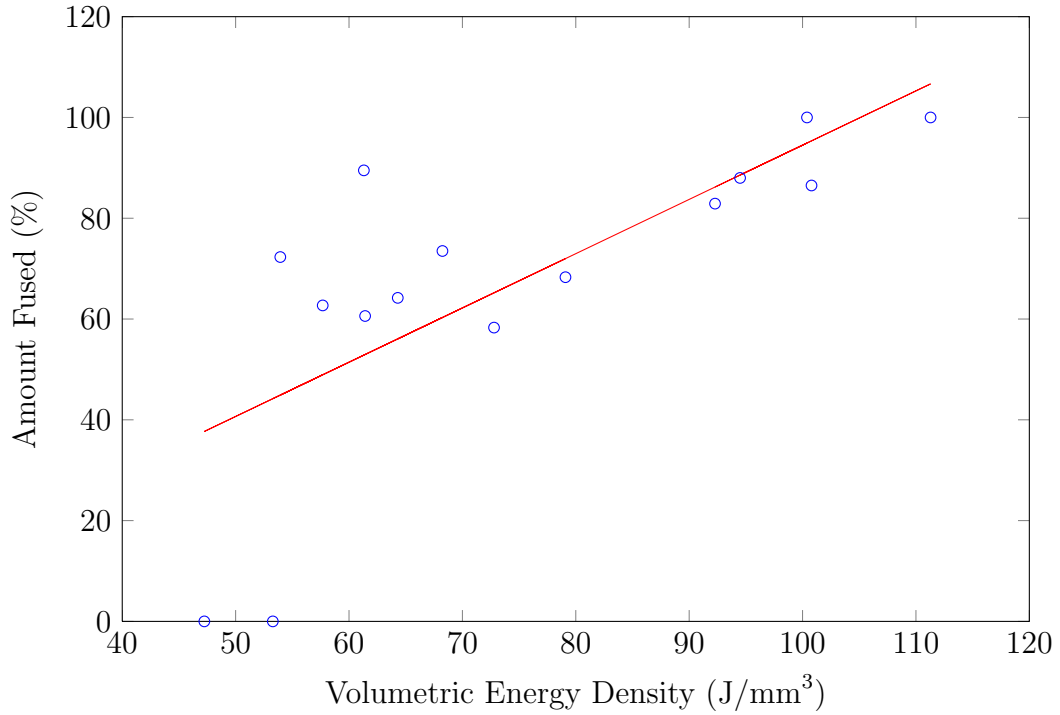
Figure 77: Percentage of substrate fused as a function of volumetric energy density. Fit line indicating the upward trend plotted in red.

As expected, it can be seen that the percentage fused increases with the volumetric energy density due to more energy being provided to melt the underlying substrate at higher volumetric energy density. It can also be seen that the trials involving 2mm powder height had a significant lack of fusion as compared to the 1mm and 1.5mm trials. This severe lack of fusion rendered several of the 2mm powder thickness samples from being able to be analyzed via the software algorithm. The metrics for these 2mm samples were instead measured manually by taking several points across the lengthwise cut and determining an average value for each metric using measurements at each of these points.

Figure 78 illustrates the change in deposit height as a function of volumetric energy density.
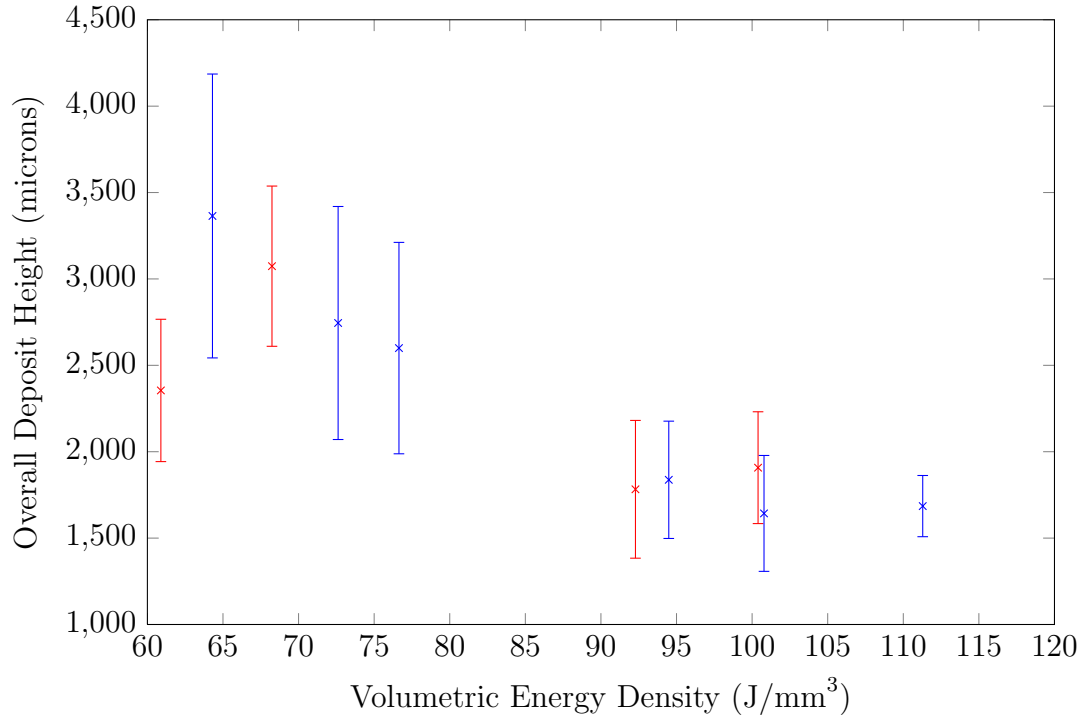
Figure 78: Average deposit height vs volumetric energy density for CMSX-4 trials. Error bars indicate the standard deviation of the deposit height across the substrate length. Red markers indicate samples run at 50 repeats and Blue markers indicate samples run at 100 repeats.

The set of five samples clustered at lower volumetric energy density have a higher average deposit height than the second cluster of five samples due to being run with the larger powder thickness of 1.5mm. Within each cluster of samples though, a downward trend in deposit thickness can still be seen with an increase in the energy density. This is due to a larger portion of the underlying substrate being melted at higher energy densities. Also of note is the fact that the overall deposit height is seemingly higher than the amount of powder placed on top of the sample. This is due to the additional powder around the samples that is sucked into the melt pool as well as the cresting towards the middle of the sample, illustrated earlier in Figure 65, where the cross-sectional widthwise cut is taken.

Figure 79 shows two deposit heights for samples run with different powder thicknesses but similar other parameters.
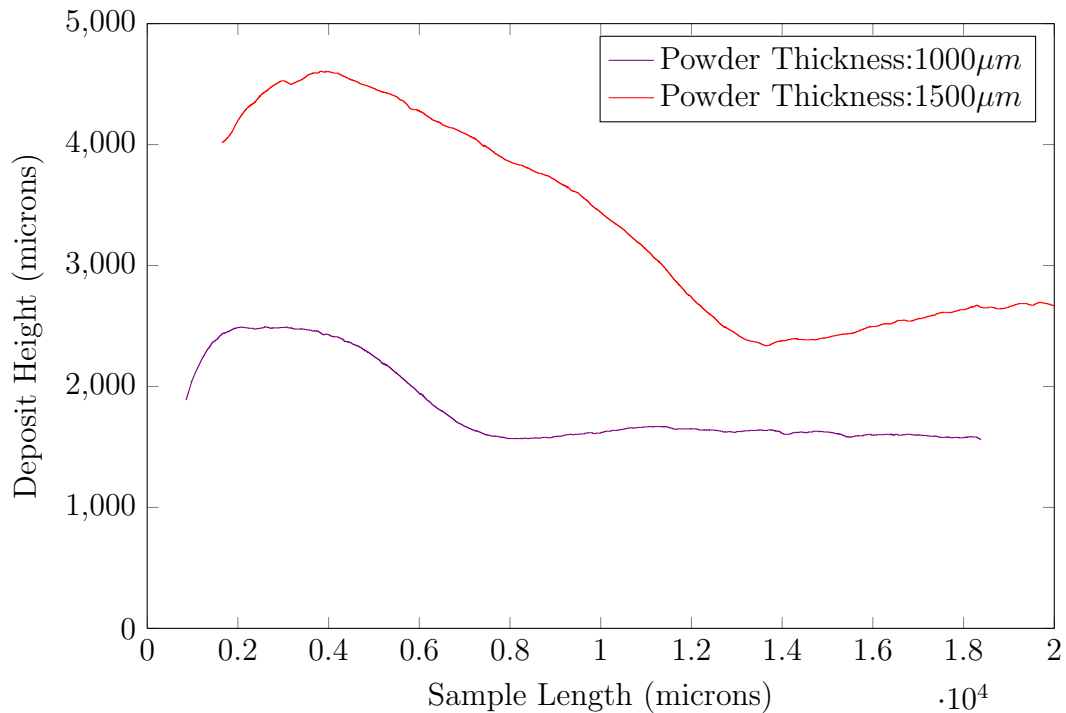
Figure 79: Comparison of total deposit height in samples CMSX8 and CMSX13 both run at $200mm/sec$ scan speed and approximately 485W power with 100 repeats but having differing powder heights.

The high correlation between powder height and deposit height becomes readily apparent when viewing plots such as these.

Figure 80 illustrates the change in deposit height as a function of volumetric energy density.
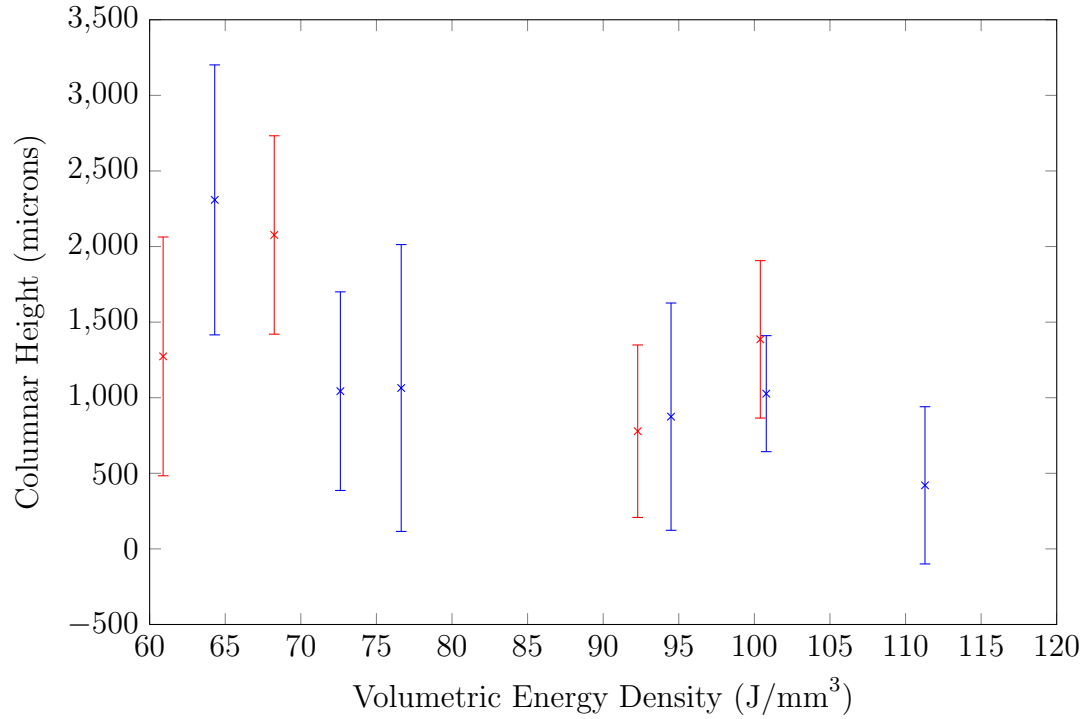
Figure 80: Average columnar height vs volumetric energy density for CMSX-4 trials. Error bars indicate the standard deviation of the columnar height across the substrate length. Red markers indicate samples run at 50 repeats and blue markers indicate samples run at 100 repeats.

The columnar height produced exhibits a slight downward trend with increasing volumetric energy density and is also heavily correlated with powder thickness as illustrated in Figure 81.
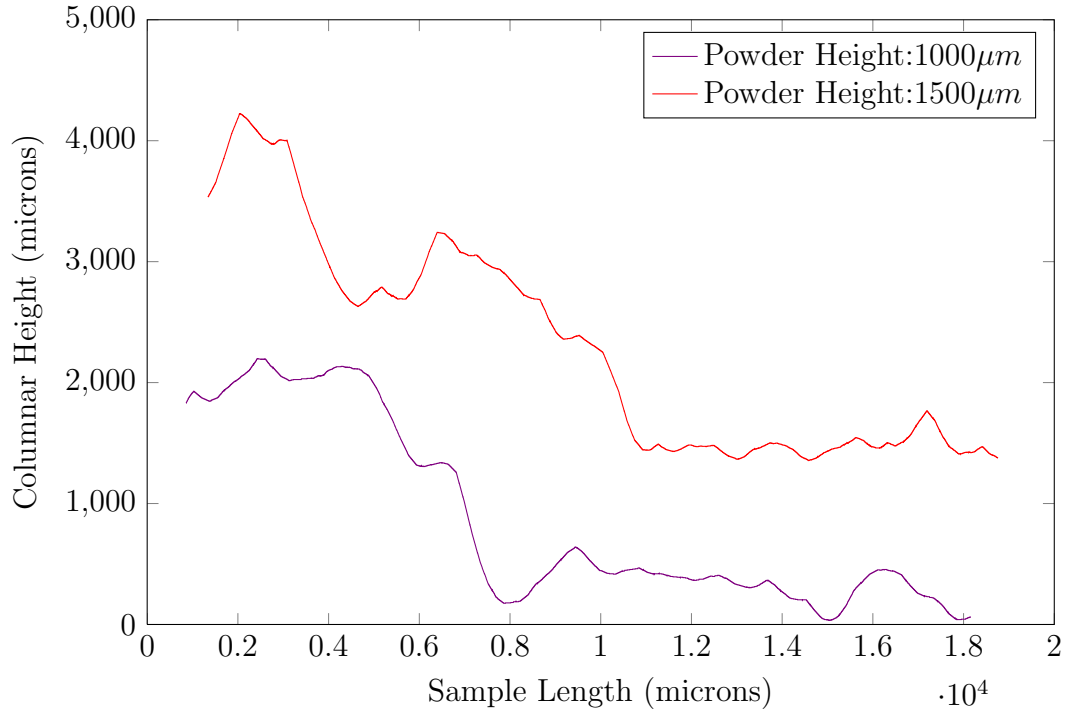
Figure 81: Comparison of columnar height in samples CMSX8 and CMSX13 both run at $200mm/sec$ scan speed and approximately 485W power with 100 repeats but having differing powder heights.

The columnar height is adversely affected by the formation of equiaxed and misoriented grains near the top of the deposit. It is likely the case that more advanced power profiles or feedback control as discussed in Chapter 5 will be required to increase the columnar height towards the trailing edge of the samples and thus increase the overall average columnar height.

Figure 82 illustrates the change in melt-back depth as a function of volumetric energy density.
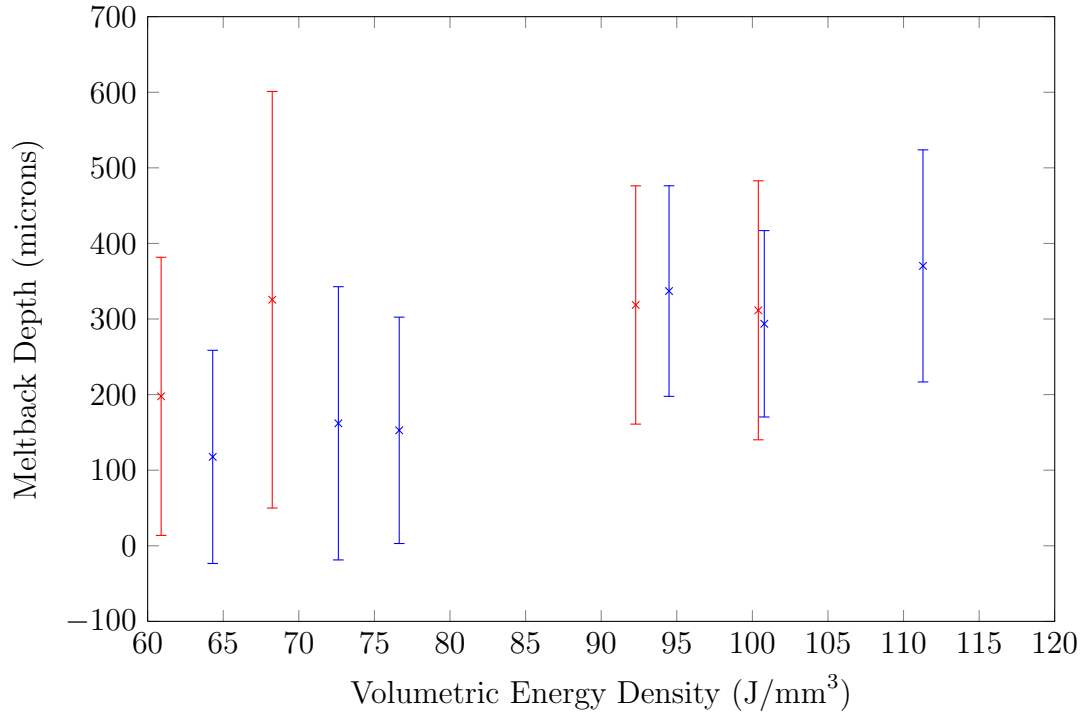
Figure 82: Average melt-back depth vs volumetric energy density for CMSX-4 trials. Error bars indicate the standard deviation of the melt back depth across the substrate length. Red markers indicate samples run at 50 repeats and blue markers indicate samples run at 100 repeats.

Most of the samples exhibit melt-back depths within the tolerable range of 500 microns, but several samples have a high amount of melt-back at the starting edge where repeat scans are used to initiate the melt pool. The repeat scans affect the amount of melt-back depth significantly at the start of the sample but their effect diminishes as the scan proceeds along the sample. Lack of repeat scans cause a lack of bonding at the starting edge though, so repeat scans must be balanced between initiating the melt pool but not over melting the substrate. Additional strategies for initiating the melt pool such as linearly ramping the power during repeat scans may help to eliminate the issues of overmelting and balling at the starting edge.

Figure 83 illustrates the change in the number of stray grains measured manually

as a function of volumetric energy density.
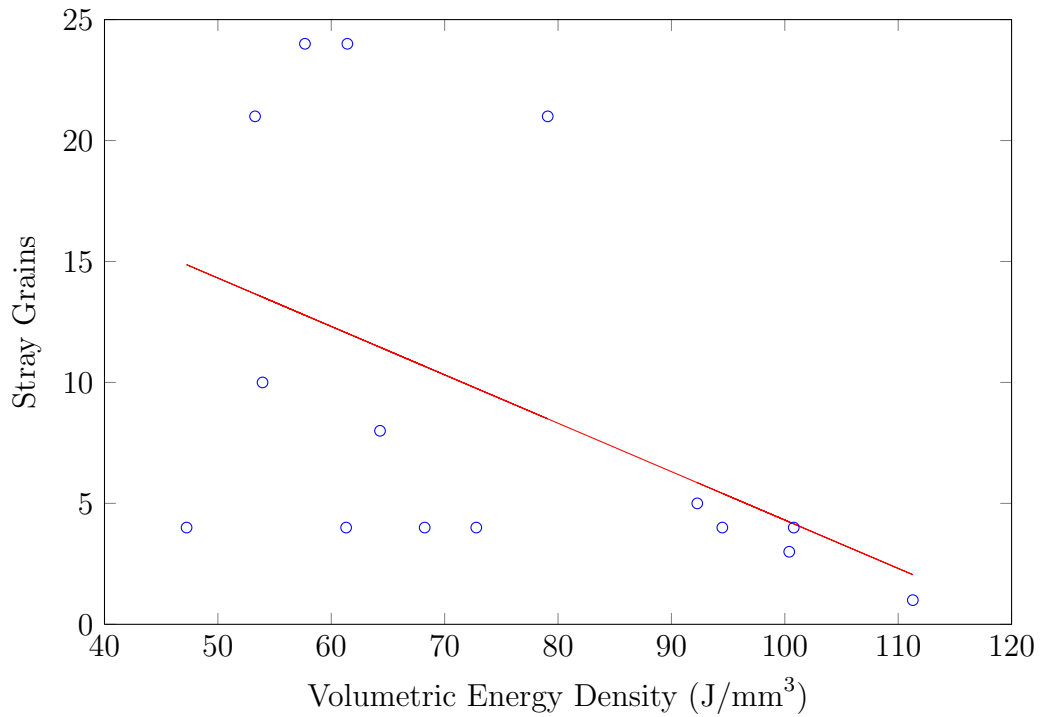
Figure 83: Number of stray grains as a function of volumetric energy density.

It can be seen that the number of stray grains decreases significantly as the volumetric energy density increases. This can also be analyzed by looking at a fit model correlating the number of stray grains with the energy density and powder thickness, as illustrated in Figure 84 with the fit significance shown in Figure 133(b) in Appendix B.
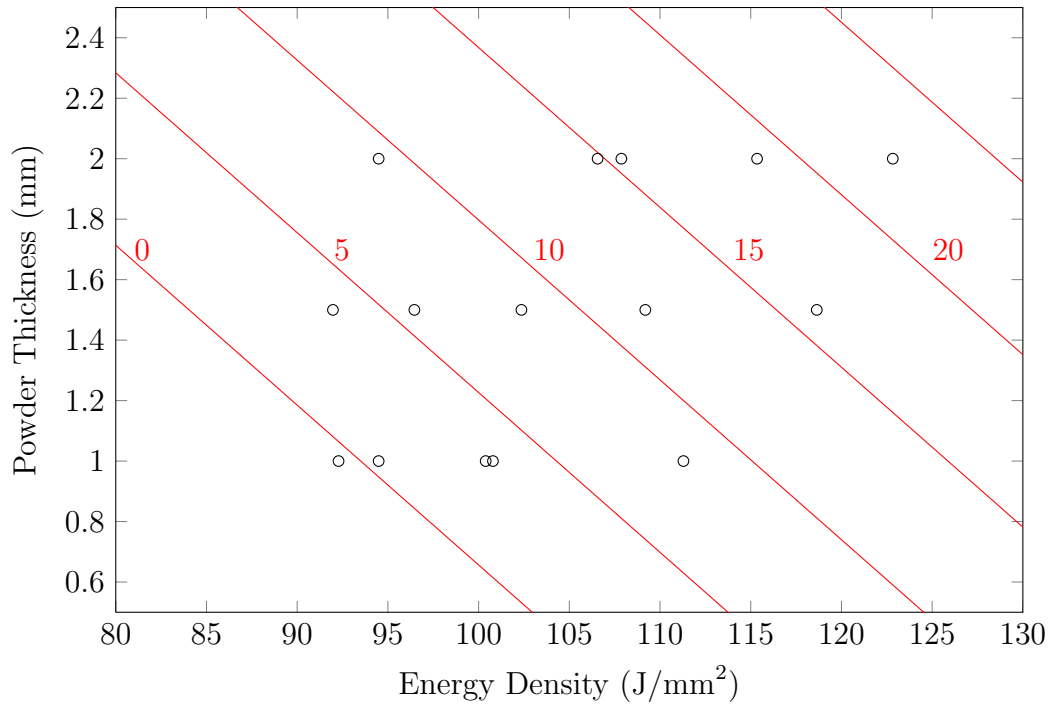
Figure 84: Contour profile of modeled stray grain formation vs energy density and powder thickness. Sample data points are indicated by the black circles.

Both energy density and powder thickness factor into the calculation of volumetric energy density. It is important to note that stray grain formation is minimized by lowering both powder thickness and energy density. There is a trade off though between supplying enough energy to remelt the substrate while also limiting the number of stray grains that are formed. When the processing parameters are properly chosen, a deposit with a significant amount of columnar structure and minimal melt-back can be achieved, as was the case in sample CMSX14 illustrated in Figure 85.
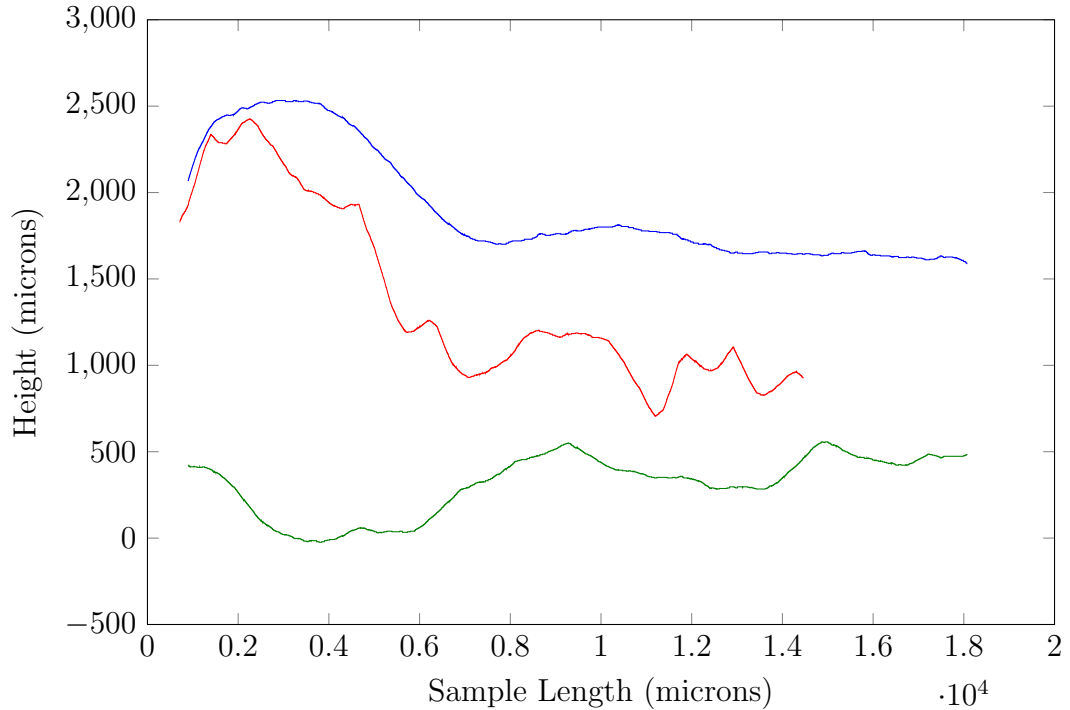
Figure 85: Plot of total deposit height (blue), columnar height (red), and melt depth (green) for sample CMSX14 demonstrating significant columnar growth and minimal melt back depth for properly chosen operating parameters.

This sample demonstrated full fusion with minimal melt back of below 500 microns, as well as significant columnar growth of approximately 1000 microns. Additionally, the average columnar to total height ratio (CTR) was greater than 50% across the length.

To develop a process map for CMSX-4 using the metrics measured in this section, the JMP 10 software package was used to develop fit models relating the powder height and energy density to several of the resulting metrics including the total percent fused, CTR, and number of stray grains. The statistical results and prediction formulas for each of these fit models are shown in Figures 133(a), 133(b), and 133(c) in Appendix B.

Using the results of these fit models, the process map for CMSX-4 illustrated in

Figure 86 was generated using the prediction formulas for each fit.
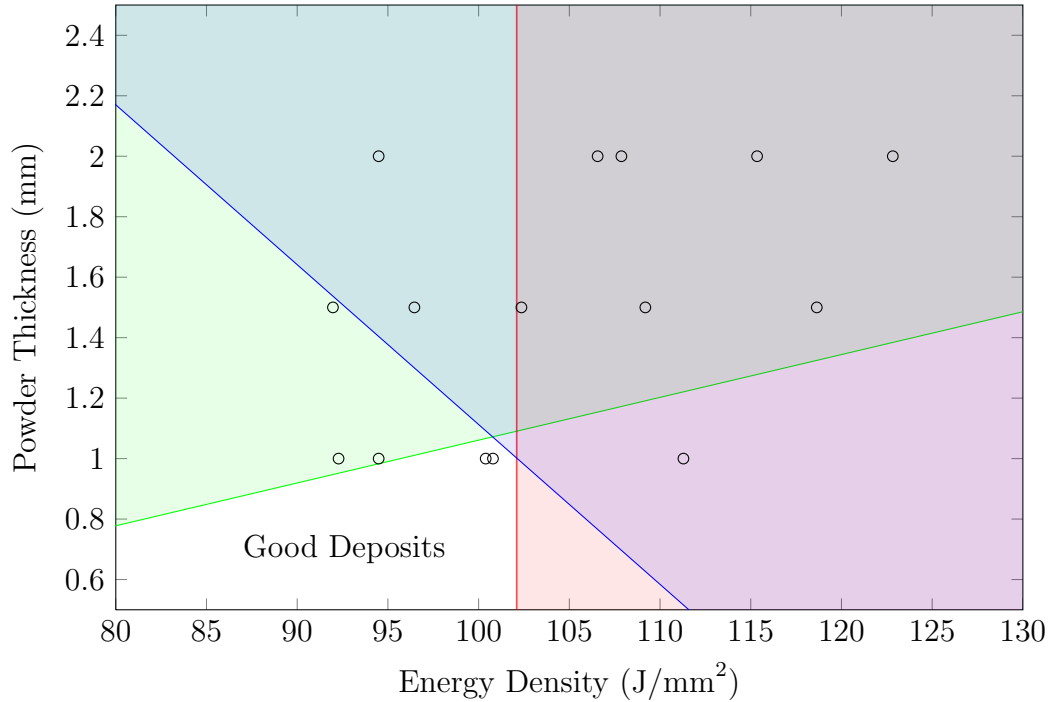
Figure 86: Process map for creating high quality CMSX-4 samples. The dots indicate the samples that were run. The green shaded area indicates where less than 90% of the sample would be fused. The red shaded area indicates lower than 50% CTR area. The blue shaded region indicates more than 4 stray grains. The white region indicates the area where high quality CMSX-4 deposits are formed.

The melt-back depth tolerance of 500 microns did not have a significant impact on the location at which good deposits were formed due to melt-back being within tolerances for nearly all samples run. The best processed samples, CMSX12 and CMSX14 sit close to the apex of the high quality deposit area, indicating that future trials at lower powder thickness are necessary to determine the lower bounds. These trials will likely take place once the multi-layer powder deposition system is put into place.

In summary, lower powder thickness with higher energy density resulting in a volumetric energy densities on the order of $100 J/mm^3$ led to the most promising

samples. Low energy density led to a lack of fusion along the length of the sample. High energy density led to stray grain formation and lower overall columnar to total deposit height ratio. It must also must be noted that increasing the energy density too much can lead to over melting of the base substrate and substrate warping as seen in some micrograph images. It is likely the case that more advanced power profiles or feedback control as discussed in the Chapter 5 will be required to increase the columnar height towards the trailing edge of the samples and reduce stray grain count. These strategies could also limit warping and overmelting towards the trailing edge of the scans by decreasing the incident laser power as scanning proceeds.

4.5   René-80 Process Parameter Development

After demonstrating the capability of the SLE process to create single-crystal microstructures on an SX material like CMSX-4, the next goal was to demonstrate its capabilities of creating fully-dense crack-free deposits on a more highly crack prone material such as René-80. Building upon the several years of development involved in improving the repeatability of the single-crystal experiments, an identical powder containment system was used to meter and hold powder on top of the substrate for processing in the René-80 trials. A similarly configured Inconel 625 baseplate with hollow cutouts below each sample was also used to again simulate the thermal conditions present on an actual turbine blade tip. Additionally, a new IPG Photonics YLS-1000 fiber laser was acquired and implemented as described in Chapter 3 that significantly improved the reliability and repeatability of the process due to having a much higher beam quality, power stability, and much smaller beam spot size than the older lamp pumped laser.

Due to being the first material run with the highly focused laser, many preliminary experiments were conducted with parameters varied by observation to develop a feasible operating range in which samples exhibited some bonding across the sample

length while also not melting all of the way through the substrate. The power stability of the new laser also enabled the use of a proper set of design of experiments (DoE) to be run when developing parameters for René-80. As such, after this initial development of a feasible range, several DoEs were conducted to drill down on an optimal set of parameters for producing high quality René-80 deposits. The parameter range explored included 100-400 repeat scans, scan speeds of 450-650mm/sec, laser powers of 350-600 W. All samples were run with a lower fixed scan spacing of $12.7 \mu m$ to account for the smaller beam diameter on the fiber laser and each substrate coupon had dimensions of 35.6 x 6.9 x 2.54mm. Additionally, all trials were run at a fixed powder height of 1.4mm. The DoEs conducted were phase one ascent DoEs based on a fractional factorial design meant to quickly identify the proper parameter range and identify the main factor effects on the chosen quality metrics of melt depth, melt uniformity, deposit height, and deposit uniformity. The sets of DoEs that were conducted are listed in Table 9.

Table 9: Samples used for René-80 process map development.

Sample Number	Laser Power (W)	Scan Speed (mm/s)	Repeats	Energy Density (J/mm^2)	Average Melt Depth (microns)	Average Deposit Height (microns)	Deposit Height R^2
RENE1	350	450	350	61.24	127.81	1548.8	0.35
RENE2	350	450	400	61.24	212.28	1738.9	0.21
RENE3	350	450	450	61.24	67.901	1818.7	0.09
RENE4	350	500	400	55.12	41.745	1553.4	0.49
RENE5	350	550	450	50.11	14.953	1521.5	0.16
RENE6	400	450	400	69.99	131.31	1672.3	0.04
RENE7	400	500	450	62.99	54.372	1841.2	0.26
RENE8	400	550	350	57.27	18.341	1778.3	0.39
RENE9	450	450	450	78.74	356.41	1731.1	0.52
RENE10	450	500	350	70.87	61.934	1942.7	0.40
RENE11	450	550	400	64.42	2.7238	1548.2	0.15
RENE12	350	450	350	61.24	-15.57	1739.9	0.35
RENE13	550	500	300	86.61	275.23	1959.1	0.17
RENE14	500	500	100	78.74	462.61	1886.3	0.63
RENE15	600	500	200	94.49	324.91	2558.3	0.29
RENE16	600	600	100	78.74	282.42	1838.8	0.26
RENE17	500	550	100	71.58	150.95	1713.5	0.43
RENE18	600	550	300	85.90	292.1	1962.9	0.60
RENE19	550	600	200	72.18	171.86	1945.8	0.53
RENE20	500	600	300	65.62	77.417	1985.4	0.35
RENE21	500	550	200	71.58	62.686	1937.2	0.40
RENE22	550	550	100	78.74	638.73	2230	0.65

Each of the René-80 samples produced were cut in half lengthwise and had one half immediately polished for metallographic analysis. The other half was processed via heat treatment at over $1000°C$ in an argon purged tube furnace for approximately two hours including heating and cooling time before metallographic analysis. The heat treated sections were meant to determine whether the samples were prone to strain-age cracking.

4.5.1 Image Analysis

Figure 87(a) shows a high quality René-80 deposit produced and illustrates the deposit uniformity across the sample. Figure 87(b) shows a sample run at poorly chosen parameters, resulting in a highly non-uniform deposit.
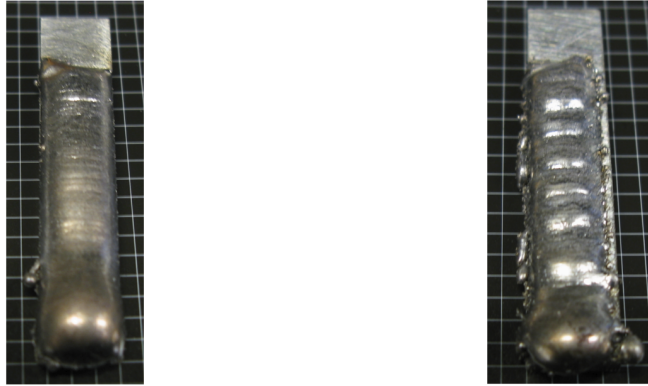
(a) Image of a high quality René-80 deposit on 2mm grid paper.

(b) Image of a low quality René-80 deposit on 2mm grid paper.

Figure 87: Images of as-processed René-80 samples.

Analysis of the processed René-80 samples showed no indication of cracking in either the non-heat treated or heat treated samples. Figures 88(a) and 88(b) show two examples of René-80 samples produced.

(a) Non-heat treated René-80 deposit.
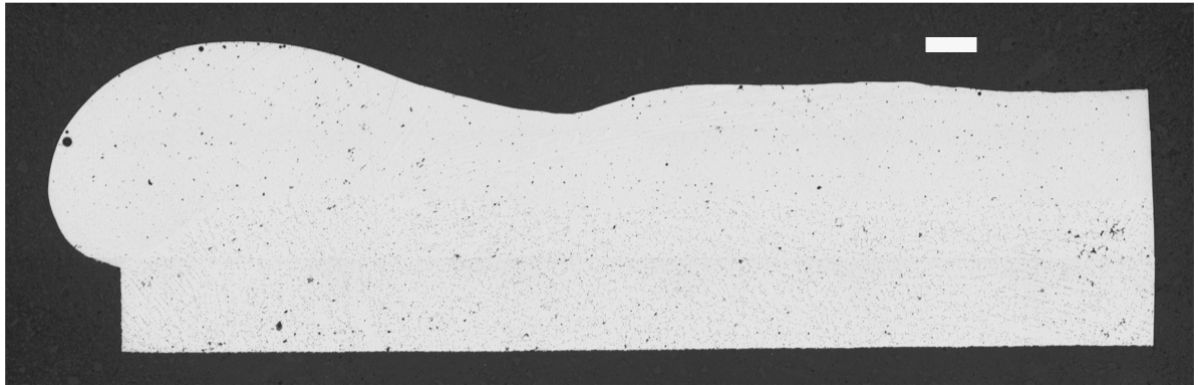
(b) Heat treated René-80 deposit.

Figure 88: Comparison of opposite halves of a non-heat treated and heat treated René-80 samples showing no indication of cracking.

Figures 89 and 90 demonstrate that deposits produced via SLE were actually less prone to cracking than that of the cast substrate itself.
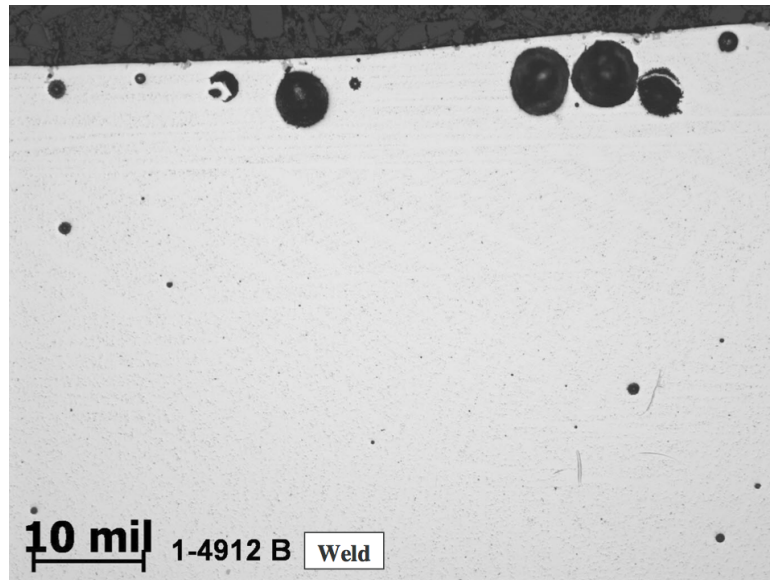
Figure 89: Micrograph of René-80 demonstrating no cracking in the deposited material.
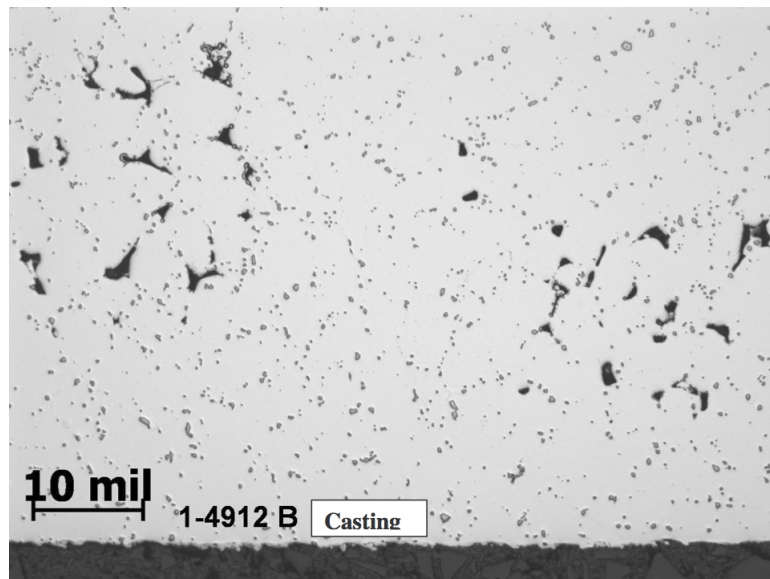
Figure 90: Micrograph of as cast René-80 substrate showing indications of cracking.

Although there was no indication of cracking in the deposited material, several of the René-80 samples did have evidence of significant spherical porosity, especially at the top of the sample, as illustrated in Figure 89. DoE analysis showed no correlation

between porosity occurrence and processing parameters such as scan speed, laser power, or repeat scans, lending to the conclusion that the porosity was caused by another external factor. It is likely that this porosity at the top surface was due to contamination in the René-80 powder during the bake-out process used for these trials. This porosity began appearing in samples after it was found that oil vapor from the powder bake-out vacuum oven pump had begun back flowing into the oven and contaminating it. Even with contamination, the small amount of porosity appearing near the top of the sample would typically be ground off during the normal contour grinding done before placing a repaired turbine engine component into an engine in the repair scenario. In the multilayer buildup scenario, the porosity would be remelted during the processing of the subsequent layer. As such, it does not significantly detract from the capability of the SLE process to produce high quality deposits even with contaminated powder and demonstrates that contaminants will bubble to the top of the melt pool during processing.

Figure 91 demonstrates the finer structure of the deposited material as compared to the cast material.
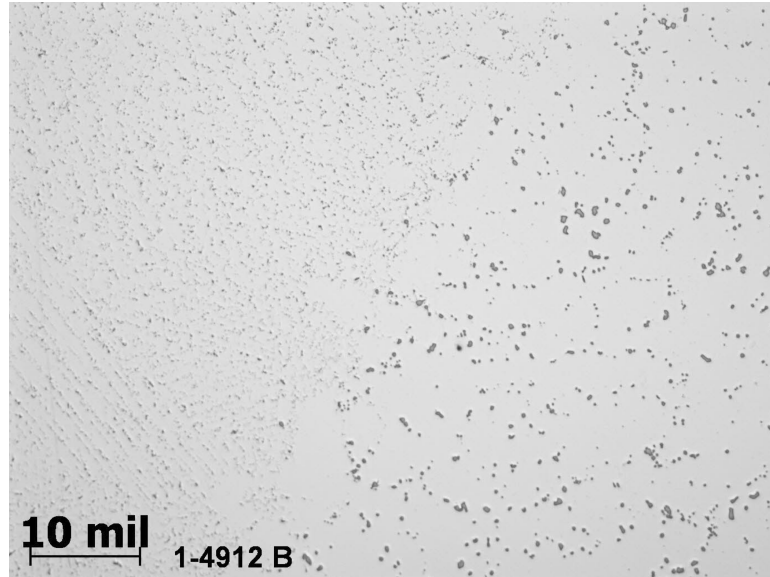
Figure 91: Micrograph of processed René-80 substrate showing the interface between deposited material on the left and substrate on the right.

The grey speckled pattern on the material is the distribution of the MC carbide precipitate and is several times finer in the deposited material due to the high solidification rate as compared to the cast substrate.

Of particular interest in this study was determining a set of parameters that would produce deposits with uniform melt back depth and deposit height. Figure 92 illustrates a sample processed with an optimal set of processing parameters.

Figure 92: Micrograph of sample RENE14 demonstrating a highly uniform deposit height with sufficient but not excess melt back. Scale bar is 1mm.

109

Figure 93 illustrates a sample run at poor parameters, resulting in a highly non-uniform deposit.
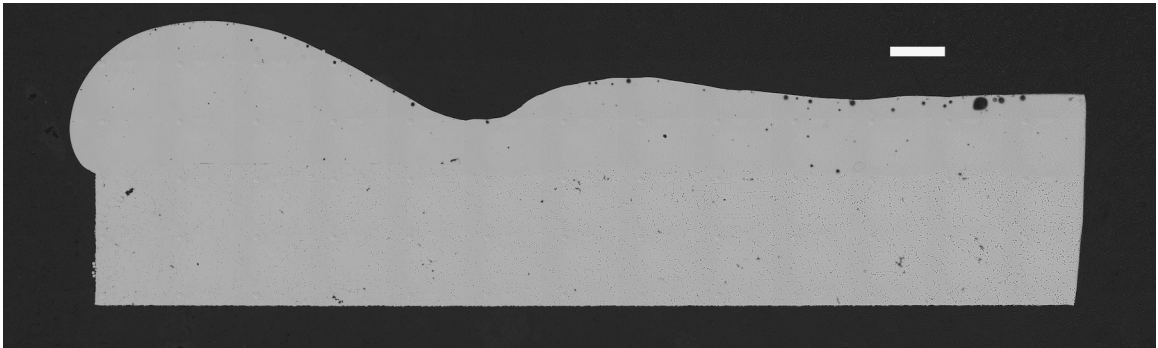
Figure 93: Micrograph of sample RENE4 demonstrating a non-uniform deposit height and low melt-back. Scale bar is 1mm.

In samples such as these ones, the combination of scan speed and power results in high surface tension and instability at the front of the melt pool, adversely affecting smooth flow of molten powder into the melt pool front. The scan proceeds so quickly that a large amount of powder will fall into the melt pool, causing a shortage of powder slightly later in the scan, resulting in the humps seen in the non-uniformity of the deposit.

One sample, run at the highest energy density of all samples, illustrated in Figure 94, was completely melted through.

Figure 94: Micrograph of sample RENE15 demonstrating extreme substrate melting at high energy density with a high number of repeat scans. Scale bar is 1mm.

Due to the significant destruction of this sample, it was neglected from the DoE analysis. It must be noted though that using energy densities as high as this with a significant number of repeat scans will result in complete substrate melting. Again, as with the CMSX-4 trials, it is necessary to carefully choose the set of processing parameters used to develop high quality deposits.

4.5.2 Process Maps

The set of metrics used to develop process maps for the René-80 samples included the average deposit height, average melt back depth, and deposit uniformity. The deposit uniformity was calculated by taking the deposit height of the sample, developing a linear fit for the height and then calculating the average R^2 residual between the height and the linear fit. The higher the R^2 value, the more uniform the deposit. Figure 95 illustrates the calculation of the deposit height uniformity metric.
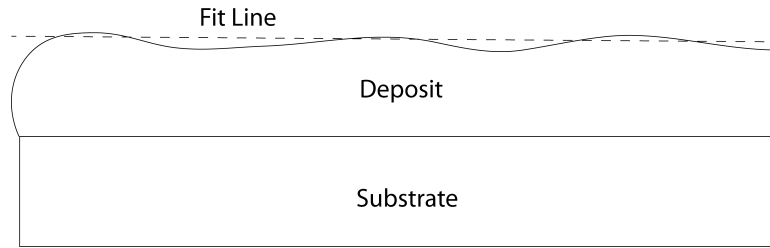
Figure 95: Illustration of the linear fit used to determine deposit height uniformity.

The measured metrics, listed in Table 9, were used to develop a set of process maps for the René-80 DoE trials using the JMP software package. It was found that samples exhibiting below 100 micron average melt back depth all had a lack of fusion at at least one point along the sample. For this reason, 100 micron average melt depth was chosen as the lower limit for melt back depth in the process maps developed. Figures 134(a) through 135(c) in Appendix B show the statistical analysis of the fits. The prediction expressions for each fit model are also listed in the Appendix.

Figure 96 shows an overview of the effects of the processing parameters on each metric.
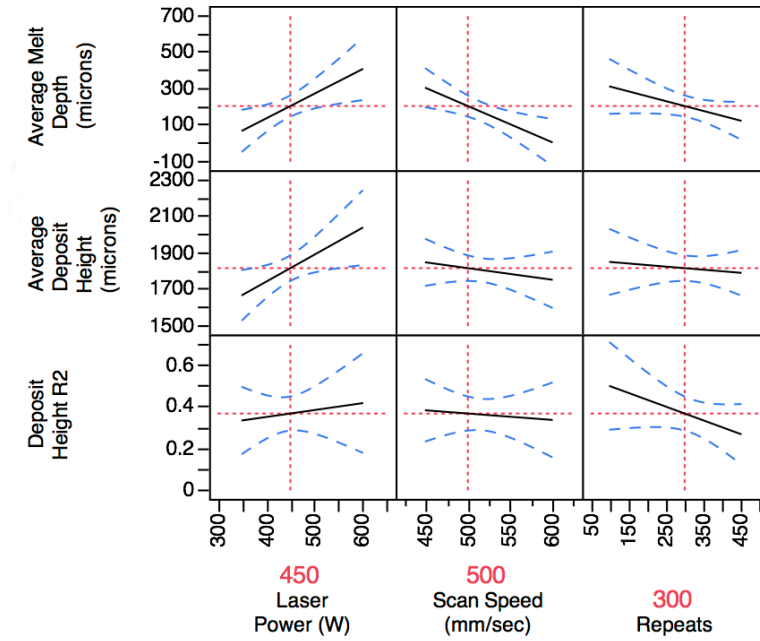
Figure 96: Overview of the effects of each process parameter on the various quality metrics.

It can be seen from the profiler that laser power most significantly impacts the deposit height and melt depth and tends to significantly increase each of these values as it increases. Scan speed most significantly impacts the melt depth and causes it to decrease as the scan speed increases. The number of repeat scans have a significant impact on the deposit uniformity and melt depth, increasing both as the repeat scans increase.

Figure 97 illustrates the effect of repeat and scan speed on the resulting deposit quality.
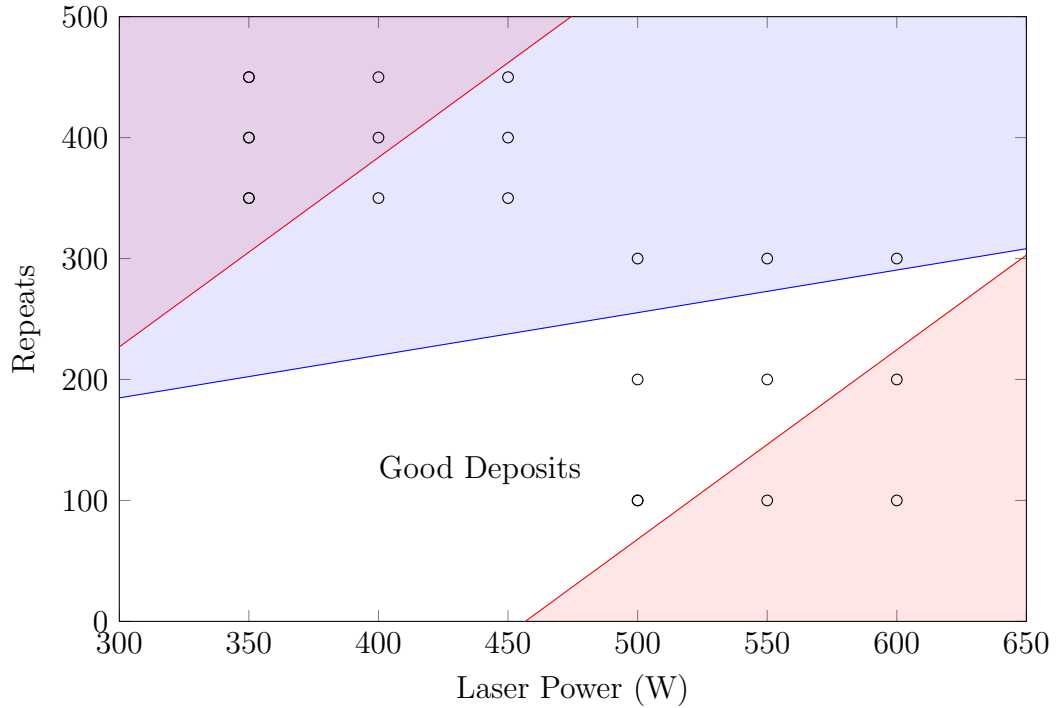
Figure 97: Process map relating repeat scans and laser power to high quality deposit formation. The lower limit of 100 micron average melt back depth is shaded in red on the left side and upper limit of 300 micron average melt back depth is shaded on the right. The blue shaded region indicates deposit uniformity below 0.40. The black dots indicate the data points.

The white area is the area in which highly uniform deposits with a proper amount of melt-back and high uniformity are produced. As can be seen, reducing the number of repeat scans and laser power leads to more uniform deposits. It is known though, as was the case with the CMSX-4 trials, that reducing laser power and repeat scans too much results in balling and lack of fusion at the starting edge of the sample. For reference, the highest quality sample produced in these trials had a deposit uniformity R^2 value of 0.65 and the lowest quality samples had uniformities on the order of 0.20.

Figure 98 illustrates that increasing scan speed while simultaneously increasing laser power will result in more uniform deposits within the tolerable melt back range.
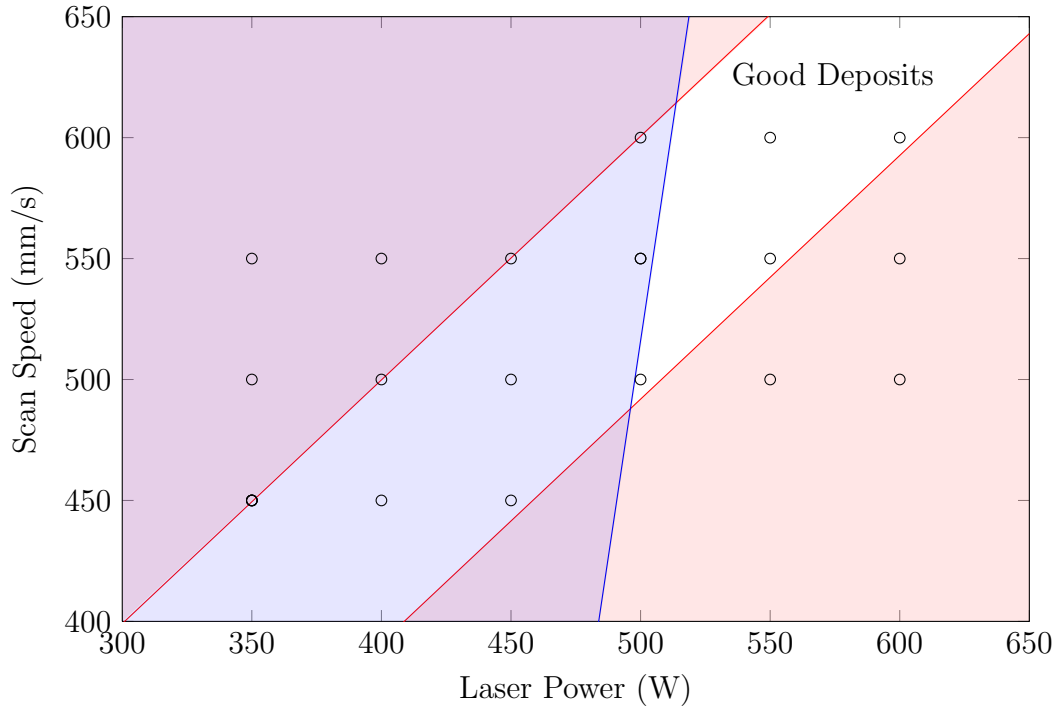
Figure 98: Process map relating scan speed and laser power to high quality deposit formation. The lower limit of 100 micron average melt back depth is shaded in red on the left side and upper limit of 400 micron average melt back depth is shaded on the right. The blue shaded region indicates deposit uniformity below 0.40.

It can be seen that increasing scan speed and laser power simultaneously leads to the highest quality deposits. It is likely that very high scan speeds in conjunction with high laser power will lead to substrate warping due to thermal stresses in the substrate. This phenomena would likely set an upper bound on the indicated white region, towards the top right portion of the process map. These conditions were not tested though due to limitations that were found in the coatings on the mirrors in the galvanometer scanner used in this research. The mirror coatings on the scanner system became damaged when operating at laser powers above 600W for a full scan.

In summary, it was found that the SLE process was capable of producing high uniformity, low melt-back deposits of René-80 material without any indications of

cracking. Heat treatment of samples also produced no evidence of strain-age cracking in deposited material. The lack of cracking seen in the SLE process is due to the high amount of pre-heat and post-heat applied to each portion of the sample due to beam overlapping caused by scanning with an extremely short scan spacing.

4.6 Summary

This chapter presented the development of the SLE process over the past several years and included developments in both the experimental setup and process parameter selection. The process was initially proven on the Mar-M247 material, on which several highly uniform deposits with full fusion at the bond line were produced. The Mar-M247 samples did not show any indication of cracking even after heat treatment in an argon tube furnace. These samples did indicate several improvements that the SLE process would require going forward. Firstly, a powder containment setup would be required to produce deposits with a uniform height across the width. Secondly, a laser with high stability power or in-line power measurement would be required to produce proper experimental results. These two issues were resolved before continuing with the single-crystal trials on CMSX-4. The CMSX-4 trials showed that the SLE process was capable of producing significant single-crystal growth in deposited material both along the length and from edge to edge along the width of the samples. A process map was also developed for CMSX-4 indicating the parameter ranges in which high quality samples would be produced for varied powder thicknesses. The chapter concluded with a study of the SLE process applied to the highly crack prone René-80 material. Again, as with the Mar-M247 trials, the René-80 samples showed no evidence of cracking, even after heat treatment. Additionally, the René-80 samples were run on a newer high quality IPG Photonics 1kW fiber laser, allowing for proper DoE analysis of the results. Using a set of two DoEs, process maps were developed for the René-80 material showing the processing parameters that would lead to high

quality samples with minimal melt back and maximum deposit uniformity across the length.

CHAPTER V

FEEDBACK CONTROL OF THE SLE PROCESS

The addition of real-time feedback control to the area of additive manufacturing has been targeted in road maps for additive manufacturing as an area of high interest due to the relative lack of research done in the area in the past and the potential impact that proper control could have on the quality of parts that are able to be manufactured via additive processes [42]. This chapter describes the development of a real-time feedback control system to control the SLE process and enable higher repeatability, greater uniformity, and functionally graded microstructures. The chapter begins by laying out why feedback control was explored, covers the development of sensors to use in feedback control schemes, discusses the development of a thermal model and subsequent system identification, gives details about the types of control schemes used, and concludes with an analysis of the results of the controls trials.

As described in Chapter 2 and demonstrated in Chapter 4, it is possible to develop process maps for creating high quality deposits using open loop control for SLE or other related technologies. One of the concerns when developing these process maps is that it is an expensive and time consuming process, especially when using exotic materials such as those used to produce high temperature turbine components. Additionally, current additive manufacturing processes are unable to account for disturbances or anomalies during processing, potentially leading to issues with repeatability. When producing multilayer parts composed of hundreds or thousands of layers, it is critical to make sure that there are no inclusions or problematic spots in any layer. Any defects in the part will deem it unusable for high performance applications such as usage in the hot section of a turbine engine. It is hypothesized

that real-time feedback control of the SLE process will increase the repeatability of the process and allow tighter control of microstructure than the open loop control used in all prior experimentation while also reducing the number of samples required to be processed before developing proper parameters. Real-time feedback control will address one of the key desires in further development of the SLE process, enabling it to produce multilayer components of specified functionally graded microstructure by making it robust to changes in geometry or disturbances during processing.

The end goal for the control schemes developed as part of this research is to enable the tracking of a pre-defined temperature profile generated by a complex offline model being developed for SLE by other students involved in this research, as described in the first chapter. An overview of the physics-based offline model currently being developed to model the SLE process is shown in Figure 99.
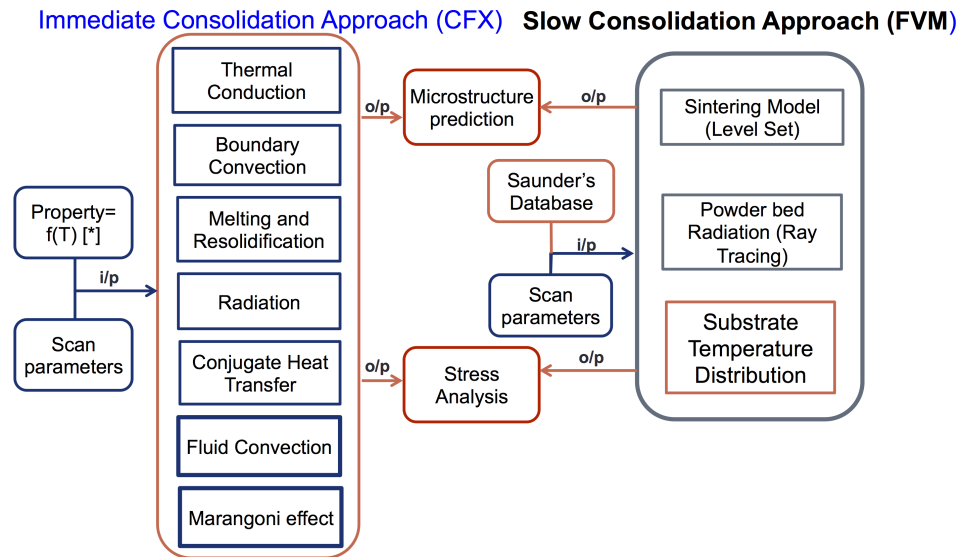
Figure 99: Overview of the end goal offline model being developed alongside this research for prediction of microstructures produced via SLE.

This comprehensive physics-based model of the SLE process is a combined computational fluid dynamics and finite volume analysis model that takes into account heat transfer, fluid flow, and solidification characteristics. The model is used to both

119

develop predictions of what microstructure is produced under certain operating parameters, and what operating parameters will be required to create particular desired microstructural characteristics. As discussed in Chapter 1 and illustrated in Figure 3, utilization of this comprehensive model in conjunction with development of a real-time control scheme to implement the parameters and temperature fields developed by this offline model will enable the production of heterogeneous multifunctional components with functionally graded microstructure via the SLE process.

A schematic overview of the components involved in the real-time control scheme for the SLE process is shown in Figure 100.
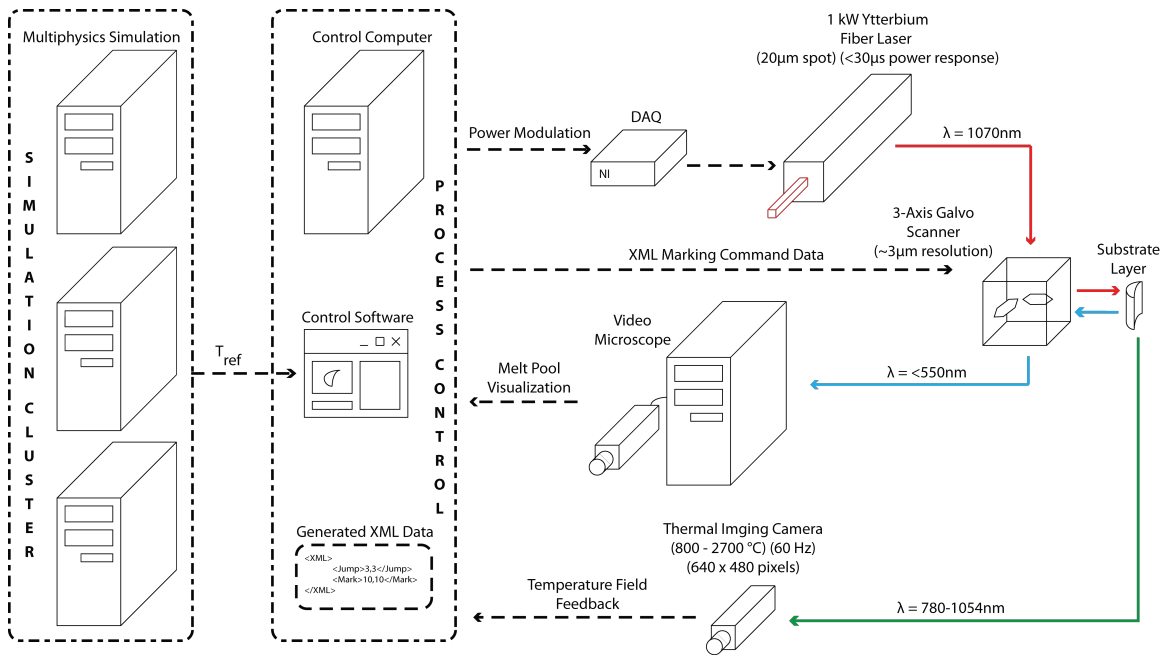
Figure 100: Schematic overview of the hardware and software involved in control of the SLE process.

The key components of the control scheme are the temperature feedback data provided by the thermal imaging camera, the laser power control provided by the DAQ board, and the process control software implemented on the control computer that ties the system together.

5.1 Sensor Development

The first step in developing a feedback control algorithm for use in the SLE process was determining a way to measure the size, shape and average temperature of the melt pool during processing. Using the data from the thermal imaging camera captured at a rate of 60 FPS as described in Chapter 3, several strategies for detecting the melt pool during SLE processing were explored. The first strategy involved the use of a Canny edge detection algorithm and the second strategy involved a scan line based method of connected component labeling. For proper detection of the melt pool it is necessary to place the thermal camera in such a way that the unmelted powder does not obscure the view of the melt pool, as illustrated in Figure 101.
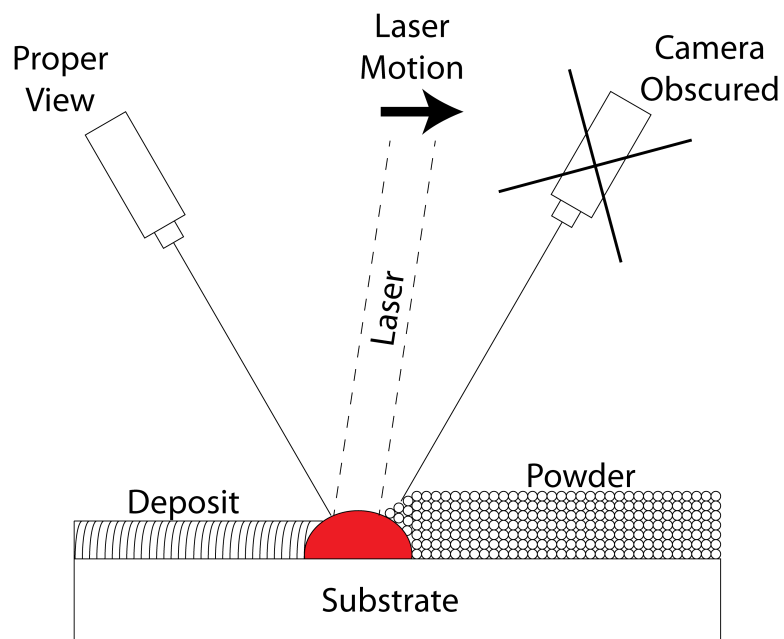
Figure 101: Illustration of the required thermal camera orientation for proper view of melt pool propagation. Molten powder balls falling into the melt pool can obscure the view from the incorrect angle.

If the camera view is obscured by the molten powder balls, an inaccurate melt pool surface temperature will be measured.

The Canny edge detection algorithm involves several steps, an overview of which is illustrated in Figure 102.

1.) Acquire thermal image.   2.) Convert to gray scale.   3.) Apply Gaussian blur.

4.) Binary threshold.   5.) Canny edge detection.   6.) Find bounding box.
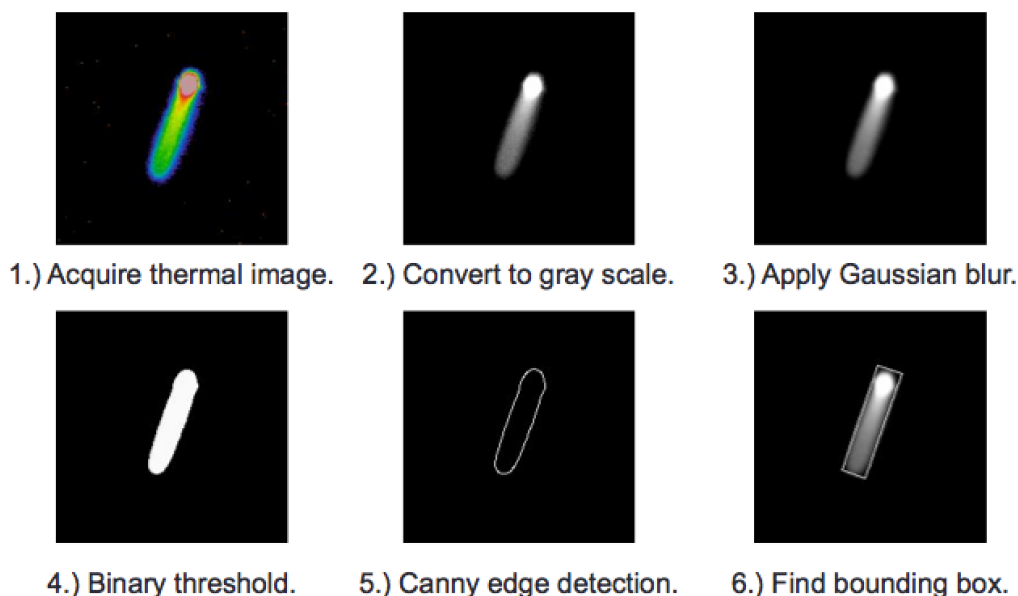
Figure 102: Overview of the Canny edge detection algorithm

The first set of operations are common between both the Canny edge detection and connected component labeling algorithms. The first step is to import the image and convert to greyscale if it is not already greyscale. A Gaussian blur is then applied to the image to filter any small specs of noise. The greyscale image is then converted to a black and white image using a binary thresholding operation. Values above the melt pool temperature (or other temperature of interest) are converted to white and values below the melt pool temperature are converted to black. This is the main operation that isolates the melt pool in the image and creates a distinct 'blob' to be detected.

The next set of steps uniquely implements the Canny algorithm. First the Sobel operator is applied to approximate the image gradient and isolate high frequency

areas or borders detected in the image. The Sobel operator is described in Equation 17:

$$G_x = \begin{bmatrix} -1 & 0 & +1 \\ -2 & 0 & +2 \\ -1 & 0 & +1 \end{bmatrix} * A \quad and \quad G_y = \begin{bmatrix} -1 & -2 & -1 \\ 0 & 0 & 0 \\ +1 & +2 & +1 \end{bmatrix} * A \tag{17}$$

where A is the source image, $*$ denotes the 2-dimensional convolution operation, and G_x and G_y are two images with the horizontal and vertical derivative approximations. The horizontal and vertical derivative approximations are then combined into a resulting overall gradient approximation, G, using Equation 18.

$$G = \sqrt{G_x^2 + G_y^2} \tag{18}$$

The gradient direction at each point, Θ, is calculated using Equation 19.

$$\Theta = atan \left(\frac{G_y}{G_x} \right) \tag{19}$$

A non-maximum suppression algorithm is then run using the calculated image gradient data which searches through the image and determines whether the gradient at each point is at a local maximum in the gradient direction. This algorithm isolates the boundaries of any objects in the image as a set of edge points. The non-maximum algorithm checks each point and determines whether the gradient is maximum there by comparing the gradient value in the gradient direction Θ to the gradient value in the perpendicular directions at that point. If the gradient value in direction Θ at that point is larger, then it is marked as a local maximum point.

Once a set of edge points is calculated, the edges are traced through these points using hysteresis thresholding. Points that are in areas of high intensity gradients are connected to the nearest point using a high gradient threshold which outlines the majority of the 'blob' to be detected with a low uncertainty. Any gaps in the outline are then filled in using a higher uncertainty lower gradient threshold. Once a full

contour is formed, a rectangular bounding box is formed around the object and used as a mask on the original image. The average original image value inside of this mask is then calculated and converted to an average temperature measurement to use in the real-time control scheme.

The Canny edge detection algorithm was run on several trial processing applications and found to have a computation time on the order of 100-150ms for a 640x480 pixel thermal image on a modern Intel Core2Duo CPU. This computation time lowered the usable rate of the thermal imaging camera by 10-20FPS, from 50-60FPS to approximately 30FPS. Although the thermal imaging camera was typically going to be used at a limited rate of 30FPS in the real-time control algorithms, the Canny edge detection algorithm was strenuous on the CPU and limited the available computational power that could be used in the real-time controller itself. Due to these constraints, a more efficient 'blob' detection algorithm was explored, as described in the next subsection.

5.1.0.2   Connected Contour Labeling Algorithm

The second 'blob' detection algorithm operated in linear time and was based upon the work of Chang, Chen, and Lu and Liñán [65, 66]. The algorithm presented operates by sending scan lines or rays from left to right across the image for each row from top to bottom. When a scan line intersects an object, the countour is traced around the object and the object is labeled. An overview of this algorithm is shown in Figure 103.
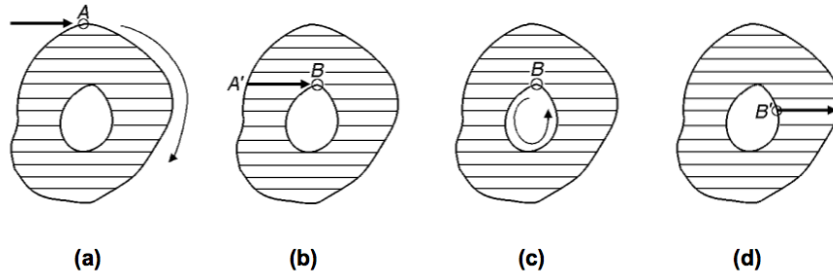
Figure 103: Overview of the connected component labeling algorithm [65].

This connected component labeling algorithm is specifically tailored for operation on binary images and as such, the steps for producing a binary thresholded image above that isolates the melt pool are followed in the same way as in the Canny edge detection algorithm prior to processing in this algorithm. Once a binary image is provided, the algorithm operates in four major steps. Figure 103(a) illustrates the first step in which a scan line encounters a white object at point A for the first time and subsequently traces around the object until point A is once again reached. The contour tracer operates as shown in Figure 104.
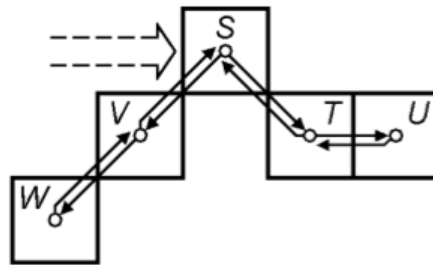
Figure 104: Contour tracing example illustrating traced contour of STUTSVWS [65].

The contour tracing algorithm starts at point S and labels the following point as T. It the proceeds to point T and labels the next point U and so on. The algorithm does not finish until two conditions hold: 1.) The current point is once again S, and 2.) The next point is once again T. For the example in Figure 104, the traced

contour is STUTSVWS. A 'blob' component has additional complexity in that it does not have a single stripe to traverse and the border between internal and external has to be additionally identified. The identification of internal and external points is done as shown in Figure 105 and 106.

(a)   (b)
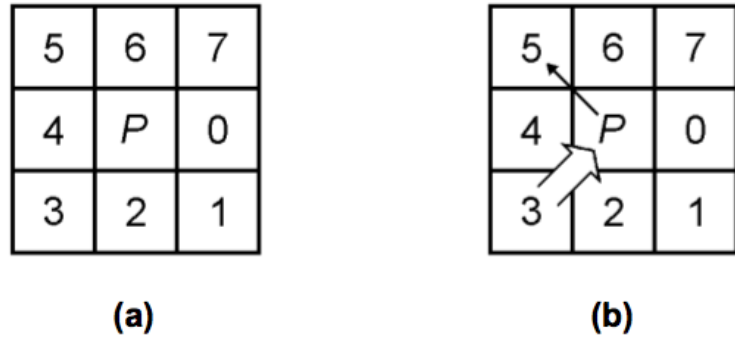
Figure 105: Illustration of clockwise pixel search for a black object on a white background [65].
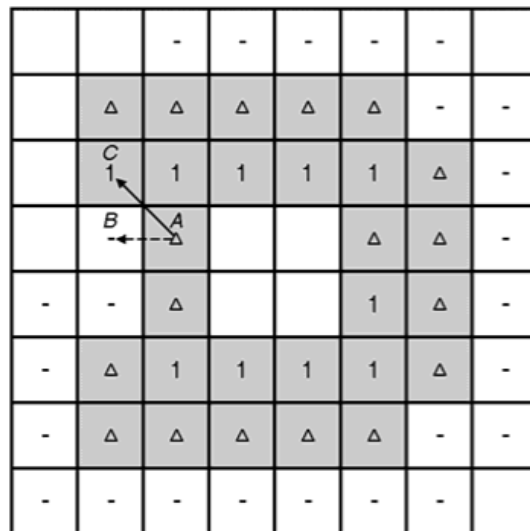
Figure 106: Identification of a black object on a white background. 1: unlabeled black pixels; Δ: labeled black pixels; -: marked white pixels [65].

Figure 105 illustrates how points around a point P are indexed. When labeling a new contour starting at point P, the next point on the contour is first checked in

index 7 because it is known from previous scan lines that the point above P is outside of the blob to be labeled. If point 7 is not found to be inside the blob then points are checked in a clockwise sequence around P until the next point is found. If no point is found around P, then P is an isolated 'blob'. Figure 105b illustrates the case in which a previous contour point had already been found at index 3, in which case the initial position for finding the next pixel is set to index 5 because index 4 must already have been explored. As the contour is traversed, pixels are labeled as illustrated in Figure 106. The final contour is then indicated by the pixels labeled Δ. The algorithm is also capable of finding internal components but in the SLE process, the melt pool is typically a single solid component or 'blob'. Any internal components are labeled using the last three steps in Figure 103. This algorithm only visits each pixel a constant number of times and runs in linear time.

It was found that this connected component labeling system was extremely efficient and was capable of detecting the melt pool and calculating the average melt pool temperature in a time on the order of 5-10ms, which did not limit the framerate of the thermal camera. Additionally, the computation time was stable and did not encumber the CPU, allowing for ample processing power to be left for use by the real-time control scheme. Due to its vastly superior performance as compared to the Canny algorithm, this second connected component labeling algorithm was used for all real-time control trials. An illustration of the detected melt pool is shown in Figure 107 with the major axis perpendicular to the direction of motion indicated.
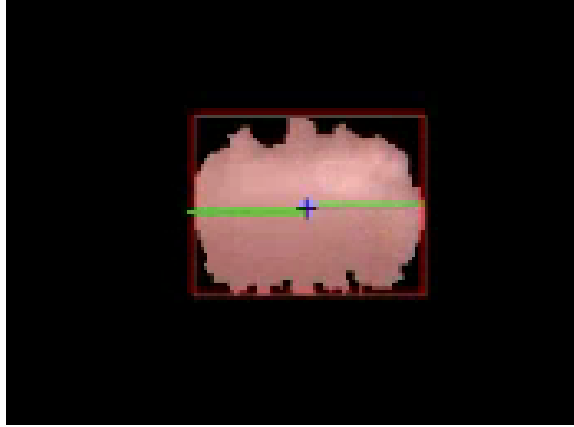
Figure 107: Illustration of the melt pool detected via connected component labeling. Size, eccentricity and average temperature can all be quickly computed for the detected component.

Setting the binary thresholding value allows for detection of different isotherms, the information from which could be utilized in future control schemes. One current limitation of the connected component labeling algorithm is the false extension of the melt pool when a significant buildup of molten powder particles build up in front of the melt pool without falling into the melt pool. This source of noise in the signal occurs when laser power is too low, resulting in the melt pool instability as described in chapter four as well as later in the system identification section of this chapter. Figures 108(a) and 108(b) show contrasting images of the powder falling into the melt front.
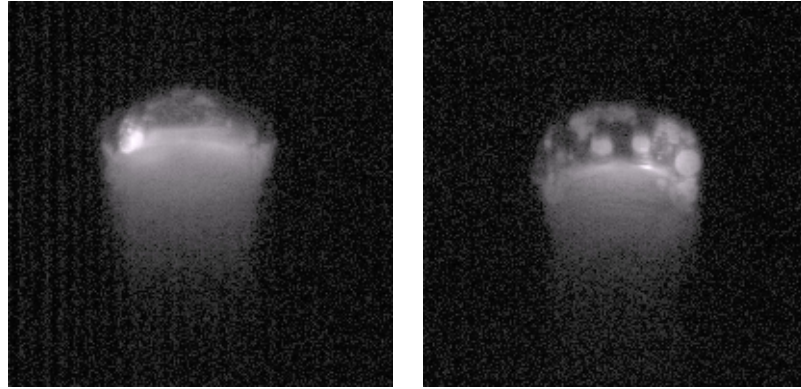
(a) Image of powder flowing smoothly into the melt pool.
(b) Image of powder balling at the melt front due to low laser power.

Figure 108: Contrasting images of powder falling into the melt front.

As can be seen, the accumulation of molten powder balls at the front of the melt pool causes the detected melt pool to significantly expand in size, resulting in additional noise in the recorded temperature signal. This melt pool instability also often results in non-uniform deposits due to a cyclical starvation of powder that occurs after the built up molten balls finally fall into the melt pool leaving less powder in front of the melt.

5.2   Model Development & System Identification

A simplified dynamic thermal model of the SLE process was used for both computational simulation of the control schemes and as a basis for the MRAC control scheme. The simplified dynamic model developed was based upon a lumped capacitance model of the system as illustrated in Figure 109.
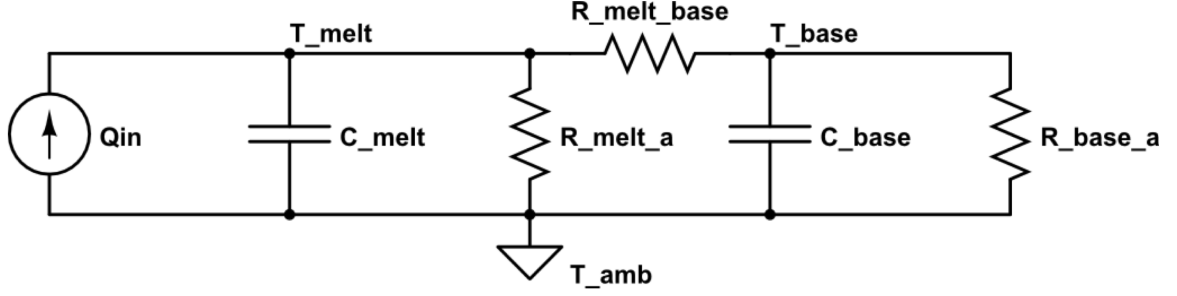
Figure 109: Simplified lumped capacitance thermal model of the SLE process.

Q_{in} is a current source representing the input laser power, T_{melt}, T_{base} and T_{amb} represent the temperature of the melt pool, base substrate, and ambient atmosphere respectively, R_{melta} or R_{1A} is the thermal resistance between the ambient atmosphere and the melt pool, $R_{meltbase}$ or R_{12} is the thermal resistance between the melt pool and base substrate, R_{basea} or R_{2A} represents the thermal resistance between the base substrate and ambient atmosphere, and C_{melt} or C_1 and C_{base} or C_2 represent the thermal capacitance of the melt pool and base substrate respectively. Using this thermal model, the following transfer function can be developed:

$$\frac{1}{R_{12}}X(s) = \left[C_1 s + \frac{1}{R_{1A}} + \frac{1}{R_{12}}\right] Y(s) - U(s) \tag{20}$$

$$\left[C_2 s + \frac{1}{R_{2A}} + \frac{1}{R_{12}}\right] X(s) = \frac{1}{R_{12}}Y(s) \tag{21}$$

Where $X(s)$ is the substrate temperature. Combining these equations yields:

$$R_{12}^2 \left[C_2 s + \frac{1}{R_{2A}} + \frac{1}{R_{12}}\right] \left[\left[C_1 s + \frac{1}{R_{1A}} + \frac{1}{R_{12}}\right] Y(s) - U(s)\right] = Y(s) \tag{22}$$

Simplifying gives the final transfer function relating input laser power, $U(s)$ to output melt pool temperature, $Y(s)$:

$$\frac{Y(s)}{U(s)} = \frac{C_2 s + \frac{R_{12}+R_{2A}}{R_{12}R_{2A}}}{C_1 C_2 s^2 + \left[\frac{C_1(R_{2A}+R_{12})}{R_{2A}R_{12}} + \frac{C_2(R_{1A}+R_{12})}{R_{2A}R_{12}}\right] s + \left[\frac{R_{2A}+R_{12}}{R_{2A}R_{12}}\right]\left[\frac{R_{1A}+R_{12}}{R_{1A}R_{12}}\right] + \frac{1}{R_{12}^2}} \tag{23}$$

As can be seen, this transfer function is a second order representation of the system, with one zero and two poles, and an output representing the temperature of the melt

130

pool. This continuous time model can be transformed into a discrete time z-domain representation using any of the standard techniques in literature, but it will remain the same order after transformation [67]. Prior literature on control in reasonably similar welding processes as described in chapter two also indicated that the heating and cooling experienced during welding operations could be described as a second order system. Due to the difficulty in determining exact values for the capacitances and resistances seen during processing, a grey box approach was used to determine the transfer function parameters to be used for simulation purposes. On the basis of this second order model, a set of system identification experiments were run to determine the parameters of the simplified model.

System identification was conducted in the time domain using a series of step inputs, as illustrated in Figure 110. Identification of the second order system model was done by analyzing the temperature response of the step input in laser power and using an autoregresive model with external (ARX) input modeling algorithm as described by Ljung [68] to determine the model matching the input to the output data.

An illustration of the input voltage and output temperature measurement for the step input used is shown in Figure 110.
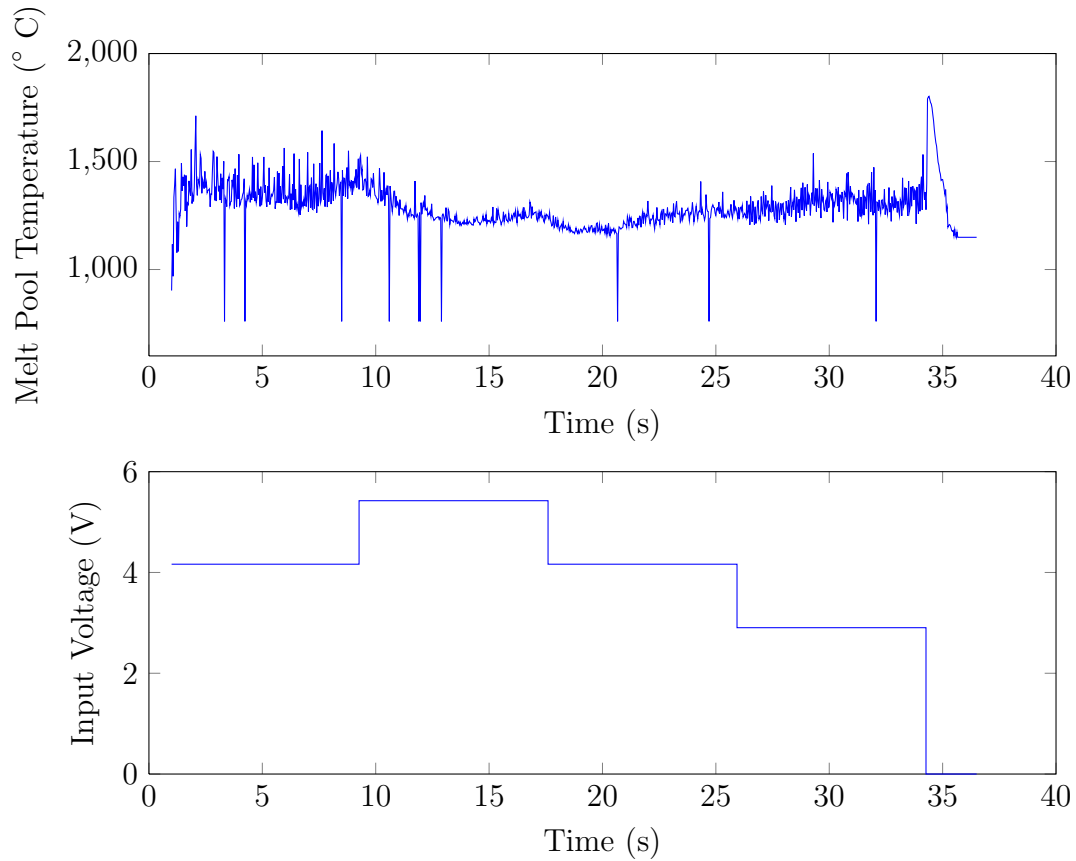
Figure 110: Step response of the SLE process with 450 repeat scans at 450W laser power. Three steps were provided at laser powers of 600W, 450W, and 300W. Data was gathered at a rate of 30Hz.

It can be seen in the measured temperature data that the signal gets noisy when the laser power drops to the low value. This signal noise was due to melt pool instability caused by the low laser power. When the laser power was too low, the melt pool became discontinuous and would not adequately gather powder from the front, resulting in the molten ball buildup. These particles would then be seen by the thermal camera and detected as a part of the melt pool by the connected component labeling algorithm, causing a significant change in size and temperature of the detected melt pool as the balls of molten powder accumulated and then fell into the melt pool.

To avoid extreme amounts of noise caused by melt pool discontinuity, a lower

control saturation limit of 2V or approximately 200W was set for all control trials. Additionally, an upper saturation limit of 6V or approximately 600W was set by the limitations inherent to the mirrors inside of the galvanometer scanner. Above this threshold, there was risk of damaging the scanner window or mirror coatings.

Additionally, several sharp drops can be seen in the temperature response. Each of these nine drops represent a time step for which no melt pool was detected, likely due to a flame, excess smoke, or another anomaly impeding the view of the thermal camera. To alleviate any issues with dropped frames and remove excess noise, a short finite impulse response (FIR) moving average filter was implemented in the control schemes.

The transfer function resulting from ARX modeling of the step response in Figure 110 with one unit of time delay is listed in Equation 24.

$$\frac{Y(z)}{U(Z)} = z^{-1}\frac{0.1501z^{-1}}{1 - 1.978z^{-1} + 0.9783z^{-2}} \tag{24}$$

A comparison between the response of this transfer function and a portion of the step response are plotted against one another in Figure 111.
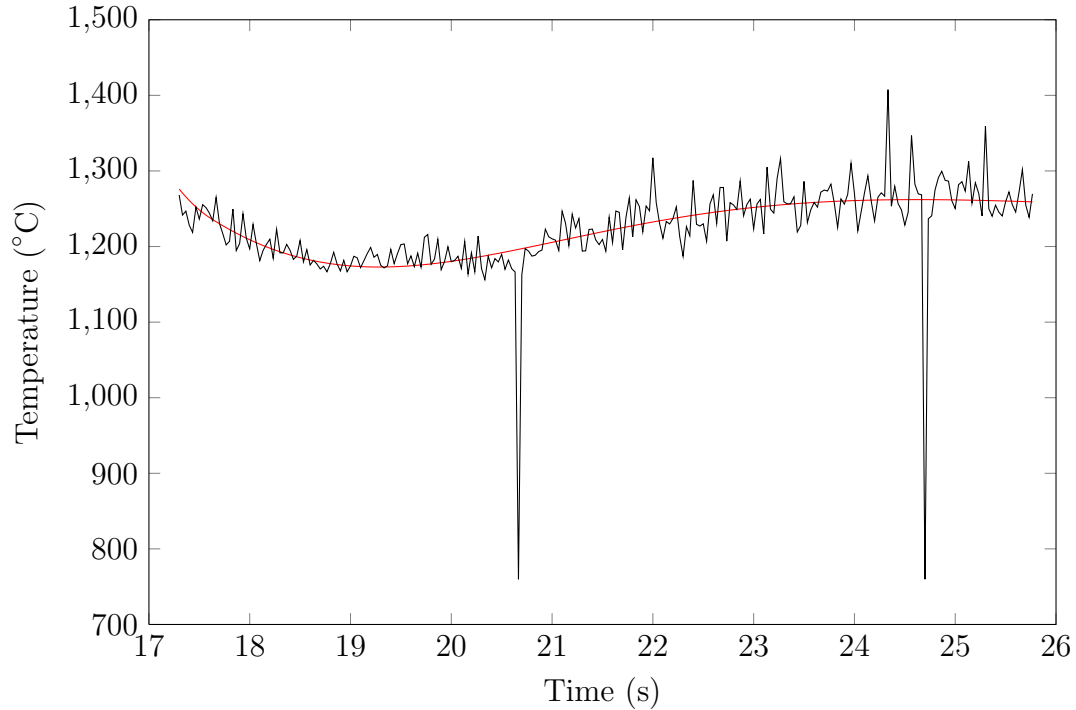
Figure 111: Comparison of the simulated transfer function output in red with the actual system response in black. The two sharp dips indicate frames in which no melt pool was detected.

This transfer function model was used for development of the control schemes via simulation as well as determination of PID gains to be used during experimentation. One additional key result of this step response is the indication of an increase in temperature towards the end of each step. This increase is due to the buildup in substrate heat as the scanning proceeds, and it causes a significant change in the heat transfer characteristics of the process during scanning.

5.3   *Real-time Control Schemes*

This section covers the development of two control schemes, one traditional PID control scheme and a second model reference adaptive control (MRAC) scheme. An overview of the control inputs, feedback signals, potential disturbances and noise sources are listed in Table 10.

Table 10: Overview of control parameters and signals.

Controllable Parameters	Feedback Signals	Disturbances	Noise Sources
Laser Power	Melt pool temperature	Excess powder falling into melt	Thermal camera uncertainty
Scan Speed	Melt pool size	Laser power fluctuation	Flames
Scan Pattern	Melt pool shape	Inclusions	Smoke
		Substrate variation	Melt pool instability
		Powder variation	Emissivity fluctuation
			Dropped camera frames

For the purposes of this work, the system was treated as a single-input single-output (SISO) system treating laser power as the only controllable input and average melt pool temperature as the only system output. Future work on control of the SLE process could expand on this to utilize more of the controllable inputs of feedback signals. PID control was first attempted to determine whether simple control was capable of controlling the complex SLE process. Due to performance constraints, it was found that PID control alone would not be sufficient, and thus a simplified MRAC control scheme was also implemented. Both control schemes operated in the discrete time domain due to the 60 Hz limitation of the thermal imaging sensor.

5.3.1 PID Control

An overview of the PID control scheme is shown in Figure 112.
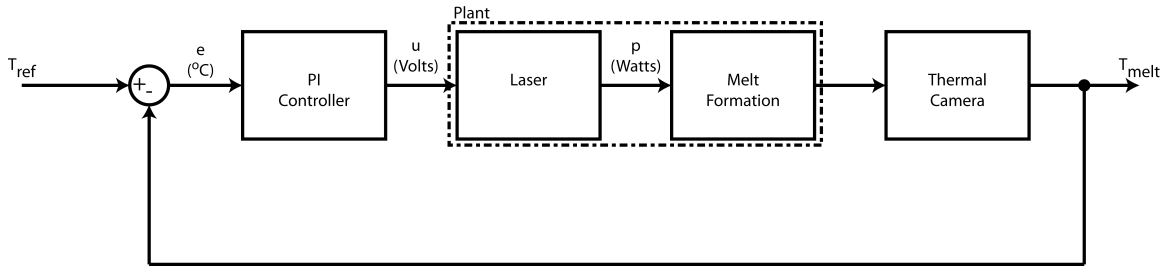
Figure 112: Overview of the PI control scheme.

Due to the significant amount of signal nose in the system, the derivative term was avoided to limit extreme amounts of actuation that could be caused by the highly fluctuating noise. The discrete PI controller used was then developed as follows starting with the general transfer function form of the discrete PID controller with proportional, integral and derivative gains taken as K_p, K_i and K_d respectively:

$$\frac{U[z]}{E[z]} = K_p + K_i \frac{T_s}{2} \frac{z+1}{z-1} + K_d \frac{z-1}{zT_s} \tag{25}$$

$$\frac{U[z]}{E[z]} = \frac{\left(K_p + K_i \frac{T_s}{2} + \frac{K_d}{T_s}\right) z^2 + \left(-K_p + K_i \frac{T_s}{2} - \frac{2K_d}{T_s}\right) z + \frac{K_d}{T_s}}{z^2 - z} \tag{26}$$

Taking

$$a = \left(K_p + K_i \frac{T_s}{2} + \frac{K_d}{T_s}\right) \tag{27}$$

$$b = \left(-K_p + K_i \frac{T_s}{2} - \frac{2K_d}{T_s}\right) \tag{28}$$

$$c = \frac{K_d}{T_s} \tag{29}$$

gives

$$U[z] = z^{-1}U[z] + aE[z] + bz^{-1}E[z] + cz^{-2}E[z] \tag{30}$$

$$u[k] = u[k-1] + ae[k] + be[k-1] + ce[k-2] \tag{31}$$

In this form, u at the current timestep, $u[k]$ is solely determined by the prior input $u[k-1]$, the current error, $e[k]$, and the prior two errors, $e[k-1]$ and $e[k-2]$ which can be easily implemented in the control software. The control signal was also modified to add saturation limits at 2 volts and 7 volts. The 2 volt lower limit maintained enough input power to form a continuous and stable melt pool, and the 7 volt upper limit prevented damage to the galvonometer scanner as a result of the input laser power being too high. The gains for the PI control scheme were developed using the MATLAB PID Tuner tool on the identified system model. Figure 113 shows the step response of the developed controller.
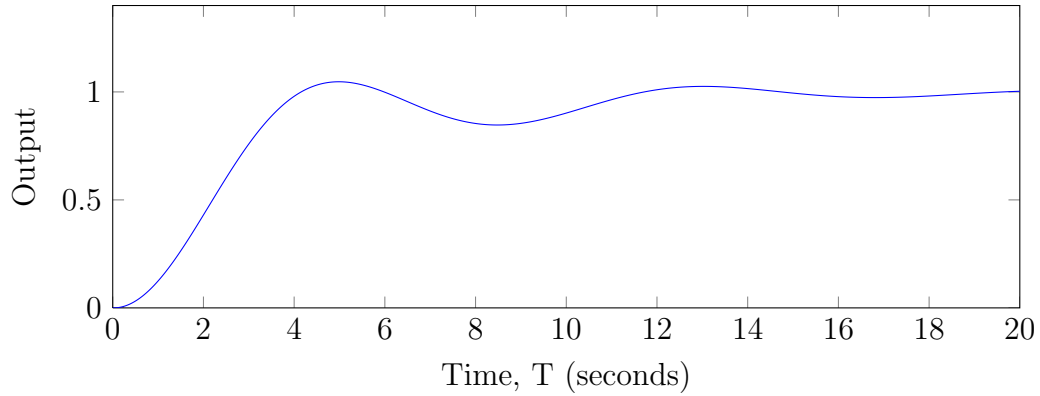
Figure 113: Step response of applying the PI controller to the transfer function in Equation 24. The PI controller was developed with a 3.46 second response time. The settling time is approximately 18 seconds. $K_p = 0.0020374$ and $K_i = 0.0012278$.

The gains chosen for this controller were based on the identified system model and although they were within the proper range of controller gains to control the actual process, the chosen gains resulted in a sub-optimal response. This was due to the identified system not exactly matching the actual system. As discussed later in the results, the PI controller developed here properly tracked a reference melt pool temperature for several different temperatures but the performance was poor and required additional tuning. To avoid the significant time and material investment required to tune the PID gains for optimal performance, a second adaptive control algorithm was developed.

5.3.2   One Step Ahead Adaptive Control Scheme

Due to the relatively high number of experiments required to tune the PID controller, as well as its poor performance in some cases, a second controller based on a model reference adaptive control (MRAC) scheme was developed. The particular form of MRAC chosen was the one step ahead adaptive control scheme (OSAAC). An overview of the OSAAC scheme is shown in Figure 114.
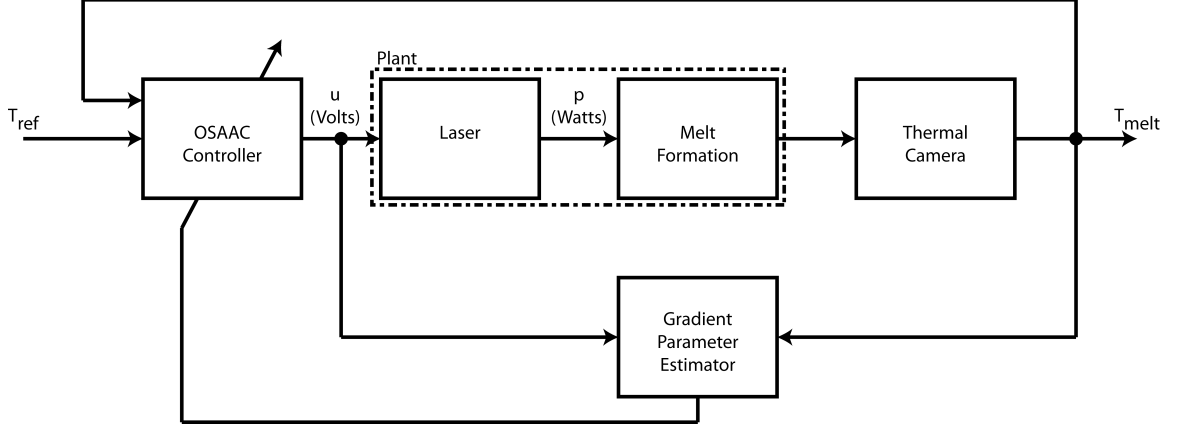
Figure 114: Overview of the OSAAC scheme.

The OSAAC scheme used in this work is a special case of the general model reference adaptive controller that achieves perfect tracking and can be used in discrete time systems when the time delay d in the system is known and the reference input is known more than d time steps in advance. In the case of real-time control of the SLE process, the reference temperature is to be determined prior to experimentation using the robust offline model, and as such, the entire reference temperature profile is available for use during processing. For these reasons, a one step ahead adaptive controller was developed to be used for the SLE process as it would provide the most optimal control out of the model reference adaptive family of controllers. The OSAAC scheme is an idealized form of the general direct MRAC scheme, where the poles of the reference model are taken as zero; in discrete time this represents the fastest stable response.

The controller is developed such that the output of the system, y_p can be put in the form of parametric model with an unknown parameter vector, θ and a vector containing a sequence of known values, ϕ_p as in Equation 59.

$$y_p(k) = \theta^T \phi_p(k - n^*) \tag{32}$$

Development of the simpler one step ahead control scheme begins by taking the plant, in this case the second order SLE process model, and putting it into discrete

138

auto-regressive moving average form (DARMA) [69, 70]. This one step ahead control scheme is then altered to incorporate adaptation for unknown plant parameters. The development of the one step ahead controller begins as follows, given a plant y_p:

$$y_p = \frac{\bar{Z}_p(z)}{R_p(z)} u_p \tag{33}$$

Where $\bar{Z}_p(z) = b_m z^m + b_{m-1} z^{m-1} + ... + b_1 z + B_0$, $R_p(z) = z^n + a_{n-1} z^{n-1} + ... + a_1 z + a_0$ and $n > m$. Letting $q^{-1} = z^{-1}$ be the shift operator we can define

$$A(q^{-1}) \triangleq z^{-n} R_p(z)|_{z^{-1}=q^{-1}} = 1 + a_{n-1} q^{-1} + ... + a_1 q^{-n+1} + a_0 q^{-n} \tag{34}$$

$$B(q^{-1}) \triangleq z^{-n} \bar{Z}_p|_{z^{-1}=q^{-1}} = q^{-n} q^m (b_m + b_{m-1} q^{-1} + ... + b_0 q^{-m}) = q^{-n^*} \bar{B}(q^{-1}) \tag{35}$$

Where $\bar{B}(q^{-1}) = b_m + b_{m-1} q^{-1} + ... + b_0 q^{-m}$ and $n^* = n - m$ is the relative degree of the plant. Using these relations, the plant can be represented as the DARMA model:

$$A(q^{-1}) y_p(k) = q^{-n^*} \bar{B}(q^{-1}) u_p(k) \tag{36}$$

which can then be put into the predictor form as follows:

$$y_p(k + n^*) = \alpha(q^{-1} y_p(k)) + \beta(q^{-1}) u_p(k) \tag{37}$$

where

$$\beta(q^{-1}) = b_m + \beta_1 q^{-1} + ... + \beta_{n-1} q^{-n+1} = f(q^{-1}) \bar{B}(q^{-1}) \tag{38}$$

$$\alpha(q^{-1}) = \alpha_0 + \alpha_1 q^{-1} + ... + \alpha_{n-1} q^{-n+1} \tag{39}$$

and

$$f(q^{-1}) = 1 + f_1 q^{-1} + ... + f_{n^*-1} q^{-n^*+1} \tag{40}$$

are the unique polynomials satisfying the equation

$$f(q^{-1}) A(q^{-1}) + q^{-n^*} \alpha(q^{-1}) = 1 \tag{41}$$

whose coefficients are computed as:

$$f_0 = 1 \tag{42}$$

$$f_i = -\sum_{j=0}^{i-1} f_j a_{n-i+j}, \quad i = 1, ..., n^* - 1 \tag{43}$$

$$\alpha_i = -\sum_{j=0}^{n^*-1} f_j a_{n-i-n^*+j}, \quad i = 1, ..., n-1 \tag{44}$$

where $a_j = 0$ for $j < 0$.

Taking the predictor form from above, the parametric model can be constructed:

$$y_p(k + n^*) = \theta^{*^T} \phi_p(k) \tag{45}$$

where

$$\phi_p(k) = [y_p(k), y_p(k-1), ..., y_p(k-n+1), u_p(k), u_p(k-1), ..., u_p(k-n+1)]^T \tag{46}$$

For known plant parameters the parameter vector, $\theta(k)$, is then:

$$\theta^* = [\alpha_0, \alpha_1, ..., \alpha_{n-1}, b_m, \beta_1, ..., \beta_{n-1}]^T \tag{47}$$

Taking the predictor form, the control law $u_p(k)$ can be developed with the objective of driving the output of the plant, $y_p(k)$ to track the reference signal, $y_m(k)$:

$$\beta(q^{-1})u_p(k) = y_m(k + n^*) - \alpha(q^{-1})y_p(k) \tag{48}$$

This yields the control law:

$$u_p(k) = \frac{1}{b_m}(y_m(k + n^*) - \alpha(q^{-1})y_p(k) - \bar{\beta}(q^{-1})u_p(k-1)) \tag{49}$$

where

$$\bar{\beta}(q^{-1}) \triangleq (\beta(q^{-1}) - b_m) \tag{50}$$

Choosing this control law results in perfect tracking after n^* time steps:

$$y_p(k + n^*) = y_m(k + n^*) \tag{51}$$

This control form is modified as follows for adaptation of unknown plant parameters:

$$u_p(k) = \frac{1}{\hat{b}_m + \lambda}(y_m(k + n^*) - \hat{\alpha}(q^{-1}, k)y_p(k) - \hat{\bar{\beta}}(q^{-1}, k)u_p(k-1)) \tag{52}$$

where

$$\hat{\alpha}(q^{-1}, k) = \hat{\alpha}_0(k) + \hat{\alpha}_1(k)q^{-1} + \dots + \hat{\alpha}_{n-1}(k)q^{-n+1} \tag{53}$$

$$\hat{\beta}(q^{-1}, k) = \hat{\beta}_1(k) + \hat{\beta}_2(k)q^{-1} + \dots + \hat{\alpha}_{n-1}(k)q^{-n+2} \tag{54}$$

The constant term $\lambda > 0$ was added to weigh down the influence of the previous input $u_p(k-1)$, limiting excessive amounts of control effort that could otherwise occur when trying to drive the system to perfect tracking. The parameter vector is:

$$\theta(k) = [\hat{\alpha}_0(k), \hat{\alpha}_1(k), \dots, \hat{\alpha}_{n-1}(k), \hat{b}_m(k), \hat{\beta}_1(k), \dots, \hat{\beta}_{n-1}(k)]^T \tag{55}$$

The parameter vector can then be estimated using one of several algorithms, including gradient, projection, or least squares algorithms. In this work, a gradient algorithm was used, resulting in the following update equations:

$$\epsilon(k) = \frac{y_p(k) - \theta^T(k)\phi_p(k - n^*)}{m_s^2(k - n^*)} \tag{56}$$

$$\bar{\theta}(k+1) = \bar{\theta}(k) + \gamma \epsilon(k)\bar{\phi}_p(k - n^*) \tag{57}$$

$$\bar{b}_m(k+1) = \hat{b}_m(k) + \gamma \epsilon(k)\phi_{n-m}(k) \tag{58}$$

$$m_s^2(k) = 1 + \phi^T(k)\phi(k) \tag{59}$$

where γ is a chosen constant adaptive gain vector. Using these update equations and the weighted adaptive control law in Equation 52, the OSAAC scheme was implemented in the C# software with an unknown parameter vector that represented the single zero and two poles of the modeled transfer function for the SLE process. The Math.net Numerics package was utilized to efficiently implement the linear algebra operations required for the calculation of the update laws and control input signal [71].

5.3.3 Sampling Rate

The control system sampling rate to use was determined and justified through the use of several pseudorandom binary signal inputs, one of which is illustrated in Figure 115.
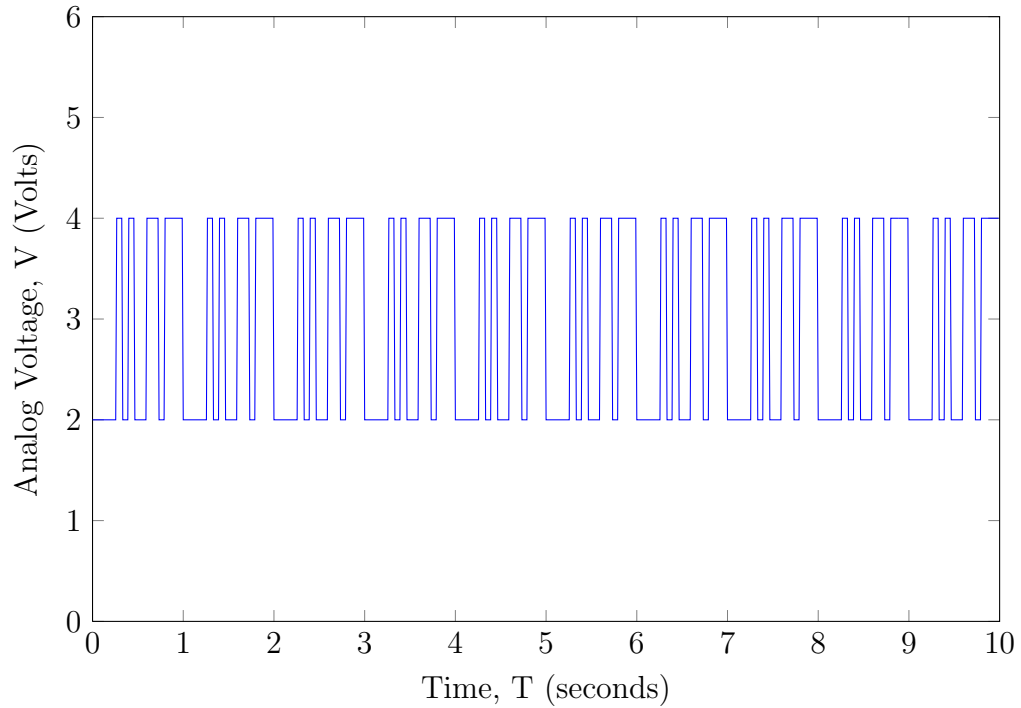
Figure 115: Example pseudorandom binary signal of approximately 5Hz used for determining system bandwidth requirements.

When using a higher frequency pseudorandom signal, such as one at approximately 30Hz, it was found that the resulting deposit quality was somewhat independent of the signal. At high frequencies, the deposited material looked as though it had been deposited at an average value of the two extreme values in the pseudorandom signal. Figures 116(a), 116(b), and 116(c) illustrate samples run with different frequency pseudorandom signals, demonstrating that running at high frequency resulted in a more uniform deposit that would be produced at the average power of the signal.

(a) Image of a sample run with an approx- (b) Image of a sample run with an approx-
imately 5Hz pseudorandom signal.   imately 20Hz pesudorandom signal.

(c) Image of a sample run with an ap-
proximately 30Hz pesudorandom signal.

Figure 116: Images of as-processed René-80 samples run with varied frequency laser
power signals.

For this reason, 30Hz was chosen as the sampling period for the thermal camera
and control system. At this frequency, the system was guaranteed to be high enough
bandwidth to saturate the limit on deposit quality that could be achieved via SLE
but low enough to allow for overhead room on the control computer to detect the
melt pool and algorithmically generate the input control signal.

5.4 Experimental Trials

The purpose of the control trials were to determine whether it was feasible to control the melt pool temperature of the SLE process by using a thermal imaging camera and modulating the laser power. As such, the scan speed and number of repeat scans were fixed at values that produced a good set of results from the prior open loop DoE analysis run on René-80 and described in Chapter 4. In this case, the scan speed was set to 450 mm/sec and the repeat scans to initiate the melt pool were also set at 450. In all trials, the repeat scans were allowed to complete at 450W power and initiate the melt pool before the controller was turned on. Limitations on the lower temperature bounds of the thermal camera prevented feedback control during the repeat scans. Implementation of a thermal camera supporting a lower temperature range would enable precise feedback control of the repeat scans as well.

The first set of feedback control trials were attempted using the PI controller. The results of two of these trials are shown in Figures 117 and 118.
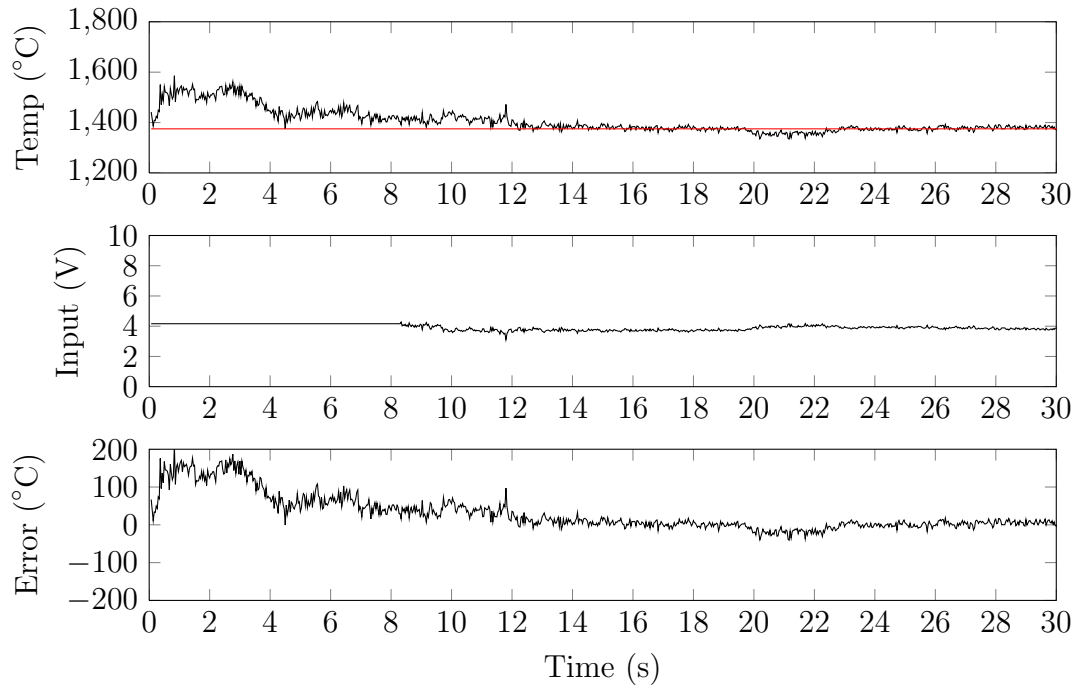
Figure 117: PI trial run with a reference temperature of 1375 $°C$ highlighted in red. PI control starts after repeat scans at a time of 8.3 seconds. Average error during control of 5.00 $°C$
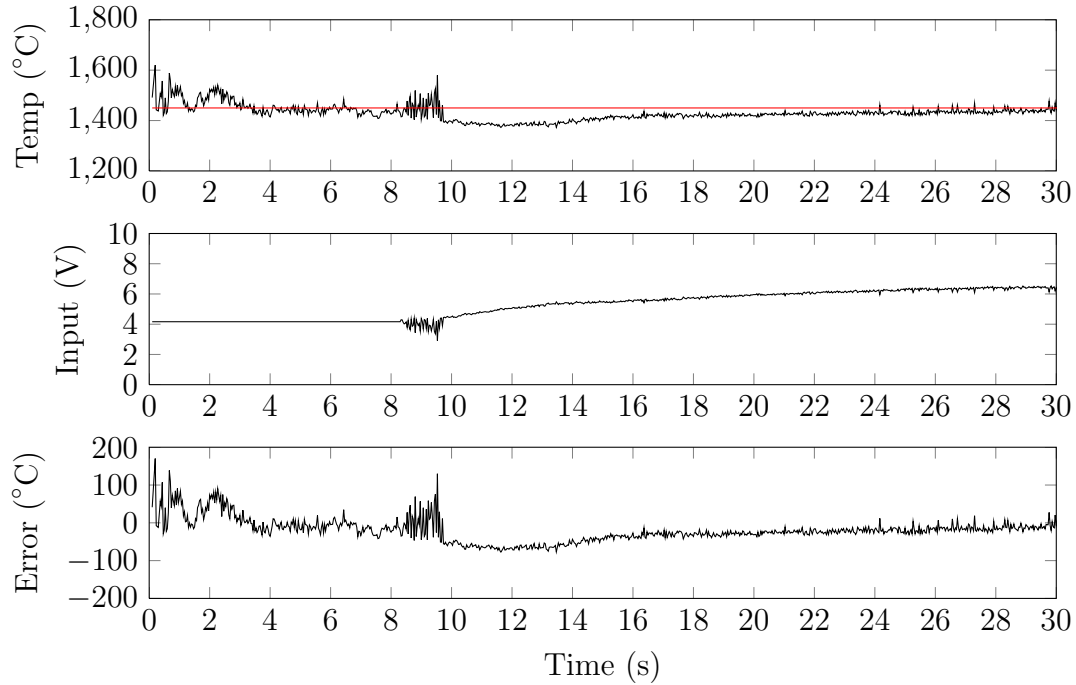
Figure 118: PI trial run with a reference temperature of 1450 $°C$ highlighted in red. PI control starts after repeat scans at a time of 8.3 seconds. Average error during control of -25.40 $°C$

It can be seen from these plots that the PI gains chosen were able to track the set reference temperature for both cases, but the second trial shows an extremely slow response and high average error for the PI gains that were chosen by simulation. The settling time in the case of the second trial was approximately 12 seconds. This settling time was somewhat expected due to the simulated responses for the PI controller applied to the identified model earlier in this chapter. Additional more aggressive tuning of PI gains may have improved performance, but determination of these PID gains would likely require a significant number of trials, on the order of twenty or more samples run as part of a DoE. It was also found from the simulated PI controller that determination of proper gains that resulted in fast response, low overshoot, and short settling time may not even be possible for this system using the PI controller. The gains used for the implemented controller were already chosen due

146

to the fact that they displayed a good trade off between each of those metrics. Even in the case of this idealized simulated controller, the settling time was relatively unacceptable when considering that processing of a full sample ends within 30 seconds. Due to the high cost of each experimental trial, the lack of an outlook suggesting that higher performance could be achieved and the desire to utilize the feedback control to produce high quality samples without time consuming and costly DoE analysis, the adaptive control scheme was explored.

Before the adaptive control scheme trials, it was determined that the several instances of scanner window damage that had occurred in the past were due to smoke accumulation on the window during processing. To avoid additional downtime, a smoke extraction system was implemented before experimentation from PID trials continued on towards experimentation on adaptive feedback trials, as shown in Figure 119.
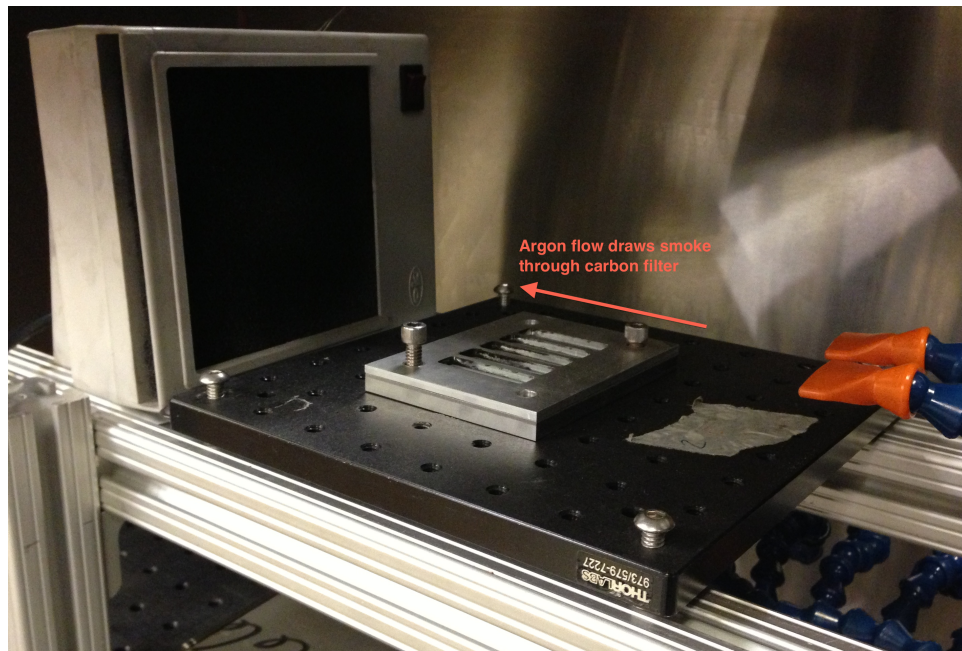
Figure 119: Image of the smoke extractor system put in place that draws an Argon flow over the top of the samples to capture any smoke developed during processing.

The additional convective currents formed above the melt pool associated with

this smoke extraction system caused a significant alteration in the quality of deposits that could be produced via SLE. An example of an open loop deposit at previously identified ideal processing parameters developed in Chapter 4 but now created with the smoke extractor in place is shown in Figure 120.
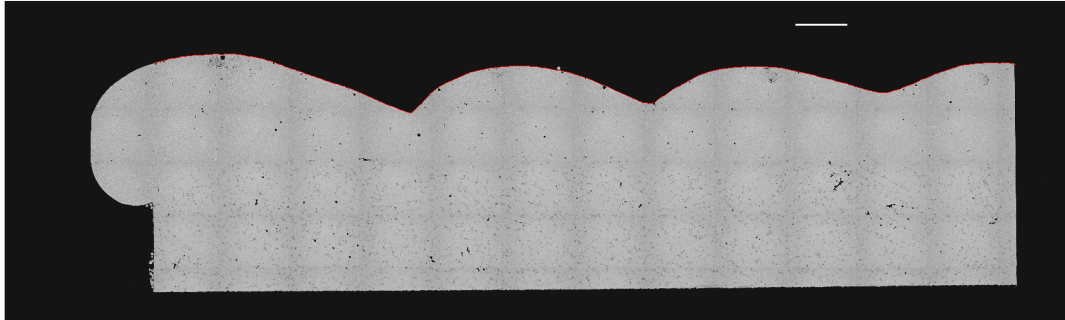
Figure 120: Micrograph of a sample run at 450 repeats with 450W laser power and 450mm/sec scan speed with the smoke extractor system in place. Scale bar of 1mm length.

A similar waviness was also found in the detected average melt pool temperature during processing of this sample, as illustrated in Figure 121.
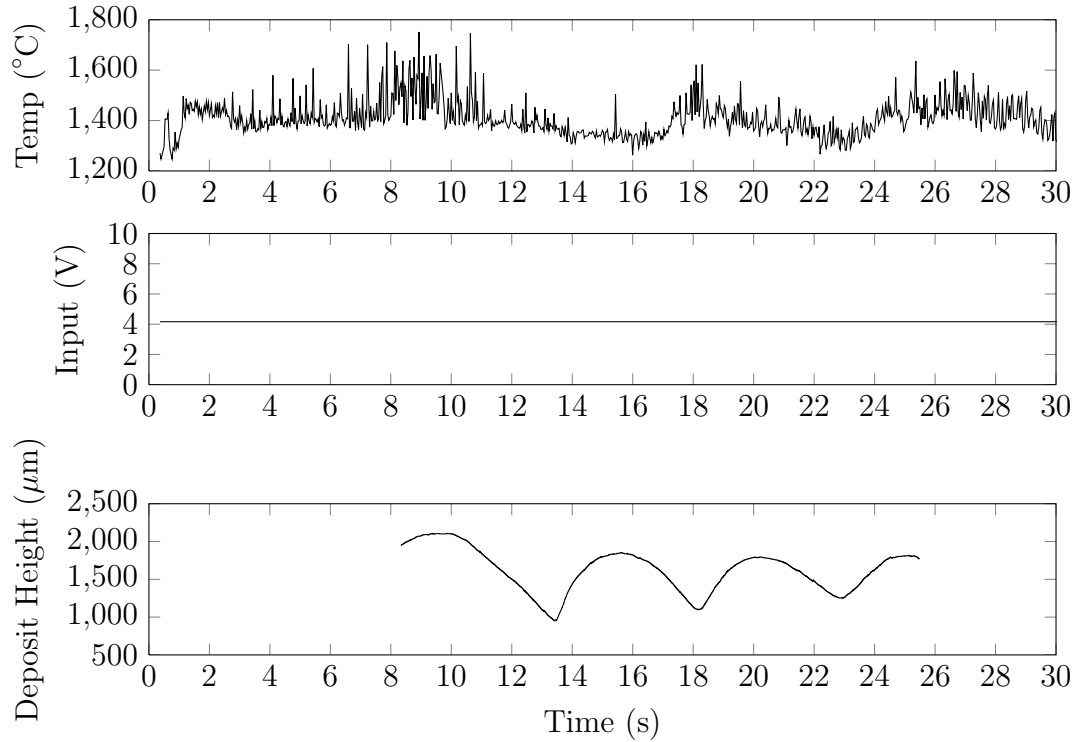
Figure 121: Measured temperature profile for the open loop trial with smoke extractor in place. Deposit height as measured off of the micrograph of the first three quarters of the sample is also plotted for comparison with the temperature profile.

Despite these new issues found during open loop trials with smoke extraction in place, closed loop adaptive control trials were still conducted with the smoke extractor in place to prevent additional scanner damage.

Determination of controller parameters was easier when using the adaptive control scheme. To initially determine the initial conditions for the plant parameters, the weighting term λ was set to a small value so that the adaptation algorithm would quickly converge to values near the proper operating point due to significant excitation of the laser power input and resulting temperature output of the system. After this initial identification experiment as illustrated in Figure 122, the end values of the adaptation parameters were set as the initial values for future experiments.

149
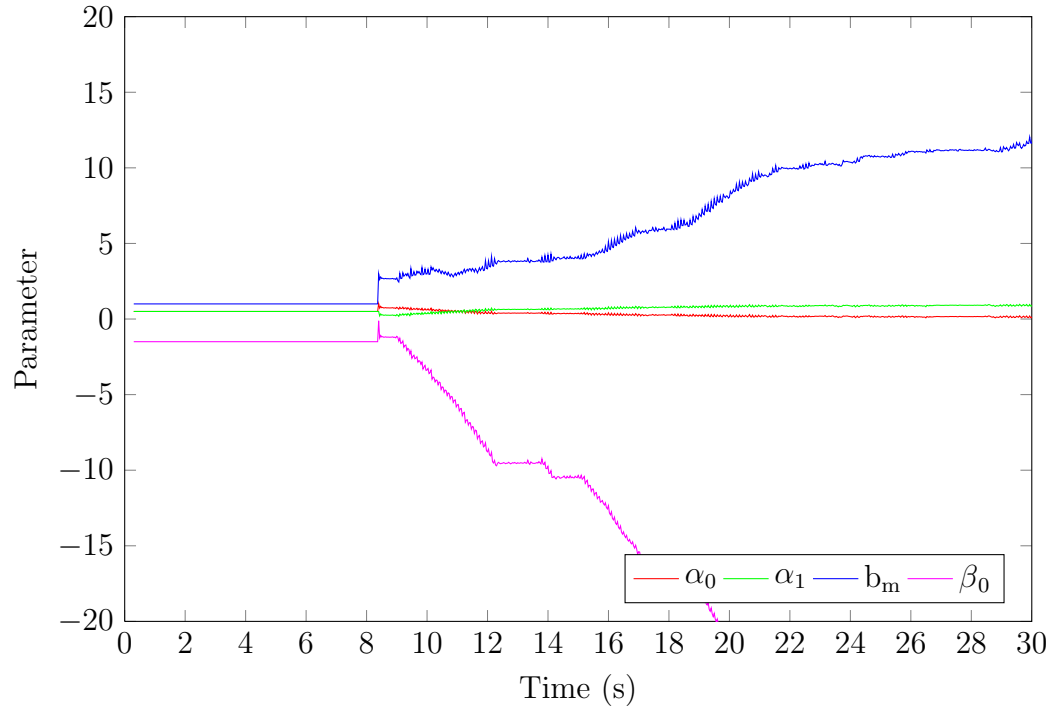
Figure 122: Plot showing parameter adaptation under significant system excitation.

Using this strategy, controller parameters could be determined with a minimal number of experiments. For the adaptive trials run in this chapter, initial parameter identification was done using only three total trials.

Several trials were run with the OSAAC scheme on René-80 to determine whether altering the temperature profile had any effect on the deposit height or uniformity. Figures 123 and 124 show the results of running with a constant reference temperature.
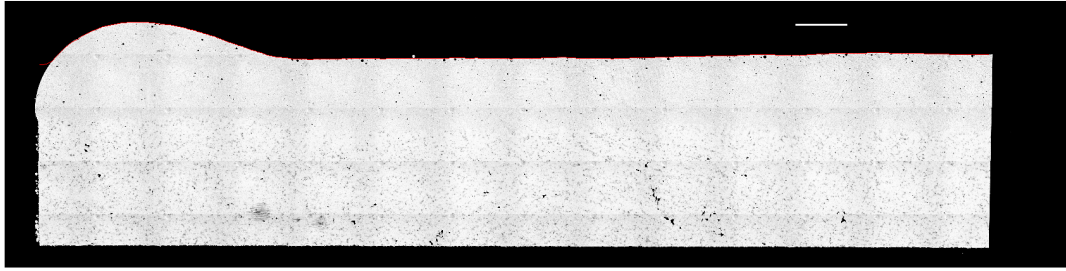
Figure 123: Micrograph of a sample run with a constant reference temperature of 1575 $°C$ demonstrating the most uniform deposit produced to date. Scale bar of 1mm length.

Even in the presence of the smoke extractor, the resulting deposit shows a remarkable uniformity of which had not been seen in all of the open loop trials run to date. This level of deposit uniformity will be required when moving the SLE process towards multi-layer deposition, as major variations in deposit height will significantly impact deposition of subsequent layers of material.

Figures 125 and 126 show the results of running with a higher constant reference temperature of 1650 $°C$.

Figure 125: Micrograph of a sample run with a constant reference temperature of 1650 $°C$ demonstrating a higher deposit height than the lower reference temperature. Scale bar of 1mm length.
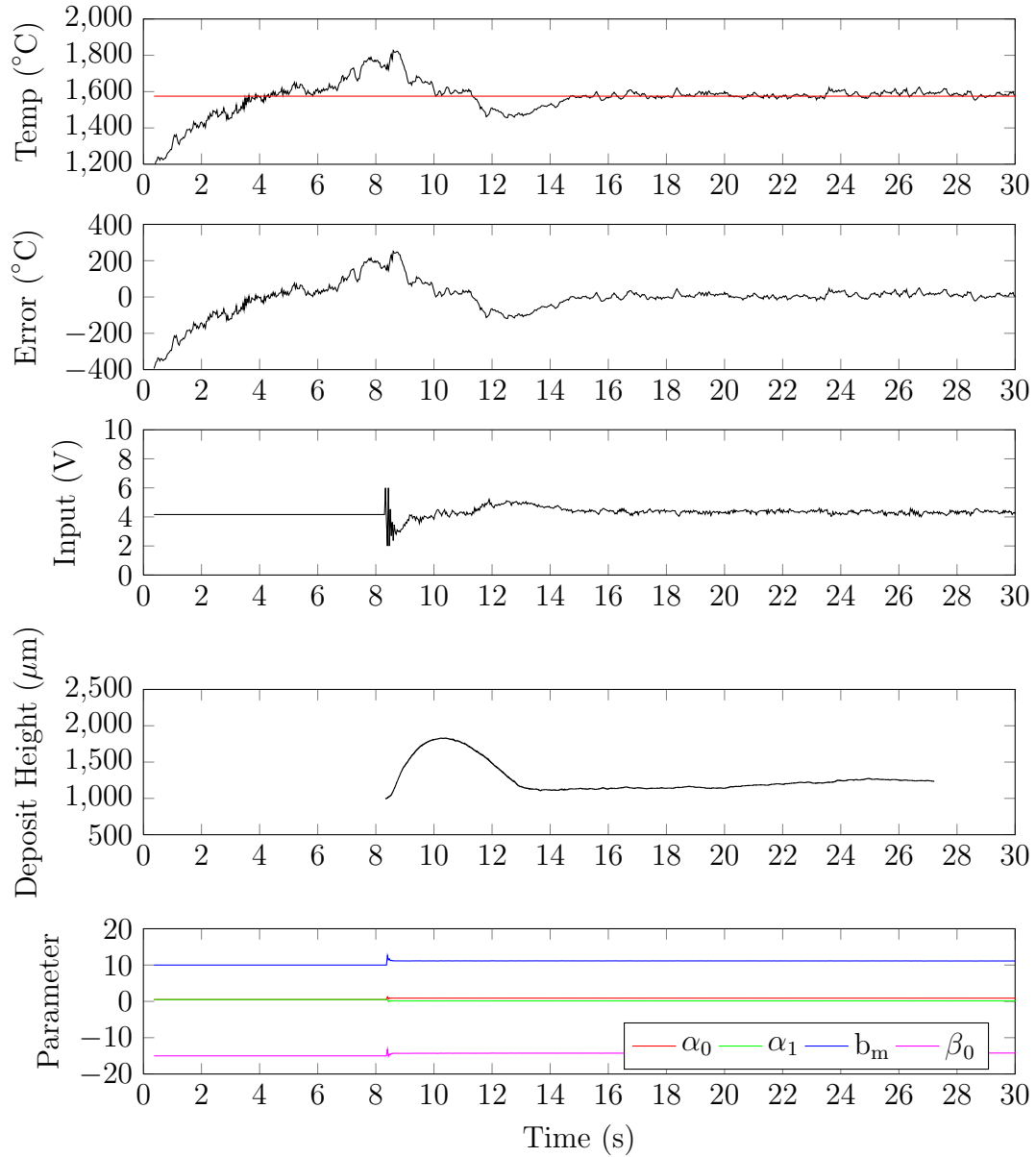
Figure 124: Measured temperature profile for a trial with a constant 1575 $°C$ reference temperature. Average error of 2.15 $°C$.

The higher constant reference temperature of $1650°C$ again produced a high uniformity deposit of approximately 200 μm higher thickness than the lower reference temperature trial.

Figure 127 shows the results of running with a linear ramp down in reference temperature. The temperature profile follows the ramp down in reference temperature
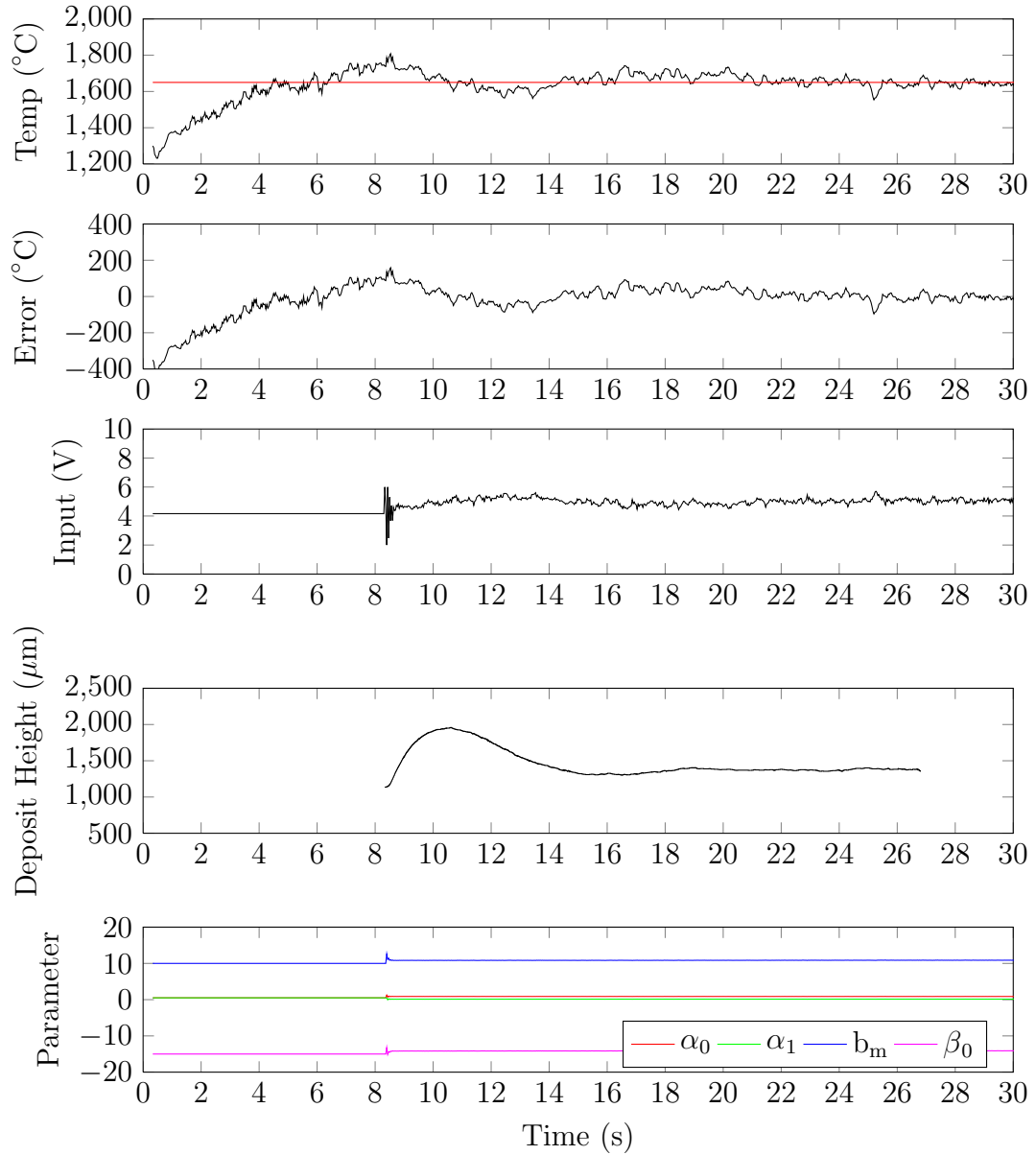
Figure 126: Measured temperature profile for a trial with a constant 1650 $°C$ reference temperature. Average error of 5.80 $°C$.

well, resulting in low average error. Although the deposit height is not as uniform as in the case of the constant temperature case, it is still more uniform than all prior open loop trials.

Figure 128 shows the results of running with a step up in reference temperature in the middle of the sample. It can be seen that a large step in reference temperature

153
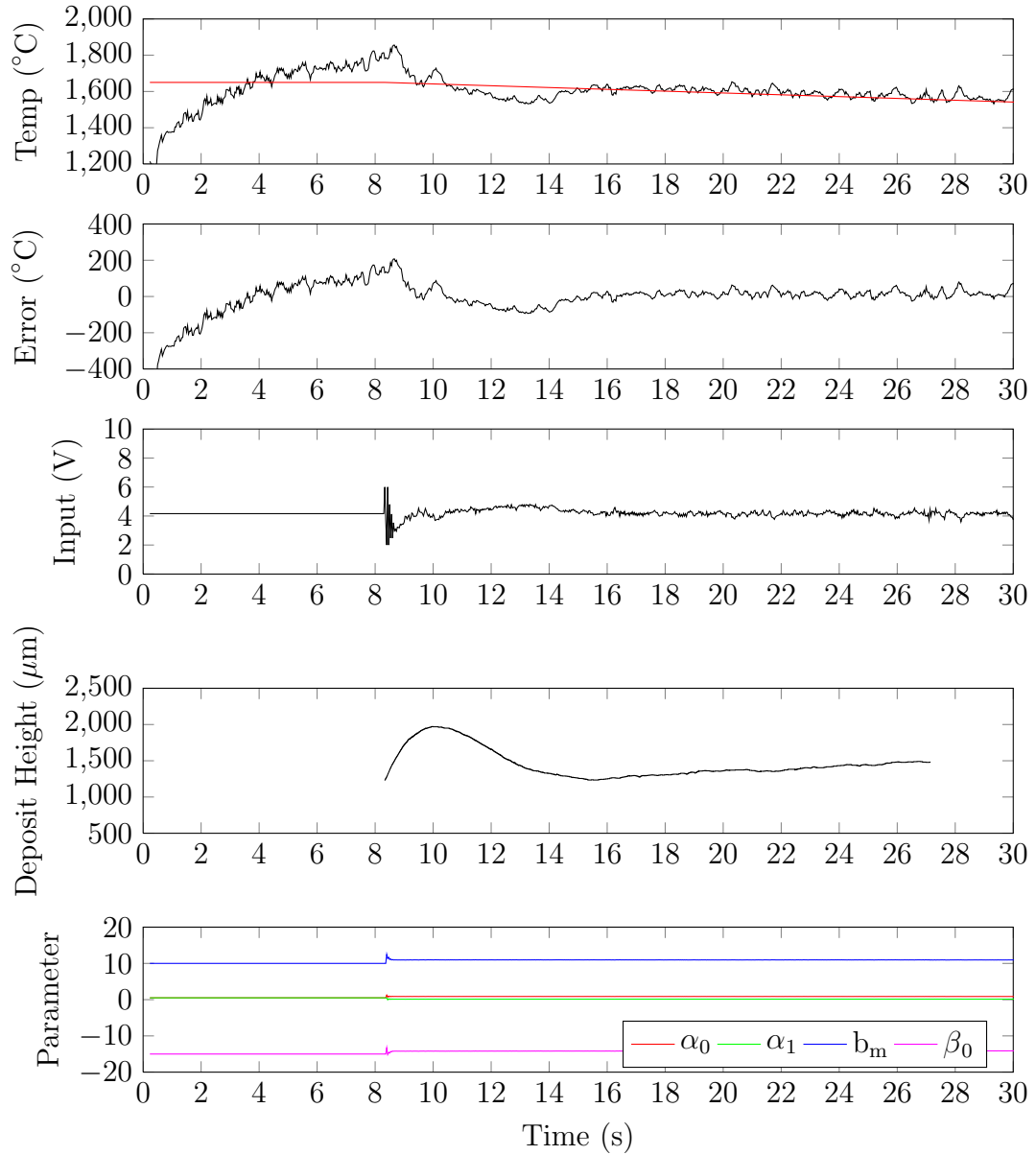
Figure 127: Measured temperature profile for a trial with a ramp down from 1650 °C to 1500 °C reference temperature. Average error of 8.73 °C.

does indeed result in an increase in the deposit height. Again clearly demonstrating that it it possible to control microstructural features through the use of temperature feedback. The change in deposit height could be used to account for variations in the previous layer height when implementing multi-layer capabilities.

The results of the adaptive control trials demonstrate that the deposit height
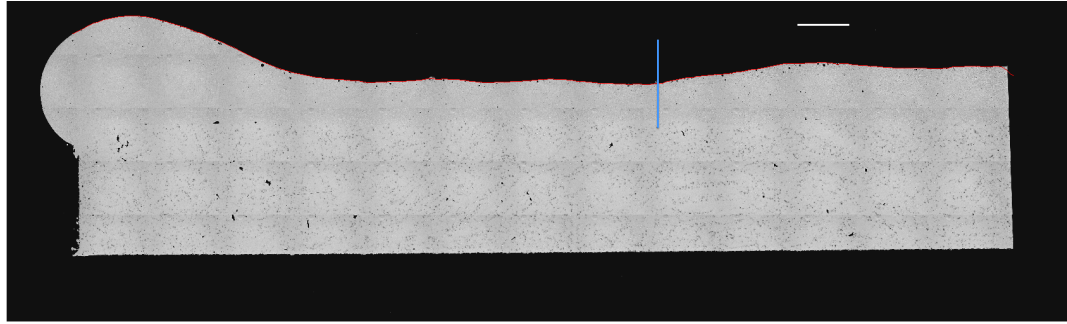
Figure 128: Micrograph of a sample run with a step up from 1600 to 1700 $°C$ in reference temperature in the second half. The location of the step up in temperature is indicated by the red line. Scale bar of 1mm length.

can be controlled using temperature feedback control. In spite of the deposit non-uniformity caused by the smoke extraction system in open loop trials, the adaptive control trials were able to appropriately control the temperature during processing to compensate and produce uniform deposits without significantly altering the average laser input power over those used in the open loop trials in Chapter 4. This result was due to the controller compensating for drops in melt pool temperature before they resulted in an instability at the melt front. Typically once there is a single occurrence of instability during processing, the powder begins falling into the melt pool cyclically pulling in excess powder and then starving itself until the run is over. Avoiding the first occurrence of this instability causes the deposit uniformity to be greatly enhanced.

The offline model used to predict the microstructure of CMSX-4 deposits is still currently being worked on by other members of the research group. With this in mind, it remains to be determined whether following a reference temperature will also similarly impact the dendrite formation in CMSX-4 samples. These initial results in feedback control of the process running on René-80 are certainly promising though and it is clear that feedback control of this nature will be required when moving the process towards multi-layer capability on any material.
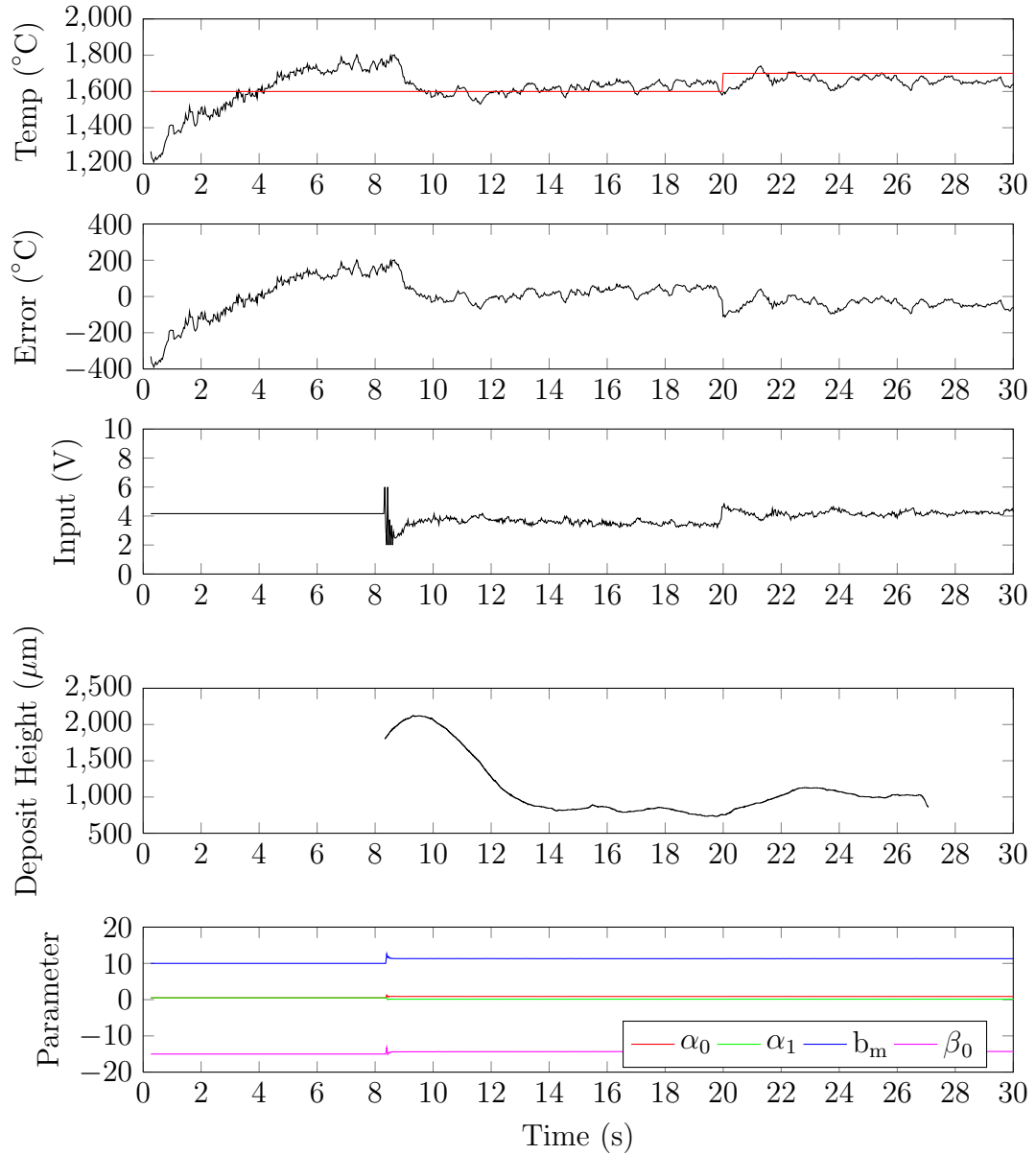
Figure 129: Measured temperature profile for a trial with a step from 1600 $°C$ to 1700 $°C$ reference temperature. Average error of -16.66 $°C$. Deposit height increases by over $300\mu m$ after the step up in reference temperature.

5.5 Controller Parameter Tuning Procedure

Development of SLE processing parameters for new alloys and geometries is currently a time consuming and difficult procedure. An overview of the process parameter development flow chart with the approximate number of samples used is shown in Figure 130. In open loop control, many trials are required to be run to determine a feasible
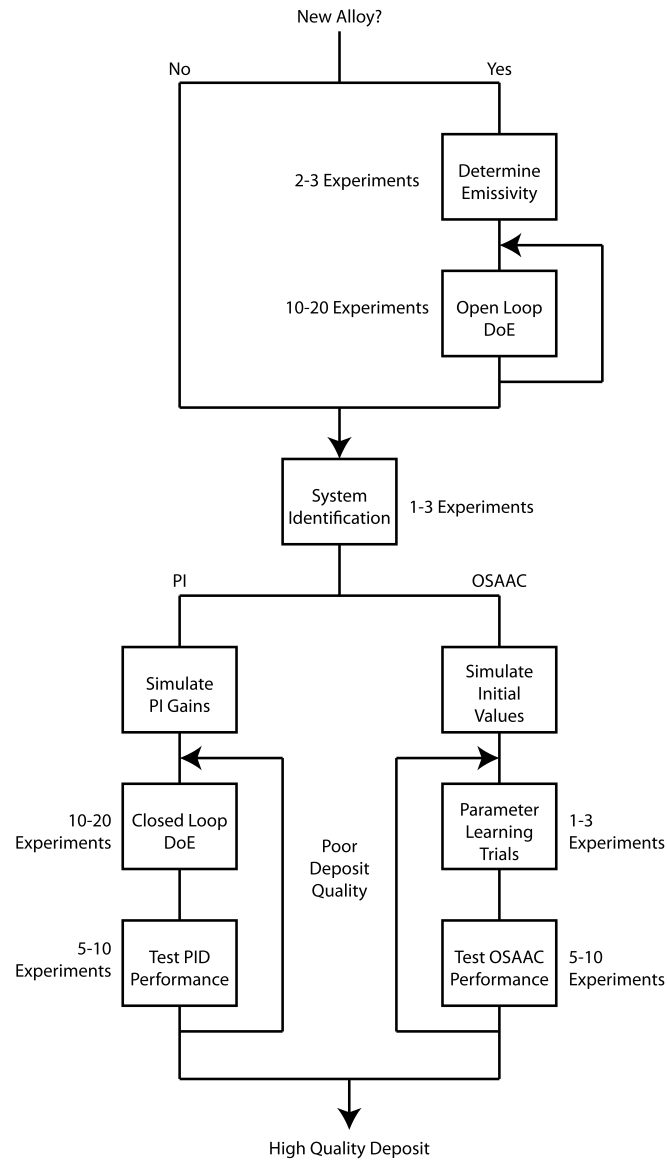
Figure 130: Flow chart overview of process parameter development for utilizing SLE on a new alloy or geometry. Approximate numbers of experiments required for each step are also listed.

range of parameters. There are two steps in determining open loop parameters, first, a set of initial feasibility trials are run to determine a feasible operating range. A set of DoEs can then be run to drill down on the proper parameter set that produces the highest quality open loop deposits. The number of open loop DoEs required to produce well formed deposits will likely be reduced or eliminated entirely once the robust multiphysics model is completed and able to predict the parameters required

to produce well formed deposits on a new alloy.

Control parameter development occurs after the open loop development and follows two different procedures for the PI and OSAAC schemes. Because of the relatively poor performance of the PI controller and difficulty choosing gain values, development of the PI gains leading to a high performance controller will require several iterations of a closed loop DoE. In these DoEs, the gains, K_i and K_p, are the factors and controller parameters such as response time, settling time, and average error are the responses to optimize. Optimizing the PI controller parameters could take upwards of 30 experiments. Development of controller parameters for the OSAAC control scheme uses fewer experiments because the parameter learning algorithm can quickly converge towards the proper process parameters over the course of only a few trials when the system is sufficiently excited by a varying laser power. These learning trials can be done by either reducing the weighting penalty, λ, on the prior control input, increasing the adaptive gains, γ, or providing a highly varying input reference temperature, such as a sine wave, to the system. Additionally, performance of the OSAAC was generally better than the PI controller and thus it is relatively easier to track a desired melt temperature with the OSAAC scheme and produce high quality deposits using this scheme. This parameter tuning procedure will be required whenever a major change in alloy or part geometry occurs. The robustness of the adaptive control scheme will allow it to operate properly when similar alloys, in terms of melt temperature and flow characteristics, are used or only small changes in geometry are made, but control performance will degrade unless the learning trials are run again.

5.6 Summary

This chapter described the development of real-time feedback control for the SLE process. Implementation of two machine vision algorithms to detect the average melt pool temperature through the use of a thermal camera was first discussed. It was

found that a connected component labeling algorithm was able to quickly locate the size and shape of the melt pool and calculate the average melt pool temperature without any loss in camera frame rate due to processing time. Using this temperature feedback data, system identification experiments were performed to determine a transfer function model for the system. A second order transfer function was developed and used to successfully simulate and implement a PI controller to control the melt pool temperature during processing by varying the input laser power. It was found that an excessive number of experiments would be required to properly tune the gains of the PI controller for each alloy being processed, so an adaptive control scheme was implemented to quickly determine controller parameters. The adaptive controller was used to demonstrate that following a reference temperature profile had a significant effect on the resulting deposit height produced on René-80 alloy samples via SLE. It was found that constant reference temperature profiles produced the most uniform samples produced to date, significantly improving the process over the open loop trials run previously and potentially enabling the process to be used for multi-layer deposition in the future. The chapter concludes with a discussion of the process parameter selection process for SLE development on new alloys and geometries.

CHAPTER VI

CONCLUSIONS

This chapter summarizes the work done to date on the development of the SLE process. The chapter begins with a listing of several conclusions taken from this work. It then highlights the unique contributions of this dissertation and finally suggests some potential avenues for future research in this area.

6.1   Summary

The SLE process developed as part of this work has been investigated for its use on repair of Ni-superalloy turbine engine hot-section components and construction of fully-dense, crack-free multilayer three-dimensional objects. The SLE process is a new layer-by-layer additive manufacturing process that creates deposits through the controlled melting and re-solidification of metal powders placed on like-material base substrates. In this dissertation, a detailed discussion of the experimental setup enabling the SLE process is first discussed. Included in this discussion is how this particular setup and process advances the current state-of-the-art in turbine engine component repair by implementing a high speed galvanometer laser scanner and a pre-placed powder bed of material to allow for tight control of temperature gradients during processing. The operation of SLE on several different Ni-superalloy materials is then explored, beginning with Mar-M247, then moving to the SX alloy CMSX-4 and finally looking at the crack-prone René-80 alloy. A set of process maps defining the parameter ranges in which high quality deposits of CMSX-4 and René-80 are developed. It is found that although the results of these open loop trials are promising and demonstrate the capabilities of the SLE process to create high quality deposits out of these materials, the process is somewhat encumbered by a lack of repeatability

160

and difficulty associated with determining optimal processing parameter maps. To overcome these issues, real-time feedback control based upon thermal camera temperature data of the melt pool during processing is developed. Several challenges associated with the use of a thermal camera are first addressed. The first challenge was measuring a proper emissivity value for the material in question. The second challenge was developing a machine vision algorithm to detect the melt pool location and temperature. After addressing the issues with utilizing a thermal camera to collect temperature data, two control schemes are explored, PID and OSAAC. The closed-loop trials are shown to improve the process over the open-loop trials.

6.2   Conclusions

1. Trials on Mar-M247 demonstrated that fully dense deposits were achievable, metallurgical bonds were formed between the melt and base substrate and hot tearing, or stress cracking was not evident, even after post-process heat treatment. These trials also found that powder containment would be required to make the SLE process more predictable and repeatable and high power/low scan speeds (high energy density) yielded significant warping of the base substrate while low power/high scan speeds (low energy density) resulted in low melt back, indicating that a trade off would need to be made between having sufficient melt back and limiting substrate warping. Volumetric energy densities on the order of $50 J/mm^3$ were found to result in high quality Mar-M247 deposits.

2. The CMSX-4 trials demonstrated that the deposition of material with full fusion and minimal melt back of below 500 microns, as well as significant columnar growth of approximately 1000 microns was possible. Additionally, the average columnar to total height ratio of greater than 50% across the deposit length could be produced. Powder containment around the top of the substrate also

allowed for columnar growth of greater than 1000 microns from edge to edge across the width of the sample. The developed process maps show that lower powder thickness with higher energy density resulting in volumetric energy densities on the order of $100J/mm^3$ led to the most promising samples. Low energy density led to a lack of fusion along the length of the sample. High energy density led to stray grain formation and lower overall columnar to total deposit height ratio.

3. Trials on René-80 showed that the SLE process was capable of creating crack-free deposits on alloys commonly referred to as "non-weldable". There was no evidence of cracking in any of the René-80 samples produced, even after heat treatment, indicating the the SLE process was able to produce deposits that were not susceptible to strain-age cracking. The René-80 process maps show that laser power most significantly impacts the deposit height and melt depth and tends to significantly increase each of these values as it increases. Scan speed most significantly impacts the melt depth and causes it to decrease as the scan speed increases. The number of repeat scans have a significant impact on the deposit uniformity and melt depth, increasing both as the repeat scans increase. The most promising process parameters for developing René-80 samples were around approximately $80J/mm^2$.

4. Two approaches were used to estimate emissivity values for the René-80 material. An emissivity-correcting pyrometer was used to measure the temperature of a heated sample at the same time as the thermal imaging camera. This resulted in emissivity values of between 0.35 and 0.40 for the temperature range between $1000°C$ and $1200°C$ when viewing through the thermal imaging camera. The emissivity-correcting pyrometer was unable to measure the emissivity

properly at or above the melting point of the material due to meniscus formation. A second method comparing the location of the plateau in temperature observed when heating a material through its melting temperature was used to determine the emissivity value of 0.52 at the solidus temperature of René-80. This small increase in emissivity when the material begins melting is due to the change in geometry of the melt pool and slight oxidation during melting.

5. Two machine vision algorithms were implemented to determine the size, shape and average temperature of the melt pool detected by the thermal imaging camera. The Canny edge detection algorithm was found to operate in 100-150 ms and significantly impacted the frame rate of the thermal imaging camera. The second algorithm, a connected component labeling algorithm, was able to operate on the order of 5-10 ms and did not alter the frame rate of the thermal camera.

6. Lumped capacitance modeling and system identification showed that the melt pool temperature during SLE processing could be related to the input laser power by a second order transfer function.

7. The second order transfer function was used as the basis for two control schemes. The PI controller with gains developed using simulation of the identified transfer function was able to control the melt temperature, but performance was poor with settling times of about 10-12s. A significant number of expensive trials would be required to optimize the PI gains to achieve more optimal results. The OSAAC was shown to achieve much faster settling times on the order of 2-4s with significantly fewer required trials than the PI controller. Additionally, the average error found when using the OSAAC scheme was lower than when using the PID scheme. Average errors on the order of $< 10°C$ were found when using the OSAAC scheme.

8. Application of several different frequency laser power input signals demonstrated that 30Hz was the highest frequency signal that could alter the deposits resulting from the SLE process. Frequencies at 30Hz or higher resulted in deposits that would have been produced at the average value of the laser power signal.

9. Closed-loop feedback control of the melt pool temperature was found to significantly alter the deposit height of produced deposits. Uniform temperature profiles led to the most uniform deposits produced amongst all open loop and closed loop trials to date. Additionally, applying step inputs or other variations to the melt pool temperature demonstrated that deposit height could be controlled and altered during processing, potentially enabling correction for non-uniform deposit heights in previous layers when doing multi-layer processing.

6.3   Unique Contributions

1. Developed the hardware and software required to initially implement the SLE process and demonstrate its use on Ni-superalloys. The SLE process is capable of producing higher quality single crystal repair deposits than any prior process and is also capable of working with previously thought to be "non-weldable" materials.

2. Demonstrated the capability of the SLE process to produce specified SX microstructure on materials such as CMSX-4 and developed process maps illustrating the parameter ranges under which high quality SX deposits are formed.

3. Demonstrated the capability of using the SLE process to produce fully dense crack-free deposits on the traditionally "non-weldable" alloy René-80. Process maps were also developed for René-80 showing process parameter areas that

resulted in high uniformity, low melt-back deposits.

4. Developed a process for measuring the high temperature emissivity of metal alloys both through the use of an emissivity-correcting pyrometer and matching of melt temperature profile with the known melt temperature of a material. This process was used to develop curves for the emissivity as a function of temperature for an alloy, René-80, that had not yet been explored in literature. The same procedure can be used to determine emissivity data for other high-temperature alloys.

5. Developed machine vision techniques to analyze thermal imaging data and to measure melt pool shape, size, and temperature for analysis of and real-time control of powder-based additive manufacturing processes.

6. Expanded the reach of additive manufacturing processes by being one of the first to implement real-time feedback control in an integral way. The feedback control system was shown to improve the SLE process considerably over the open loop process.

6.4   Suggestions for Future Work

1. The trials run on CMSX-4 did not include experiments run below 1mm powder height due to issues of creating a uniform amount of powder below this height without a proper layering system in place. These additional trials should be run when developing a multi-layer system to determine a lower bound on the resulting process maps.

2. Trials on René-80 above 600W input laser power were not run due to potential for damaging of the galvonometer laser scanner mirrors. This resulted in an unbounded location on the process maps above this laser power. Additional

verification of René-80 process maps for laser powers higher than 600W would complete this process map.

3. Use of the control scheme with temperature profiles actually developed by a detailed offline model was not explored due to the aforementioned model not being completed before presentation of this work. An exploration of how tracking a modeled temperature profile rather than simple profiles such as constant, step or ramp inputs would provide key insights into what new types of homogeneous or heterogeneous microstructural features could be developed using real-time control.

4. Current limitations on the lower bound operating temperature of the thermal imaging camera prevented precise control of input laser power during melt pool initiation repeat scans. If a thermal camera with a lower operating temperature was used, different repeat scan schemes could be developed to initiate the melt pool while also limiting the amount of balling seen at the starting edge of samples. Additional data such as looking at the eccentricity and size of the melt pool at the starting edge could also be used to determine the exact moment that wetting of the substrate occurs.

5. One of the limitations of the thermal camera data used in this work is the assumption of a fixed emissivity value that was set at the melting point of the alloy in question. Determination of emissivity data for temperatures above the melting point of each alloy will make the temperature data more accurate. Emissivity determination during processing could also be achieved by focusing the emissivity-correcting pyrometer through the laser scanner such that it is always measuring the emissivity value of the melt pool. This was the original approach followed in this work but it was not accomplished due to difficulties in setting up the proper optical path.

6. The current melt pool detection algorithm performs poorly at low laser input power due to inadvertent detection of molten balls of powder collecting in front of the melt pool from melt instability. The detection of these molten balls causes additional noise in the signal that may be reduced through other algorithms such as an active contouring algorithm that could detect and reject these molten balls of powder. Implementation of such an algorithm may expand the operating range of the laser power but care must be taken to ensure that the the algorithm computes fast enough to not limit the sampling rate of the thermal camera.

7. The control schemes implemented as part of this dissertation are the initial foray into the area of feedback control of additive manufacturing processes. Many more complex and robust control schemes could be explored to further improve controller performance and increase the robustness of the process. Additionally, the control schemes in this dissertation were both SISO schemes, only controlling the melt pool temperature through adjustment of laser power. The first more advanced scheme to explore should be a MIMO scheme including control of both laser power and melt pool geometry by adjusting both input laser power and scan speed. Both of these inputs have an effect on each of the outputs and implementing all temperature profiles developed by an offline model will require simultaneous control of both parameters.

8. The end goal control scheme would be a distributed parameter control (DPC) scheme that drives the entire temperature field during processing towards a desired temperature field developed by the offline model. Comparing a large-scale distributed temperature map to an ideal temperature map and implementing feedback control based upon that feedback will allow for much tighter control of the temperature gradients present during the laser processing. Initially this was the scheme that was being worked towards before it was determined that

even developing simpler algorithms to introduce real-time control to the SLE process would pose a significant challenge on their own. Nevertheless, some initial work has been done on developing an output observer for use in a DPC scheme. This work in presented in the Appendix A and could be utilized by a future researcher in this area.

APPENDIX A

OUTPUT OBSERVER DEVELOPMENT

Although it did not end up being used in the currently implemented control schemes, a Green's function model was used to develop an online observer to estimate the substrate temperature of a location just below or near the melt pool for use in more advanced control schemes such as a distributed parameter control scheme. Green's function analysis was used to calculate a lookup table for determining the temperature profile generated in response to beam location. The lookup table developed using this analysis would allow for quick estimation of substrate temperature during online SLE processing by allowing for convolution of the values in the lookup table to determine the temperature distribution caused as a result of past laser beam locations and powers.

Early analysis of the temperature fields produced in welding processes were based upon Rosenthal's solution for a heat source moving on a semi infinite plate. Eagar and Tsai formulated a Green's function approach to the problem in the early 1980s [72, 73]. A similar analysis as it pertains to SLE is presented here.

Although a 3D analysis will be needed for constructing a full lookup table for complex geometries, for the purposes of an initial study and proof of concept, a 2D model was analyzed. Due to the extremely high scan speed, v_r, of the laser beam, it was assumed to be equal to a line source of heat input on the top of the rectangular substrate. The rectangular block substrate was then modeled as a two-dimensional rectangle. The incident laser beam was modeled as a Gaussian distributed heat source that moved across the top of the substrate with a line speed, v_l. Convective boundary conditions were used on all boundaries, as this was most representative of the actual

experimental setup. A graphical representation of the problem is shown in Figure
131.
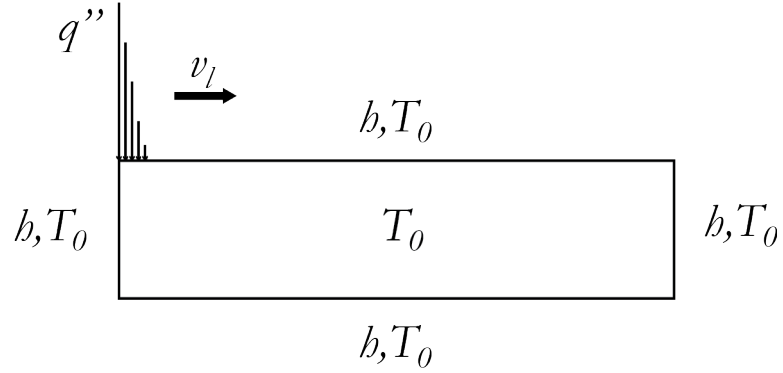
Figure 131: Two dimensional representation of the scanning laser epitaxy problem.

The Green's function for a heat conduction problem represents the temperature
at a particular location and time, $T(x, y, t)$, due to an instantaneous line source of
unit strength located at (x', y') and time τ. The Green's function for this problem
is found by utilizing a product of the finite extent Green's functions in the x and y
directions for convective boundary conditions on both sides and is shown in Equation
60 [74].

$$
G\left(x, y, \theta | x', y', \tau\right) = \left[\sum_{n=1}^{\infty} e^{\alpha \beta_n^2 (t-\tau)} \frac{1}{N\left(\beta_n\right)} X\left(\beta_n, x\right) X\left(\beta_n, x'\right)\right]
$$
$$
\left[\sum_{m=1}^{\infty} e^{\alpha \beta_m^2 (t-\tau)} \frac{1}{N\left(\beta_m\right)} Y\left(\beta_m, y\right) Y\left(\beta_m, y'\right)\right] \quad (60)
$$

Where:

$$\alpha = \frac{k}{\rho c} \tag{61}$$

$$H = \frac{h}{k} \tag{62}$$

$$X(\beta_n, x) = \beta_n cos(\beta_n x) + H sin(\beta_n x) \tag{63}$$

$$N(\beta_n) = \frac{1}{2}\left[(\beta_n^2 + H^2)\left(L_x + \frac{H}{\beta_n^2 + H^2}\right) + H\right] \tag{64}$$

$$Y(\beta_m, x) = \beta_m cos(\beta_m y) + H sin(\beta_m y) \tag{65}$$

$$N(\beta_m) = \frac{1}{2}\left[(\beta_m^2 + H^2)\left(L_y + \frac{H}{\beta_m^2 + H^2}\right) + H\right] \tag{66}$$

The eigenvalues β_n and β_m are the positive roots of:

$$tan(\beta_n L_x) = \frac{2H\beta_n}{\beta_n^2 - H^2} \tag{67}$$

$$tan(\beta_m L_y) = \frac{2H\beta_m}{\beta_m^2 - H^2} \tag{68}$$

The temperature distribution is then found by integrating the Green's functions as follows:

$$U(x, y, \theta) = \int_A G(x, y, \theta | x', y', \tau)|_{\theta=0} F(x', y') \, dA' d\tau$$

$$+ \frac{\alpha}{k} \int_{\tau=0}^\theta \int_A G(x, y, \theta | x', y', \tau) g(x', y', \theta) \, dA' d\tau$$

$$+ \frac{\alpha}{k} \int_{\tau=0}^\theta \sum_{i=1}^N \int_C G(x, y, \theta | x', y', \tau)|_{r'=r_i} f_i dl_i d\tau \tag{69}$$

The initial temperature distribution, $F(x', y')$, is zero due to the normalization in this particular formulation of the problem. The heat generation, $g(x', y', \theta)$, is also zero in this case. Likewise, all of the boundary heat flux terms, f_i, are also zero except for the heat flux from the gaussian beam on the top surface. Using these simplifications and substituting back in $t(x, y, \theta) = u(x, y, \theta) + T_0$, the temperature distribution is found to be:

$$T(x, y, \theta) = \frac{\alpha}{k} \int_{\tau=0}^{\theta} \int_{x'=0}^{L_x} G(x, y, \theta | x', y', \tau)|_{y'=0} q''(x', \tau) \, dx' d\tau + T_0 \qquad (70)$$

This solution to the problem is particularly powerful because it represents the solution for this geometry for a heat source of arbitrary spatially and temporally varying power. This solution can thus give the temperature profile for an arbitrarily shaped and moved input laser beam through the use of integration or convolution. In this particular case, the heat input from the Gaussian distributed beam was taken as:

$$q''(x', \tau) = \frac{P(\tau)}{\sigma\sqrt{2\pi}} e^{-\frac{1}{2}\left(\frac{x'-v_l\tau}{\sigma}\right)^2} \qquad (71)$$

$P(\tau)$ is the time varying amplitude of the Gaussian distribution chosen so that its total area represents the total incident laser power at each instant in time. σ is the standard deviation of the Gaussian chosen such that the distribution represents a beam of the chosen radius. The $v_l\tau$ term causes the beam to move across the substrate at the line speed.

To assess it's validity, this analytical solution was analyzed in MATLAB and compared to an FEM analysis in the software package COMSOL. For the purposes of both this MATLAB simulation and the following COMSOL simulation, the parameters for CMSX-4 processed in air shown in Table 11 were used.

Table 11: Simulation Parameters for CMSX-4 in Air [28]

Parameter	Value	Units
k	28.45	$W/(m \cdot K)$
ρ	8700	kg/m^3
c	815.88	$J/(kg \cdot K)$
h	5	$W/(m^2 K)$
L_x	0.018	m
L_y	0.003	m
v_l	0.0002	m/s

One comparison case between the analytical and FEM response is shown in the plots in Figure 132. This set of simulations was run with a constant power intensity as the Gaussian beam moved across the substrate at a line speed of $v_l = 1.8mm/sec$.
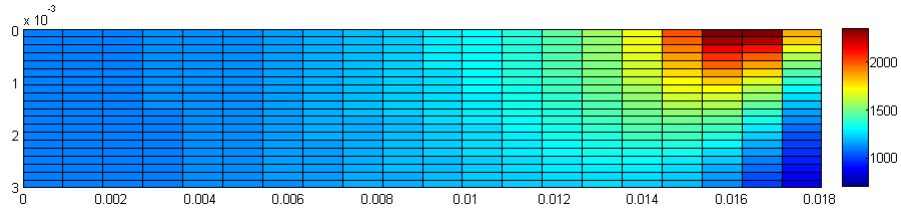
(a) Analytical Simulation
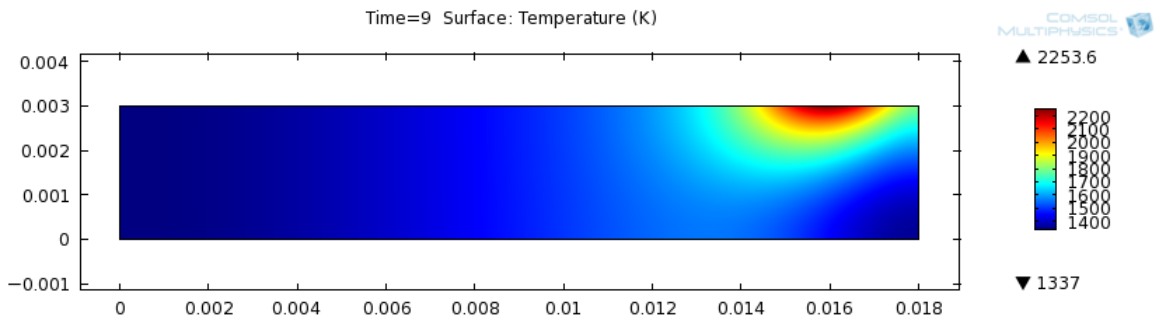
(b) COMSOL Simulation

Figure 132: Temperature distributions for simulations run with 350W absorbed constant power Gaussian beam at moving at $v_l = 1.8mm/sec$ at $\theta = 9sec$.

It can be noted that the analytical and FEM analysis lines up well, though a comparison between the analytical and the experimental responses remains to be tested.

APPENDIX B

PROCESS MAP FIT MODEL DETAILS

Several fit models relating various processing parameters to the resulting deposit quality metrics studied in this work. These fit maps were produced using the statistical analysis software package, JMP 10. The resulting models were then used to plot processing maps for each of the alloys studied in this dissertation. A detailed analysis relating the predicted value of each fit model to the actual experimental values is listed in this appendix for each model that was developed. The p-value represents the likelihood that a measured value would have been observed in the absence of variation of the considered process parameters. The p-value helps to indicate the level of statistical significance of each model. P-values below 0.05 or 5% indicate that the observed result would be highly unlikely if the process parameters considered were not varied, indicating that it may be a statistically significant model. The prediction expressions for each fit model that were used to plot the process maps are also listed.

B.1 CMSX-4 Fit Models
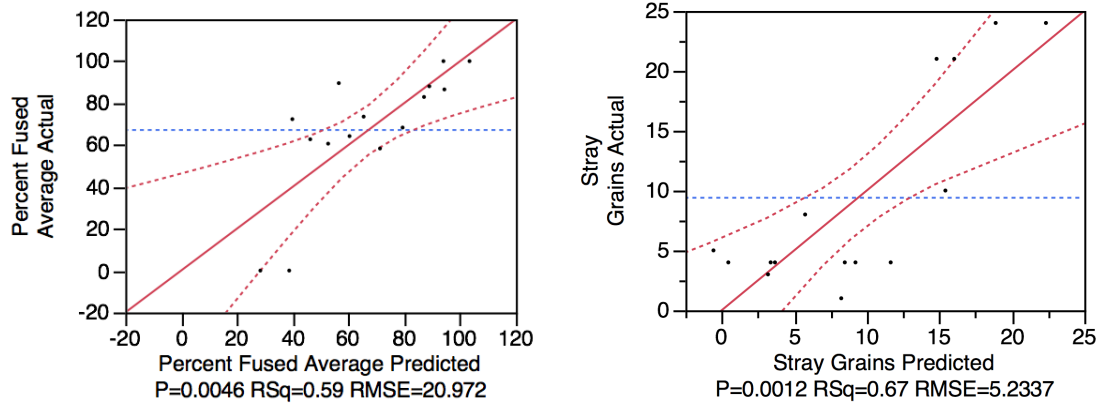
(a) Analysis of the fit model relating the percent fused to powder height and energy density. $68.5 - 60.6 * Powder(mm) + 0.858 * Energy(J/mm^2)$

(b) Analysis of the fit model relating the stray grain count to powder height and energy density. $-52.1 + 8.76 * Powder(mm) + 0.463 * Energy(J/mm^2)$
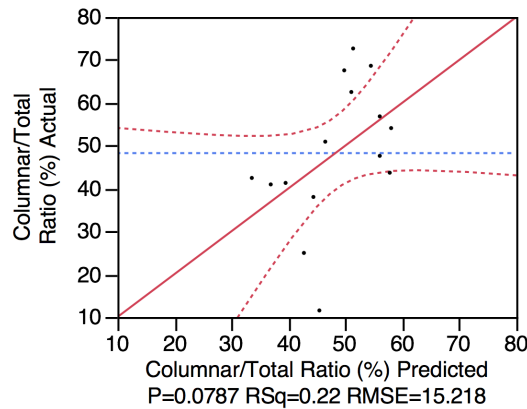
(c) Analysis of the fit model relating the CTR to energy density. $131 - 0.792 * Energy(J/mm^2)$

Figure 133: Plots showing predicted vs actual values for each fit model developed. Black dots indicate data points, the red line indicates the model, the red dotted line is the 0.05 significance interval, and the blue line indicates the mean value. The prediction expressions are also listed in the captions.

As can be seen from the P values well below 5% and the R^2 values around 0.6, the predicted values of fused percent and stray grain count were significant. The model

175

for CTR was not quite as good and had a P value of 7.9%. Running more experiments at a lower powder thickness could increase the statistical significance of this particular fit model. These trials were not run due to the absence a layering system that could properly meter powder thicknesses below 1mm in height.

B.2 René-80 Fit Models
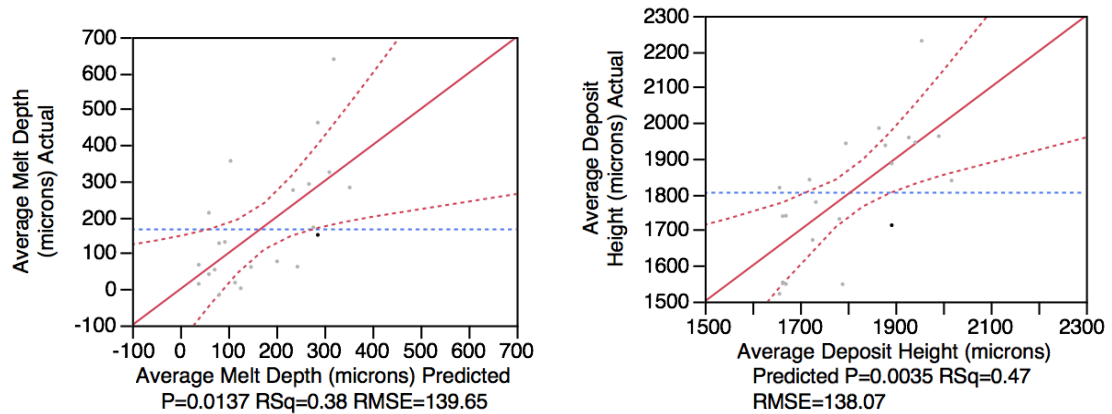
(a) Analysis of the fit model relating the average melt depth to laser power and repeat scans.
$-2.87 + 0.663 * Power(W) - 0.423 * Repeats$

(b) Analysis of the fit model relating the average deposit height to laser power and repeat scans.
$1280 + 1.26 * Power(W) - 0.134 * Repeats$
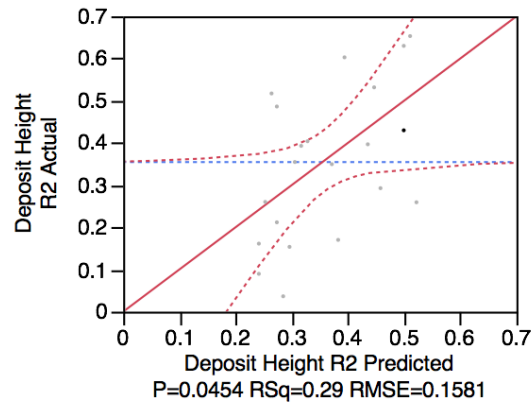
(c) Analysis of the fit model relating the deposit height uniformity to laser power and repeat scans. $0.451 + 0.000226 * Power(W) - 0.000640 * Repeats$

Figure 134: Plots showing predicted vs actual values for each fit model developed. Black dots indicate data points, the red line indicates the model, the red dotted line is the 0.05 significance interval, and the blue line indicates the mean value. All of the fit models here were determined to be significant. The prediction expressions are also listed in the captions.
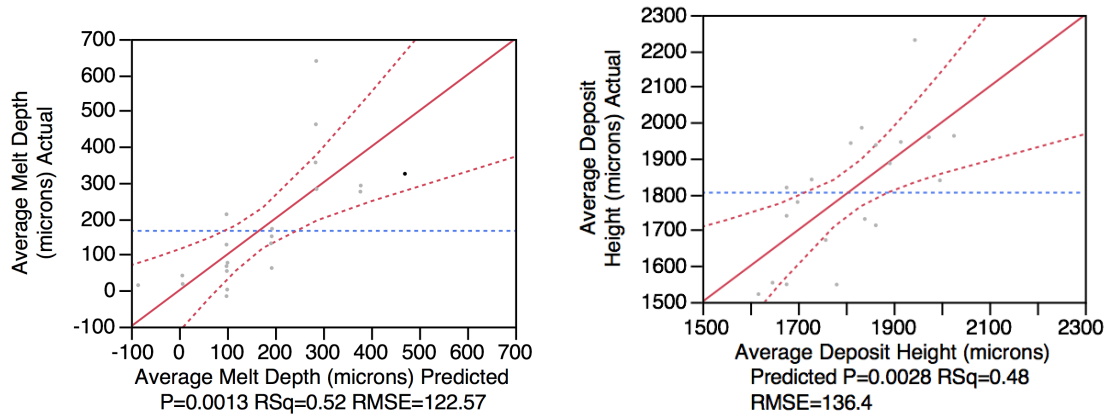
177

(a) Analysis of the fit model relating the average melt depth to laser power and scan speed. $278 + 1.85 * Power(W) - 1.84 * Speed(mm/s)$

(b) Analysis of the fit model relating the average deposit height to laser power and scan speed. $1370 + 1.64 * Power(W) - 0.588 * Speed(mm/s)$
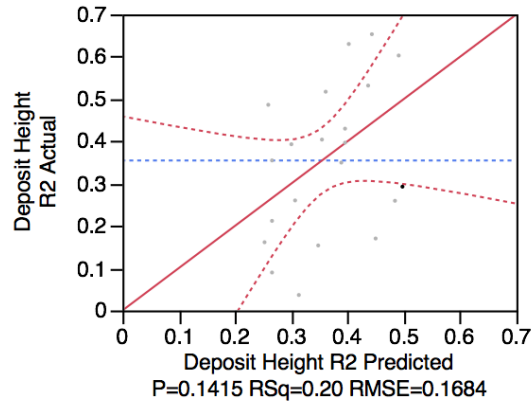
(c) Analysis of the fit model relating the deposit height uniformity to laser power and scan speed. $-0.00824 + 0.000954 * Power(W) - 0.000133 * Speed(mm/s)$

Figure 135: Plots showing predicted vs actual values for each fit model developed. Black dots indicate data points, the red line indicates the model, the red dotted line is the 0.05 significance interval, and the blue line indicates the mean value. The fit models for melt depth and deposit height were significant. The model for deposit uniformity was not as significant but still indicated the general trend. The prediction expressions are also listed in the captions.

REFERENCES

[1] NICKEL, A., BARNETT, D., and PRINZ, F., "Thermal stresses and deposition patterns in layered manufacturing," *Materials Science and Engineering: A*, vol. 317, no. 1, pp. 59–64, 2001.

[2] KRUTH, J., FROYEN, L., VAN VAERENBERGH, J., MERCELIS, P., ROMBOUTS, M., and LAUWERS, B., "Selective laser melting of iron-based powder," *Journal of Materials Processing Technology*, vol. 149, no. 1, pp. 616–622, 2004.

[3] MORRIS, G., "Direct metal laser sintering." Presented, October 2009.

[4] GAUMANN, M., *Epitaxial Laser Metal Forming of a Single Crystal Superalloy.* PhD thesis, École Polytechnique Fédérale De Lausanne, 1999.

[5] GLAVICIC, M., "The repair of single crystal nickel superalloy turbine blades using laser engineered net shape (lens) technology," tech. rep., DTIC Document, 2003.

[6] MOKADEM, S., *Epitaxial laser treatment of single crystal nickel-base superalloys.* PhD thesis, École Polytechnique Fédérale De Lausanne, 2004.

[7] BABU, S., DAVID, S., PARK, J., and VITEK, J., "Joining of nickel base superalloy single crystals," *Science and Technology of Welding &# 38; Joining*, vol. 9, no. 1, pp. 1–12, 2004.

[8] PARK, J., BABU, S., VITEK, J., KENIK, E., and DAVID, S., "Stray grain formation in single crystal ni-base superalloy welds," *Journal of applied physics*, vol. 94, p. 4203, 2003.

[9] YOUNOSSI, O., ARENA, M., MOORE, R., LORELL, M., and MASON, J., "Military jet engine acquisition: Technology basics and cost-estimating methodology," tech. rep., DTIC Document, 2002.

[10] SPITTLE, P., "Gas turbine technology," *Physics education*, vol. 38, no. 6, p. 504, 2003.

[11] GOULETTE, M., "The future costs less high temperature materials from an aeroengine perspective," 1997.

[12] REED, R., *The superalloys: fundamentals and applications.* Cambridge Univ Pr, 2006.

[13] QUESTED, P., BROOKS, R., CHAPMAN, L., MORRELL, R., YOUSSEF, Y., and MILLS, K., "Measurement and estimation of thermophysical properties of nickel based superalloys," *Materials Science and Technology*, vol. 25, no. 2, pp. 154–162, 2009.

[14] DECKER, R. and MIHALISIN, J., "Coherency strains in gamma prime hardened nickel alloys," *ASM Transactions Quarterly*, vol. 62, no. 2, pp. 481–489, 1969.

[15] TAKEUCHI, S. and KURAMOTO, E., "Temperature and orientation dependence of the yield stress in ni_3ga single crystals," *Acta metallurgica*, vol. 21, no. 4, pp. 415–425, 1973.

[16] YOO, M., "On the theory of anomalous yield behavior of ni_3al–effect of elastic anisotropy," *Scripta metallurgica*, vol. 20, no. 6, pp. 915–920, 1986.

[17] CIESLAK, M., HEADLEY, T., and ROMIG, A., "The welding metallurgy of hastelloy alloys c-4, c-22, and c-276," *Metallurgical and Materials Transactions A*, vol. 17, no. 11, pp. 2035–2047, 1986.

[18] CIESLAK, M., "The welding and solidification metallurgy of alloy 625," *Welding journal*, vol. 70, no. 2, pp. 49s–56s, 1991.

[19] DUPONT, J., MICHAEL, J., and NEWBURY, B., "Welding metallurgy of alloy hr-160," tech. rep., Sandia National Laboratories (SNL), Albuquerque, NM, and Livermore, CA, 1999.

[20] DUPONT, J., LIPPOLD, J., and KISER, S., *Welding metallurgy and weldability of nickel-base alloys.* Wiley, 2011.

[21] HENDERSON, M., ARRELL, D., LARSSON, R., HEOBEL, M., and MARCHANT, G., "Nickel based superalloy welding practices for industrial gas turbine applications," *Science and Technology of Welding &# 38; Joining*, vol. 9, no. 1, pp. 13–21, 2004.

[22] DYE, D., HUNZIKER, O., ROBERTS, S., and REED, R., "Modeling of the mechanical effects induced by the tungsten inert-gas welding of the in718 superalloy," *Metallurgical and Materials Transactions A*, vol. 32, no. 7, pp. 1713–1725, 2001.

[23] ANDERSON, T., DUPONT, J., and DEBROY, T., "Stray grain formation in welds of single-crystal ni-base superalloy cmsx-4," *Metallurgical and Materials Transactions A*, vol. 41, no. 1, pp. 181–193, 2010.

[24] OJO, O. and CHATURVEDI, M., "On the role of liquated γ precipitates in weld heat affected zone microfissuring of a nickel-based superalloy," *Materials Science and Engineering: A*, vol. 403, no. 1, pp. 77–86, 2005.

[25] IDOWU, O., OJO, O., and CHATURVEDI, M., "Effect of heat input on heat affected zone cracking in laser welded ati allvac 718plus superalloy," *Materials Science and Engineering: A*, vol. 454, pp. 389–397, 2007.

[26] RAPPAZ, M., DAVID, S., VITEK, J., and BOATNER, L., "Development of microstructures in fe- 15ni- 15cr single crystal electron beam welds," *Metallurgical and Materials Transactions A*, vol. 20, no. 6, pp. 1125–1138, 1989.

[27] RAPPAZ, M., DAVID, S., VITEK, J., and BOATNER, L., "Analysis of solidification microstructures in fe-ni-cr single-crystal welds," *Metallurgical and Materials Transactions A*, vol. 21, no. 6, pp. 1767–1782, 1990.

[28] ANDERSON, T., DUPONT, J., and DEBROY, T., "Origin of stray grain formation in single-crystal superalloy weld pools from heat transfer and fluid flow modeling," *Acta Materialia*, vol. 58, no. 4, pp. 1441–1454, 2010.

[29] LIU, W. and DUPONT, J., "Effects of melt-pool geometry on crystal growth and microstructure development in laser surface-melted superalloy single crystals: Mathematical modeling of single-crystal growth in a melt pool (part i)," *Acta materialia*, vol. 52, no. 16, pp. 4833–4847, 2004.

[30] LIU, W. and DUPONT, J., "Effects of substrate crystallographic orientations on crystal growth and microstructure development in laser surface-melted superalloy single crystals. mathematical modeling of single-crystal growth in a melt pool (part ii)," *Acta materialia*, vol. 53, no. 5, pp. 1545–1558, 2005.

[31] BROWN, C., BREINAN, E., and KEAR, B., "Method for fabricating articles by sequential layer deposition," Apr. 6 1982. US Patent 4,323,756.

[32] HOFMEISTER, W., WERT, M., SMUGERESKY, J., PHILLIBER, J., GRIFFITH, M., and ENSZ, M., "Investigation of solidification in the laser engineered net shaping (lenstm) process," *JOM*, vol. 51, no. 7, pp. 1–7, 1999.

[33] GRIFFITH, M., SCHLIENGER, M., HARWELL, L., OLIVER, M., BALDWIN, M., ENSZ, M., ESSIEN, M., BROOKS, J., ROBINO, C., SMUGERESKY, J., and OTHERS, "Understanding thermal behavior in the lens process," *Materials & design*, vol. 20, no. 2, pp. 107–113, 1999.

[34] GRUJICIC, M., CAO, G., and FIGLIOLA, R., "Computer simulations of the evolution of solidification microstructure in the lens^{TM} rapid fabrication process," *Applied surface science*, vol. 183, no. 1, pp. 43–57, 2001.

[35] GREMAUD, M., WAGNIÈRE, I., ZRYD, A., and KURZ, W., "Laser metal forming: process fundamentals," *Surface engineering*, vol. 12, no. 3, pp. 251–259, 1996.

[36] LEWIS, G. and SCHLIENGER, E., "Practical considerations and capabilities for laser assisted direct metal deposition," *Materials & Design*, vol. 21, no. 4, pp. 417–423, 2000.

[37] GÄUMANN, M., BEZENCON, C., CANALIS, P., and KURZ, W., "Single-crystal laser deposition of superalloys: processing–microstructure maps," *Acta materialia*, vol. 49, no. 6, pp. 1051–1062, 2001.

[38] MARCIN JR, J., NEUTRA, J., ABBOTT, D., ADUSKEVICH, J., SHAH, D., CARRAWAY, D., LANGEVIN, R., SAUERHOEFER, M., and STONE, R., "Containerless method of producing crack free metallic articles by energy beam deposition with reduced power density," May 4 1999. US Patent 5,900,170.

[39] DAS, S., *Direct selective laser sintering of high performance metals: machine design, process development and process control*. 1998.

[40] ATHREYA, S. R., *Processing and characterization of carbon black-filled electrically conductive nylon-12 nanocomposites produced by selective laser sintering*. PhD thesis, Georgia Institute of Technology, 2010.

[41] ROSENTHAL, D., "The theory of moving sources of heat and its application to metal treatments," ASME, 1946.

[42] BOURELL, D., LEU, M., and ROSEN, D., "Roadmap for additive manufacturing: identifying the future of freeform processing," in *University of Texas, Arlington, VA, NSF Workshop*, 2009.

[43] BOUGHTON, P., RIDER, G., and SMITH, E., "Feedback of weld penetration in 1978," *Advances in Welding Processes*, 1978.

[44] GARLOW, D. and WEINERT, J., "A model of full penetration arc-welding for control system design," *Journal of dynamic systems, measurement, and control*, vol. 107, p. 40, 1985.

[45] ANDERSEN, K., COOK, G., KARSAI, G., and RAMASWAMY, K., "Artificial neural networks applied to arc welding process modelingand control," *IEEE Transactions on Industry Applications*, vol. 26, no. 5, pp. 824–830, 1990.

[46] ZHANG, Y. and KOVACEVIC, R., "Neurofuzzy model-based predictive control of weld fusion zone geometry," *IEEE Transactions on Fuzzy Systems*, vol. 6, no. 3, pp. 389–401, 1998.

[47] DOUMANIDIS, C., "Multiplexed and distributed control of automated welding," *IEEE Control Systems Magazine*, vol. 14, no. 4, pp. 13–24, 1994.

[48] SALEHI, D. and BRANDT, M., "Melt pool temperature control using labview in nd: Yag laser blown powder cladding process," *The international journal of advanced manufacturing technology*, vol. 29, no. 3, pp. 273–278, 2006.

[49] TANG, L. and LANDERS, R., "Melt pool temperature modeling and control for laser metal deposition processes," in *American Control Conference, 2009. ACC'09.*, pp. 4791–4796, IEEE, 2009.

[50] Tang, L. and Landers, R., "Melt pool temperature control for laser metal deposition processes-part i: Online temperature control," *Journal of manufacturing science and engineering*, vol. 132, no. 1, 2010.

[51] Tang, L. and Landers, R., "Melt pool temperature control for laser metal deposition processes-part ii: Layer-to-layer temperature control," *Journal of manufacturing science and engineering*, vol. 132, no. 1, 2010.

[52] Gregori, A., "A survey of welding and repairing of nickel superalloys for gas turbines," *The Welding Institute*, 2003.

[53] Rush, M., Colegrove, P., Zhang, Z., and Courtot, B., "An investigation into cracking in nickel-base superalloy repair welds," *Advanced Materials Research*, vol. 89, pp. 467–472, 2010.

[54] Mathey, G., "Method of making superalloy turbine disks having graded coarse and fine grains," May 17 1994. US Patent 5,312,497.

[55] Chang, K., "Method of making high strength superalloy components with graded properties," Apr. 11 1989. US Patent 4,820,358.

[56] Kramida, A., Ralchenko, Y., Reader, J., and (2012), N. A. T., "Nist atomic spectra database (ver. 5.0)," Feruary 2013.

[57] Ghaemi, A., "Freezing-point-blackbody radiation sources for the 29.78–1084.62°*c* temperature range," *Applied optics*, vol. 35, no. 13, pp. 2211–2215, 1996.

[58] Pottlacher, G., Hosaeus, H., Wilthan, B., Kaschnitz, E., and Seifter, A., "Thermophysikalische eigenschaften von festem und flüssigem inconel 718," *Thermochimica acta*, vol. 382, no. 1, pp. 255–267, 2002.

[59] Mills, K. C., Youssef, Y. M., Li, Z., and Su, Y., "Calculation of thermophysical properties of ni-based superalloys," *ISIJ international*, vol. 46, no. 5, pp. 623–632, 2006.

[60] Del Campo, L., Pérez-Sáez, R., González-Fernández, L., Esquisabel, X., Fernández, I., González-Martín, P., and Tello, M., "Emissivity measurements on aeronautical alloys," *Journal of Alloys and Compounds*, vol. 489, no. 2, pp. 482–487, 2010.

[61] Masuda, H., Higashitani, K., and Yoshida, H., *Powder technology: Fundamentals of particles, powder beds, and particle generation.* Boca Raton: CRC Press/Taylor & Francis, 2007.

[62] Gambone, J., "Quantitative metallography tracking and analysis for the scanning laser epitaxy process applied to cmsx-4 and rené-80 nickel-based superalloys," Master's thesis, Georgia Institute of Technology, 2012.

[63] DAS, S. and BEAMAN, J. J., "Direct selective laser sintering of metals," Apr. 2 2003. EP Patent 1,296,776.

[64] FLEMINGS, M. C., "Solidification processing," *Metallurgical and Materials Transactions B*, vol. 5, no. 10, pp. 2121–2134, 1974.

[65] CHANG, F., CHEN, C., and LU, C., "A linear-time component-labeling algorithm using contour tracing technique," *Computer Vision and Image Understanding*, vol. 93, no. 2, pp. 206–220, 2004.

[66] LIÑÁN, C. C., "cvBlob." http://cvblob.googlecode.com.

[67] OGATA, K., *Discrete-time control systems*, vol. 8. Prentice-Hall Englewood Cliffs, NJ, 1995.

[68] LJUNG, L., *System identification*. Wiley Online Library, 1999.

[69] GOODWIN, G. C. and SIN, K. S., *Adaptive filtering prediction and control*. Dover Publications, 2009.

[70] IOANNOU, P. and FIDAN, B., *Adaptive control tutorial*, vol. 11. Society for Industrial Mathematics, 2007.

[71] "Math.net numerics," March 2013.

[72] EAGAR, T. and TSAI, N., "Temperature fields produced by traveling distributed heat sources," *Welding Journal*, vol. 62, pp. 346–355, December 1983.

[73] TSAI, N. and EAGER, T., "Changes of weld pool shape by variations in the distribution of heat source in arc welding," *Metallurgical Soc of AIME, Warrendale, PA, USA*, vol. 1984, 1984.

[74] OZISIK, M. and OEZISIK, M., *Heat conduction*, vol. 300. John Wiley & Sons New York., 1993.

VITA

Rohan Bansal was born in Amherst, NY in 1984 and raised in Clarence, NY, just outside of Buffalo. He graduated from Nichols High School in 2002 and went on to pursue undergraduate study at the Georgia Institute of Technology. In 2004 he spent a semester studying abroad in Metz, France. By 2007, he had received both a Bachelor of Science in Mechanical Engineering and a Bachelor of Science in Computer Engineering. After pursuing this dual-degree in engineering, he enrolled in the graduate program at Georgia Tech. During graduate school, he joined the Direct Digital Manufacturing group and worked on development of the Scanning Laser Epitaxy (SLE) additive manufacturing process under the advisement of Dr. Suman Das. He completed his Masters of Science in Mechanical Engineering in 2010 and received his Doctor of Philosophy in Mechanical Engineering in 2013 for his dissertation entitled *Analysis and Feedback Control of the Scanning Laser Epitaxy Process Applied to Nickel-Base Superalloys.* He will be joining Chart Industries, Inc. as a R&D manager after leaving Georgia Tech.